Author:
Alexander, Robert W

Title:
Exploring the mineralisation and functionalisation of recombinant Pyrococcus furiosus ferritin

Exploring the mineralisation and functionalisation of recombinant *Pyrococcus furiosus* ferritin

Robert Alexander

A dissertation submitted to the University of Bristol in accordance with the requirements for award of the degree of M.Sc. by Research in the Faculty of Cellular and Molecular Medicine

Submitted 2nd May 2020

Abstract

Set against a background of global antimicrobial resistance and an increased mortality rates from sepsis, there is a clear requirement for novel rapid point-of-care diagnostic technologies, especially those that are affordable for use in a poor resource setting. The magnetic labelling of bacteria using functionalised ferritin nanoparticles presents one clear opportunity to capture and identify bacteria from patient samples using magnetic based cell separation techniques. Here, the mineralisation and functionalisation of a recombinant ferritin from *Pyrococcus furiosus* has been investigated. This involved reconstitution of an iron oxide core within the particle and cationisation of the outer surface to facilitate adhesion to bacterial cell surface using electrostatic interactions. Analysis of the mineralised particles using transmission electron microscopy (TEM) and small angle X-ray scattering (SAXS) provided evidence to suggest the tuneable mineralisation of the iron oxide core without impacting particle polydispersity. Monte Carlo based dummy atom modelling and form factor fitting of SAXS data provides evidence of how the iron core reconstitutes within the particle as core and multi shell models. Super conducting interference magnetometry of the mineralised particles indicated that the experimental conditions promoted the formation of a hydrated iron (III) oxide ($Fe_2O_3 \cdot nH_2O$) core, rather than the desired magnetite (Fe_3O_4). Successful chemical cationisation of the non-mineralised recombinant ferritin highlights the potential application of these particles, for example in magnetic based microfluidic devices to capture and concentrate bacteria, once magnetic core mineralisation has been achieved. Moreover, the controllable mineralisation demonstrated in this project suggests that individual bacterial selection could be achieved by harnessing the differences in magnetic susceptibility of particles reconstituted under different iron concentrations. Ultimately, such magnetic nanoparticles could facilitate rapid identification and infection diagnosis.

Acknowledgements

Firstly, I would like to thank my supervisors. Annela Seddon, who inspired me with her support to learn a whole new discipline. A Monday morning meeting is like a rocket of motivation for the whole week! And, Jim Spencer who was always available for discussion and guidance, with his mentorship I have improved massively over the past 3 years. I am lucky to have both of your support, so thank you.

A massive thank you to Steve Volsen for coming out of retirement to proofread my text, it was important to have a fresh set of eyes, and some great constructive criticism. Thank you to Sara Correia Carreira, Kristian Le Vay and Rob Hughes, who helped me actualise this concept, acting as unofficial supervisors answering my questions, they were always happy to help, I owe you guys a pint! Thank you to the academics at Bristol University who allowed me to conduct my project in their lab or with their equipment. These include Paul Curnow, Sven Friedemann, Walther Schwarzacher and Adam McAleer. Special thanks to Judith Mantell, Chris Neal and the Wolfson Bioimaging facility. Equally, thank you to those at Diamond Light source B21, Nathan Cowieson and Nikul Khunti for their support with SAXS measurement and analysis. And, thank you to all those in the Spencer group and the D60 lab for the community spirit and support. Finally, thank you to my Mum and Dad (Sue and Bob Alexander), their continued support kept my eyes on the prize - it’s happening!

Author declaration

I declare that the work in this dissertation was carried out in accordance with the requirements of the University's Regulations and Code of Practice for Research Degree Programmes and that it has not been submitted for any other academic award. Except where indicated by specific reference in the text, the work is the candidate's own work. Work done in collaboration with, or with the assistance of, others, is indicated as such. Any views expressed in the dissertation are those of the author.

Online submission.

ROBERT ALEXANDER

2nd May 2020

SIGNED: ..... DATE:.....

Contents

Table of figures

Abbreviations

Listed below are the abbreviations used in this thesis. They are generally defined where they first appear in the text. Commonly used units, chemical symbols, company names and brands have been excluded.

AIS	Ammonium iron sulphate
AMR	Antimicrobial resistance
COA	Certificate of analysis
DAM	Dummy atom model
DLS	Dynamic light scattering
DMPA	N,N′-dimethyl-1,3-propanediamine
EDC	1-ethyl-3-(3-dimethylaminopropyl)carbodiimide
HEPES	4-(2-hydroxyethyl)-1-piperazineethanesulfonic acid
HPLC	High performance liquid chromatography
Hsf	Horse spleen ferritin
ICP-OES	Inductively-coupled plasma optical emission spectroscopy
IEC	Ion exchange chromatography
ITPG	Isopropyl β- d-1-thiogalactopyranoside
MALDI TOF	Matrix-assisted laser desorption ionisation time of flight
MES	2-(N-morpholino) ethanesulfonic acid
MfPf	Magnetised ferritin *Pyrococcus furiosus*
MPMS	Magnetic property measurement system
MWCO	Molecular weight cut-off
PCR	Polymerase chain reaction
PDI	Polydispersity index
PDR	Polydispersity ratio
PEG	Polyethylene glycol
Pf	*Pyrococcus furiosus*
PTA	Phosphotungstic acid
rpm	Revolutions per minute
SDS-PAGE	Sodium dodecyl sulphate polyacrylamide gel
SEC	Size exclusion chromatography
SLD	Scattering length density

SPION	Superparamagnetic iron oxide nanoparticle
SQUID	Super conducting interference device
TCEP	Tris(2-carboxyethyl) phosphine
TEM	Transmission electron microscopy
SAXS	Small angle X-ray scattering
UV	Ultraviolet
WGS	Whole genome sequencing

Chapter 1 Introduction

In microbial imaging for diagnosis and research, the development of cell labelling has two important functions. First, to further understand cellular pathways through the visualisation of cellular processes. Second, cell labelling can provide rapid identification of the presence of cell types, something which, if specific, will prove to be a valuable diagnostic tool [1].

The labelling of bacteria via unique surface molecules with magnetic nanoparticles presents an opportunity to impact rapid diagnostics testing, offering identification through the isolation of bacteria from patient samples without the needs for enrichment culturing. The development of rapid point-of-care diagnostics has been highlighted as a major intervention in the response to the global threat of antibiotic resistance [2].

The following chapter will explain how diagnostic nanoparticles are synthesised, and how the magnetic properties of superparamagnetic iron oxide nanoparticles (SPIONS) can be exploited to capture and concentrate bacteria from solution, with particular focus on ferritin the ubiquitous self-assembling protein.

1.1 Nanoparticles

Because of their abundance, diversity, versatility and unique properties nanoparticles are often utilised to solve technical problems faced in the biomedical world. This section will introduce nanoparticles and identify some of those currently in use.

Structures and particles on the nanoscale (1 nm-100 nm), are considered to be nanoparticles, Figure 1.1 demonstrates the scale of nanoparticles in relation to other microscopic structures [3]. Such particles behave differently than their micro or macro counterparts regarding interatomic interactions and electromagnetic interactions. For example, as the diameter of a spherical nanoparticle decreases the surface area increases in relation to volume, the consequence of which is an amplification of surface interactions per unit volume compared to larger scale particles [4]. Consequently spherical nanoparticles make ideal candidates for catalytic activity or surface functionalisation, where the increased contact points on the surface can act as molecular foundations for a range of specific interactions [4].

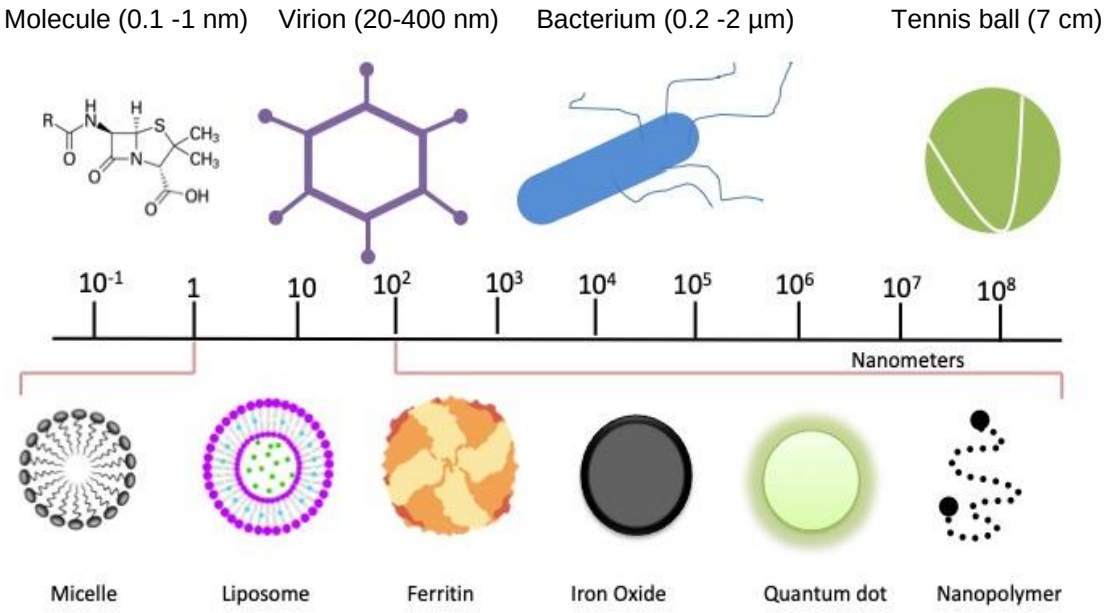

Figure 1.1 Cartoon illustrating the scale of nanoparticles

Nanoparticles are described as being 1 nm-100 nm, note that some virus particles fall into this category. Figure adapted with permissions from M. T. Amin. et al under Creative Commons Attribution License.

With such unique behaviour, nanoparticles have been utilised by industry. However inorganic production of synthetic nanoparticles is often expensive, with both ‘top down’ physical size reduction or ‘bottom up’ chemical precipitation or synthesis methods, relying on the use of toxic materials, high energies or unsustainable technologies such as UV radiation or lithography [5]. To circumvent the unsustainable production of nanoparticles, a growing trend in synthesis is the use of biological systems to organically produce self-assembling nanoparticles, often by commandeering naturally occurring processes within microbes. The use of organic materials offers industry the opportunity to pursue more environmentally sustainable activity, since such practices require far less energy and can generate high yield and reproducible nanoparticles [6].

Improved organic nanoparticle technologies coupled with advances in molecular medicine have impacted the clinic, with several nanoparticles being developed for diagnostics or pharmaceutical therapeutics. There are many FDA approved nanoparticles which act to enhance the efficacy or delivery of a drug to a target site or have a therapeutic effect themselves [7]. Neulasta, for example, is a granulocyte colony stimulating factor conjugated to a polyethylene glycol (PEG) nano polymer, which serves to increase drug half-life [8]. Similarly, naturally forming lipid bilayer vesicles known as liposomes have been used to carry anti-cancer drugs to malignant cells[9].

Biocompatible synthetic nanoparticles, such as iron oxides or carbon dots, have been developed as alternatives to inorganic, high toxicity heavy metal based bio imaging and sensing methods [10]. Glycan functionalised carbon dots, for example, emit fluorescence of a particular wavelength while demonstrating non-toxicity in HeLa and breast cancer cells [11]. On the other hand, SPIONS have been developed for use in contrast imaging. Iron oxide nanoparticles were once popular for diagnostic contrast agents, however, side effects such as nausea and urticaria ultimately led to a decline in their usage in the clinical setting [12]. Despite this, iron oxides are considered as low toxicity because of the body’s innate efficiency of iron metabolism [13]. The intrinsic magnetic properties of iron oxide offer unique biomedical, industrial and environmental applications [14].

Currently, magnetic nanoparticles are utilised in medicine as tumour- specific targeted drug delivery systems, similar to liposomes. The application of a magnetic field to $CoFe_2O_4$ magnetic nanoparticles conjugated with paclitaxel (PTX), an anti-mitotic drug, has been shown to increase efficacy through controlled localisation and target cell penetration in human ovarian carcinoma SKOV-3 cells[15]. In an alternative application, polyethylene glycol bis(amine) decorated magnetic nanoparticles have been shown to concentrate heavy metal ions from solution; such research has identified magnetic nanoparticles as viable sustainable technologies for remediation of environmental water [16].

1.2 Magnetic nanoparticles

The magnetic properties of a material result from the magnetic moments associated with the atomic particles of which the material is made up. The magnetic moment associated with the protons and neutrons within the nucleus is of too low a magnitude to influence magnetism; therefore, it is the sum of the magnetic moments associated with electrons that contribute to the total magnetic properties of a material. Electrons provide magnetic moments through electrical charge in motion, contributing to both orbital magnetic moment and spin magnetic moment [17]. Materials made from atoms with filled electron shells have no magnetic properties due to the total cancellation of opposing electron orbits, these are considered diamagnetic and their magnetic response opposes the magnetic field [14]. Those materials made from electrons with partially filled shells have a weak magnetic property in response to an applied magnetic field and are classed as paramagnetic. The magnetisation of these materials is weak but is proportionally aligned in parallel with the direction of applied field. Ferrimagnetic particles have a strong magnetic susceptibility in response to a magnetic field and remain magnetised once the field is removed [18].

At nanoscale, ferrimagnetic particles exhibit superparamagnetism, a phenomenon characterised by rapid change in domain orientation in response to thermal energy [5]. Consequently, nanoparticles with enhanced magnetic susceptibility, such as iron oxides or magnetite alloys, are known as SPIONs. Often an amphiphilic layer, such as dextran or PEG modified starch, is used to surround the SPION to avoid agglomeration and improve targeted functionalisation [5].

When considering bulk ferrous molecules, the presence of conflicting magnetic domains demands high energies or strong magnetic fields to reach a magnetic saturation. A substantial increase in applied field (H) is required to increase the magnetic flux of a material (Φ_B). Bulk ferrous materials maintain magnetic flux after interaction with a magnetic field and require a coercive force to reach $\Phi_B = 0$ [17]. Due to having small dimensions, a diameter or less than 30 nm, the magnetic energy required by SPIONs to reach magnetic saturation is much lower. This can be explained by the absence of conflicting magnetic domains, and as a result no coercive field is required to return to a magnetic saturation point $\Phi_B = 0$ [5].

Figure 1.2 describes the contrast in coercivity required by bulk and nano ferrous particles [19]. Superparamagnetism can be explained quantitatively through the measurement of the blocking temperature, this is described as the point in the system where the relaxation time, the time taken for a particle domain to flip on its axis in relation to an applied field, is equal or less than the measurement time (TM≤TN) [20]. When considering superparamagnetic particles, the relaxation time is less than the measurement time (TM >TN) at very low temperatures (>20 K). Below the blocking temperature where nanoparticles are cooled to extremely low temperatures (~5K) there is insufficient energy for the magnetic domain to flip its axis[20].

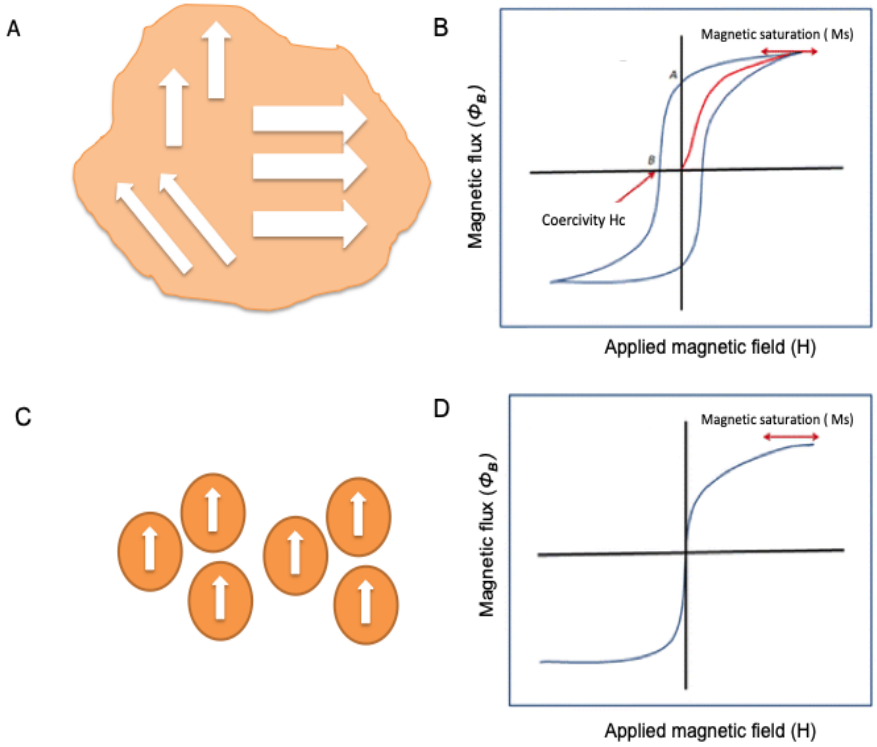

Figure 1.2 Characteristics of magnetic domains

(A) Schematic example of the possible orientation of magnetic domains in bulk ferrous particles (B) The coercivity required for the particle to reach $\Phi_B=0$ evident in the hysteresis Magnetic flux (Φ_B) is plotted against applied field (H). (C) Illustrates the single domain orientation of ferrous nanoparticles, (D) Graph depicting the absence of coercivity and the hysteresis characteristic of SPIONS. Figure adapted with permissions from V. V. Mody, et al. under Creative Commons Attribution License.

1.3 Cell labelling

Cell labelling is a common technique used to visualise and characterise cells and cellular processes within a cell. Historically scientists have used cell labelling in order to better identify bacteria. In microscopy common labels include dyes or fixative agents that stain the cell aiding contrast imaging through the absorption of light. For example, Gram staining uses iodine, crystal violet and carbol fuchsin to visualise prokaryotic cells, differentiating Gram-positive bacteria, whose thick peptidoglycan cell wall is stained purple, from Gram-negative cells, which are counter stained by the fuchsin. Gram-negative bacteria have less peptidoglycan, from which the violet stain is readily washed away, allowing discrimination between the two types of bacteria [21]. Consequently, Gram staining aids in the identification of bacteria, via bacterial morphology and cell wall compostition, but is unable to identify species, strain or antibiotic resistance profiles. It is conceivable that labelling bacteria with nanoparticles with species or strain level specificity, using intermolecular interactions between the cells and the unique surface molecules, could provide potent new infection diagnostic tools.

By exploiting non-specific electrostatic intermolecular interactions, nanoparticles can adhere to bacterial surface structures such as lipopolysaccharide in Gram-negative and teichoic acid in Gram-positive organisms. These structures give the bacterial envelope an overall negative charge, thus allowing cationised nanoparticles to adhere through non-specific electrostatic intermolecular interactions [22]. Horse spleen ferritin cationised with *N*,*N*′ -dimethyl-1,3-propanediamine (DMPA), has been shown to adhere to Gram-negative *Escherichia coli* (*E. coli.*) and Gram-positive *Staphylococcus aureus (S. aureus)* [23]. This technology is non-specific to bacterial species but facilitates the capture and concentration of bacteria out of solution, ideal for water purification or for rapid diagnostics of the presence of bacteria.

For more specific cell labelling, receptor-ligand pairing has been appropriated in the development of bacteria-specific SPIONS. The antimicrobial agent vancomycin recognises the D-ala D-ala motif found in the bacterial envelope and when functionalised on FePt SPIONS, the vancomycin-nanoparticle conjugate can adhere to bacterial surfaces. Research demonstrated the capture of Gram-positive enterococci at concentrations of 4 $CFU.ml^{-1}$ [24].

For increased individual bacterial specificity, nanoparticles can be functionalised with specific antibodies that target ligands or molecular motifs to generate high affinity binding. Identification to a species or strain level is advantageous with prescribing correct antimicrobials as this can limit the unnecessary prescription of antibiotics (e.g. for viral infections) or use of agents inappropriate for a given infection. As part of the adaptive immune defence, antibodies are generated to protect against bacterial or viral infection. Monoclonal derivatives of such immunoglobulins could be conjugated to SPIONS to facilitate pathogen specific binding.

Due to specific structural and chemical constitution, antibodies bind to antigens with varying specificity and affinity. The individual sequence of amino acid residues along an antibody's paratope provides a surface area with numerous opportunities for definite, high affinity electrostatic intermolecular interactions such as van der Waals forces [22]. These dispersion forces result from temporary fluctuations in electron densities as electrons orbit around their nucleus, thus producing transient dipole moments. Such dipole moments can induce other dipole moments on neighbouring atoms. Particularly, atoms with higher atomic mass whose outer electron shells are further from the nucleus; accumulation of such dipole moments, through increased surface area, can contribute to affinity of binding [25].

In the 1990's ferritin-dextran beads functionalised with biotin were developed to bind to streptavidin fluorochrome conjugates bound to a biotinylated antibodies on mice spleen cells, thus allowing the quantifiable and specific labelling of cells [26]. More recently, Fe_3O_4 SPIONS conjugated to monoclonal antibodies for epidermal growth factor were shown to detect brain gliomas by binding to the transmembrane receptor over expressed by malignant cells in Wistar rat models [27] as demonstrated in Figure 1.3.

Despite their increased affinity and specificity, there are limitations with antibody technologies being adopted for therapeutic use. Being proteinaceous, they require certain conditions to avoid denaturation, equally increased quality control screening is required to assess and restrict the host immune response. For example, one of the first monoclonal antibodies developed for preventing kidney transplant rejection, Orthoclone OKT3, had restricted usage due to the human anti-mouse antibody response [28]. Furthermore, there are increased costs associated with their production, for instance a

year's supply of monoclonal derived leukaemia treatment can cost in excess of £37,000[29]. These drawbacks justify the development bacterial binding SPIONS based around electrostatic attraction. Proteins with increased stability, such as ferritin, developed at lower production costs could prove to be more appropriate in lower-middle income countries where resources are limited.

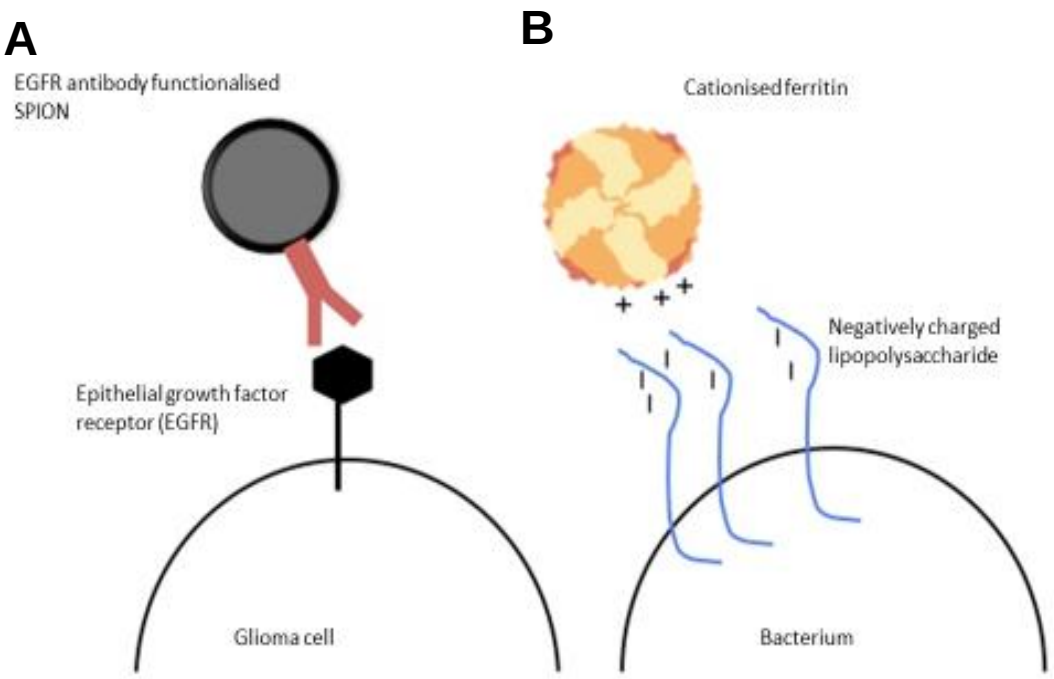

Figure 1.3 Cartoon depicting nanoparticle adherance to cell types

(A) SPION conjugated to EGFR monoclonal antibody, makes highly specific interactions with the EGF receptor overexpressed on glioma cells.
(B) Cationised ferritin molecule makes non-specific interactions with negatively charged bacterial cell surface.

1.4 Ferritin

Recent research into the constitution of a magnetic core within commercially available horse spleen ferritin, and the subsequent cationisation and efficiency of bacterial capture, has identified ferritin as a promising tool for bacterial concentration [23]. This section introduces the biochemistry of ferritin and highlights potential avenues for the development of a recombinant mineralised ferritin for bacterial capture.

As one of the transition elements, iron has multiple oxidation states as, due to the incomplete d-orbital shell, it is energetically favourable for iron to lose or gain electrons and remain stable. Iron has a 5 d-orbital outer shell electron configuration and can form +5, +4, +3 and +2 oxidation states [30]. In biological systems the most common oxidation states are ferrous iron (Fe^{2+}) and ferric iron (Fe^{3+}) [31]. For both prokaryotic and eukaryotic organisms, iron is an essential element for cellular metabolism and biosynthetic pathways [32]. However, it is the redox potential of iron in excess that is damaging to cells, forming reactive oxygen species that interact with cellular components [31]. One of the roles of ferritin is to sequester Fe^{2+} atoms, storing them as hydrated oxo-mineral clusters until reduction and rehydration releases the iron as required by the cell [33].

Extensively characterised in the literature [33] [34],ferritin is a self-assembling multimeric protein icositetramer (24 subunits), a large 480 kDa protein with a diameter of ~12 nm [33]. In mammalian cells there are two identified sub-unit isoforms, heavy (H) and light (L) chains. Particles can be a mixture of both isoforms, and constituent ratios in assembled particles vary due to physiological location and conditions. For example, ferritin found in splenic macrophages has a higher L-chain ratio in response to increased iron loading from dying red blood cells [35]. In prokaryotes, ferritins are homopolymers, assembled from 24 homogenous sub-units, with no examples of L/H chain stoichiometry [34].

Although ferritin sequences may differ between organisms, there are conserved structural regions that facilitate storage of up to 4000 iron atoms [33]. These include channels that allow the entry and exit of Fe^{2+} into the particle via diffusion, occurring at the 3-fold and 4-fold symmetry axes. These can be seen on the PYMOL generated images of *Pyrococcus furiosus* ferritin shown in Figure 1.4. Each subunit contains a

ferroxidase catalytic site that facilitates the oxidation of Fe^{2+} into a di-ferro-oxo mineral precursor. Incoming Fe^{2+} ions displace the precursor into the negatively charged interior where, at carboxylate-rich nucleation sites an iron-oxide core is constituted [36]. Although, L-chain subunits contain an inactive ferroxidase site, research has indicated that there is no reduction in iron mineralisation in recombinant homopolymeric ferritin, formed solely of L-chain subunits [36]. Instead, the negatively charged nucleation sites of the L-chain homopolymer enable the charge directed mineralisation of a mineral core in the absence of ferroxidase activity. This type of mineralisation also facilitates the constitution of a core made from other minerals, for example the mineralisation of silver ions within a *Pyrococcus furiosus* ferritin [37]. Similarly, manganese oxyhydroxide cores have been constituted in de-mineralised horse spleen ferritin [38].

Stability is a desired characteristic for nanoparticles in order for them to reach their target destination without particle disintegration. The stability of ferritin is a consequence of the numerous intermolecular forces that direct self-assembly and maintain the protein structure, with studies demonstrating the multimeric structural stability of ferritin over a wide range pH [39].

In addition to pH stability, ferritins from thermophilic bacteria such as *Pyrococcus furiosus* (*Pf*) have demonstrated stability at high temperatures, due to the source organism inhabiting deep-sea thermal vents where temperatures can reach 120^{o}C [40]. Research by Tatur et al. [41] comparing sequences and crystal structures of various bacterial ferritins, demonstrates that it is intramolecular salt bridges, as evident in *E. coli.* and *Campylobacter jejuni* ferritin, that often promote thermal stability. Interestingly, however, this was not evident with *Pyrococcus furiosus,* where an increased number of hydrogen bonds are responsible for a thermal stability at temperatures up to 120^{o}C [41] .

In addition to increased stability, research into *Pf* ferritin has illustrated an increased magnetic susceptibility with rapid saturation at low magnetic fields. This could be explained by the electrostatic potential on the inside of the icositetramer. As shown in Figure 1.5, the *Pf* ferritin possesses a single acidic patch or carboxylate nucleation site whereby a single iron core is reconstituted thus limiting the number of conflicting

magnetic domains [42]. Alternatively, in mammalian ferritin, comparative studies have shown that the majority of the interior facing subunit is acidic, offering multiple nucleation sites that may reconstitute a number of iron oxide crystals with opposing domains, reducing magnetic susceptibility [42]. Whether the reported increased magnetic susceptibility is a benefit to industry has yet to be seen; however, it is evident that, given its thermostability, the magnetic properties of *Pf* ferritin could be employed at higher temperatures than currently achievable with other biocompatible nanoparticles.

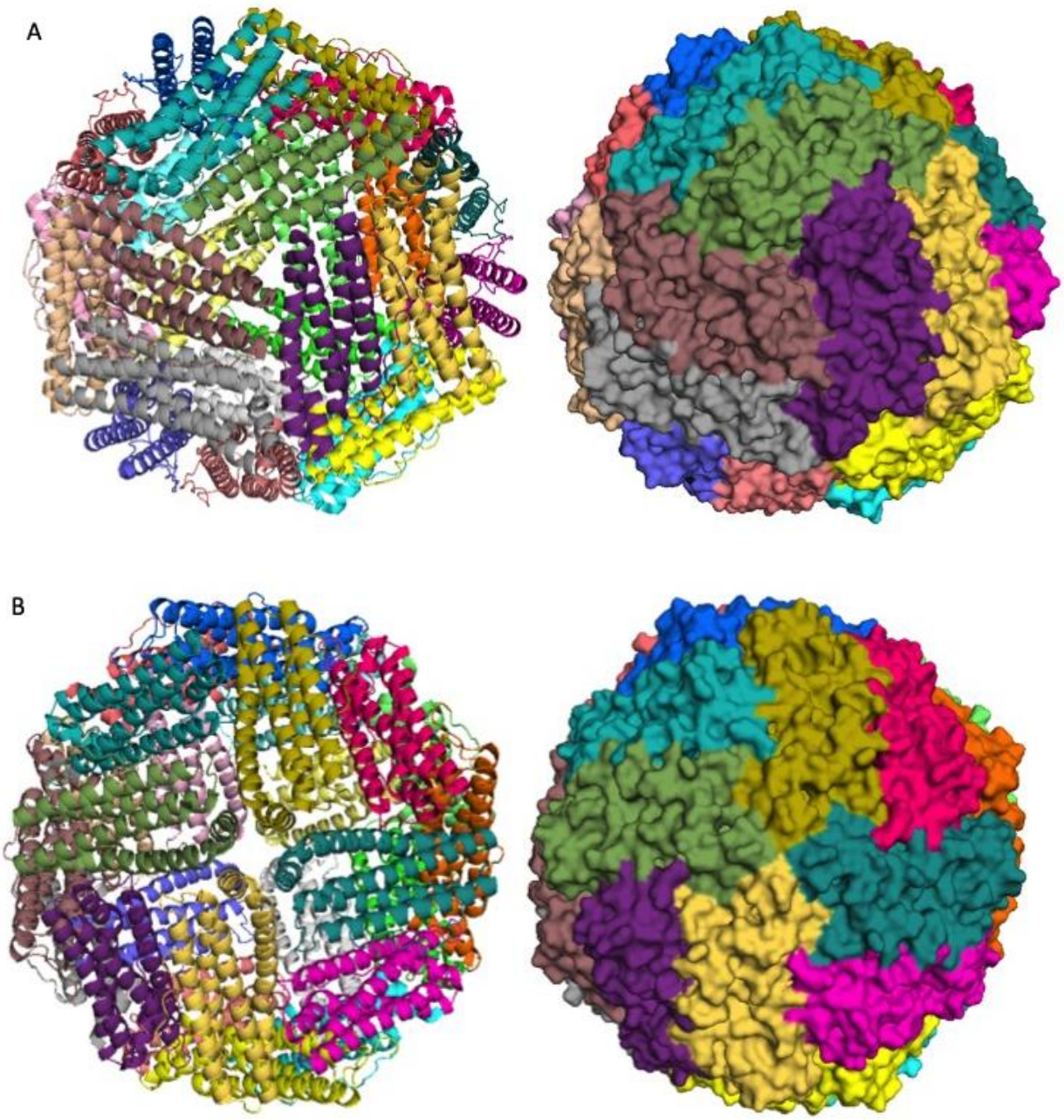

Figure 1.4 Structure of *Pyrococcus furiosus* ferritin

Pymol generated models of *Pyrococcus furiosus* ferritin, showing the subunit ribbon cartoon (left) and space filling representation (right). View along the 3-fold axis (A) and the 4-fold axis (B). PDB ID 2JD7 [36].

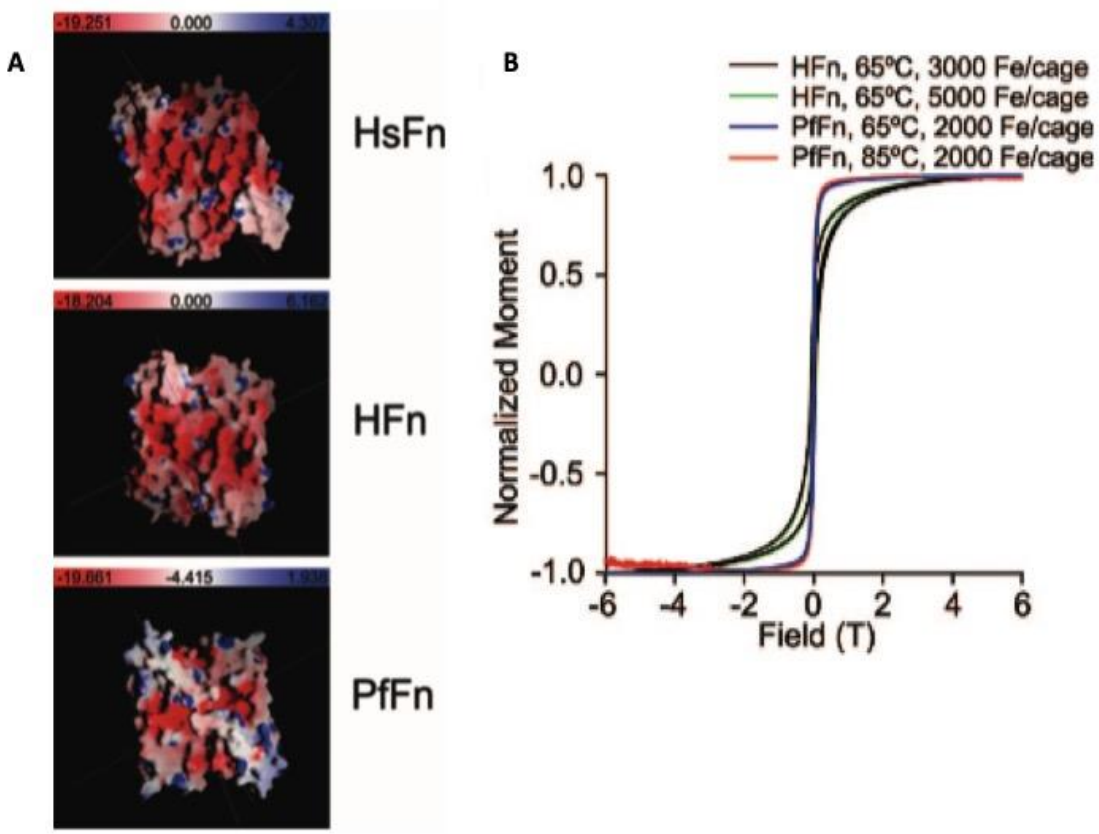

Figure 1.5 Evidence for increased magnetic susceptibility of *Pyrococcus* ferritin

(A) Space filling models indicating the electrostatic potential of the subunit. Mammalian ferritins, unknown isoform horse (HsFn) and human H-chain (HFn) have a greater overall negative charge than *Pyrococcus* ferritin (PfFn). Negative charge is Red, positive charge is coloured blue and no charge is white. (B) Magnetic susceptibility of *Pyrococcus* compared with human H-chain ferritin. Both reprinted with permission M. J. Parker *et al.* 2008, American Chemical Society.

1.5 The requirement for rapid diagnostics

The development of rapid bacterial diagnostic technologies has been identified as a key response to some of the problems associated with the worldwide challenge of antimicrobial resistance (AMR) [43]. Characterised by the inefficacy of antibiotic drugs, the phenomenon of AMR is a product of the combination of human pathogens acquiring multiple resistance genes, the shortcomings of novel antibiotic agents and poor antibiotic stewardship. Antibiotic inefficacy can have serious consequences for individuals whose survival depends on antibiotics, for example immunosuppressed patients [2].

The over prescription of antibiotics is a common problem, particularly in primary care settings, where there is currently no point of care diagnostic technology to differentiate between viral and bacterial infections. In a comprehensive investigation into antibiotic prescribing on ambulatory care visits in the United States, an estimated 43% of prescriptions were potentially inappropriate [44]. Technologies that improve rapid diagnosis are just one of the interventions that can limit the unnecessary prescription of antibiotics and as a consequence, limit the growth of AMR.

Currently, rapid diagnostic technologies do exist, these include matrix assisted laser desorption/ionisation-time of flight (MALDI-TOF) [45], polymerase chain reaction (PCR)[46] and whole genome sequencing (WGS) [47], all of which are extremely good at determining species, strain and resistance profiles of infections. Problematically, these highly specialised technologies are expensive and consequently out of budget for primary care providers and those in resource poor setting such as the developing world. Furthermore, these diagnostics rely on the quality of the sample and there is a real challenge to isolate or identify whole bacteria without the use of traditional pre-enrichment culturing [24].

The requirement for rapid diagnostics is most significant for the detection of sepsis, characterised by the rapid onset of an inappropriate inflammatory response to bacterial blood stream infection often resulting in mortality, with sepsis accounting for 25% of hospital fatalities[48]. Early recognition in order to provide effective antibiotics is a key determination in patient outcomes, however blood culture diagnostics remain the gold standard despite low sensitivity and low throughput (over 48 hour turnaround times) [46].

PCR-based diagnostic technologies, such as Light Cycler SeptiFast (LC-SF) allow for the detection of 25 pathogens within hours expediting the appropriate commencement of therapies. However, there is a likelihood for false-negative results with these technologies, complicating patient outcomes [46].

1.6 Aims and objectives

In response to the urgent requirement for novel rapid diagnostic technologies, the aim of this project is to develop a magnetic bacterial labelling particle from recombinant *Pyrococcus furiosus* ferritin in order to non-specifically concentrate bacteria from solution.

After recombinant protein expression, particle characterisation is required to identify suitability for downstream functionalisation, with particle size and polydispersity a key concern. Advanced particle characterisation by transmission electron microscopy (TEM), small angle X-ray scattering (SAXS) and dynamic light scattering (DLS) were used to compare recombinant particles with commercially available horse spleen ferritin.

In order to engineer a magnetic nanoparticle with tuneable magnetic susceptibility from the recombinant protein, iron oxide cores of controlled concentration were reconstituted within the cavity of the nanoparticles. Based on evidence in the literature[42] *Pyrococcus furiosus* (*Pf*) ferritin demonstrates increased magnetic properties compared with mammalian ferritin. Therefore, advanced magnetometry was used to investigate how mineralisation concentration affects magnetic susceptibility.

Ultimately the chemical cationisation of the recombinant particle will be investigated with zeta potential measurements. With this analysis used to describe the change in particle surface charge, as seen with investigations using horse spleen ferritin[23].

These aims and objectives will be reported in three chapters. Firstly, the synthesis and characterisation of the nanoparticles will be discussed in Chapter 2. The SAXS analysis and particle modelling will be discussed in Chapter 3. And finally, the functionalisation and magnetometry of the nanoparticles investigated in Chapter 4. Each chapter will have its own methods and materials, results and discussions before the final conclusions in Chapter 5.

Chapter 2 Synthesis, mineralisation and characterisation of *Pyrococcus furiosus* ferritin

This chapter focuses on the expression and mineralisation of recombinant *Pyrococcus furiosus* ferritin chosen for its expected thermal stability and increased magnetic susceptibility as reported by Parker et al.[42]

Two mineralisation methods were investigated, one under nitrogen conditions in a double jacketed vessel at 65^{o}C, in order to maintain the correct conditions for the reconstitution of a magnetite (Fe_3O_4) core as described by Okuda et al. [49]. This method was successfully employed by Carreira et al. [23] for the reconstitution of a magnetic cobalt-doped iron oxide core inside commercially available horse spleen ferritin. These particles were cationised and used in bacterial concentration experiments. A similar mineralisation protocol was successfully reported for recombinant *Pyrococcus furiosus* ferritin by Parker et al. [42] with this particle being characterised using size exclusion chromatography (SEC), DLS and TEM [42].

A second method, under aerobic conditions was used to reconstitute a hydrated iron oxide core ($Fe_2O_{3.n}H_2O$) as described by Weeratunga et al. [50] in the mineralisation of *Pseudomonas aeruginosa* bacterioferritin. However, this work did not provide any information on magnetic susceptibility. Using this protocol Le Vay [51] synthesised a mineralised recombinant *E. coli.* bacterioferritin suitable for downstream SAXS.

Using the analytical methods of SEC, DLS and TEM mineralised ferritins from these aerobic and anaerobic protocols were characterised in preparation for downstream bacterial capture functionalisation and advanced biophysical measurement using SAXS.

2.1 Methods and materials

Unless otherwise stated all chemicals were purchased from Sigma (UK)

2.2 Recombinant protein expression

Theory

Recombinant protein expression relies on the DNA transcription and translation machinery found within all living organisms to express a desired protein *in vitro*. Commonly, specialised expression bacteria are used to over express a protein of interest because they are facile to genetically manipulate, grow rapidly and can be induced to produce a large yield of protein. Due to some building blocks of DNA, known as nucleotides, being universal amongst organisms, the DNA of any species can be read by the expression machinery in bacteria. The result is the expression of proteins encoded on that DNA by the bacteria [52].

Genetically modified particles of DNA known as vectors are transformed into the expression bacteria, and under the correct growth conditions will result in the production of the protein, encoded by a gene within that vector. The target protein is then harvested from the bacteria and purified as needed. Induction of expression can facilitate the over expression of the protein, whereby regulatory sequences of DNA known as operons are manipulated to enhance gene expression. For example, the *lac* operon controls the expression of genes required for lactose metabolism[53]. In order to save energy, by not expressing unnecessary proteins, the *lac* operon increases expression in the presence of allolactose, through the binding of allolactose to a repressor protein Lacl. Vectors can be designed whereby the *lac* operon is recombinantly placed downstream of a desired gene, subsequently an allolactose analogue such as isopropyl β-D-1-thiogalactopyranoside (ITPG) is used to release the repressor protein, resulting in the increased binding of transcription machinery and therefore an increased expression of desired protein [54].

Method

Recombinant *Pf* ferritin was encoded in a pOPINF vector (The Oxford Protein Production Facility, UK), transformed into BL21*DE3 *E. coli.* cells purchased commercially (Invitrogen, UK). These bacteria were inoculated on 2YT culture media with 1% cells, selected for using 0.1% 1mg.ml^{-1} Ampicillin for selection. Cell cultures were induced at OD 600 nm using 0.1% 1mg.ml^{-1} ITPG. Shaking cultures were then incubated aerobically for 20 hours at 37^{o}C 190 revolutions per minute (rpm). The cells were harvested from culture media by centrifugation, 20 minutes at 6500 x *g* Avanti J-26XP centrifuge (Beckman Coulter, UK).

The harvested cells were homogenised in 20 ml HEPES buffer (pH 8.6, 0.05 M, 0.1M NaCl) 10 µl benzonase and 2 µg lysozyme were added to facilitate nucleic acid and cell membrane breakdown respectively. The homogenate was then passed through a CF-1 cell disruptor (Constant Systems, UK), for two rounds at 25 kpsi. The resulting lysate was centrifuged to separate protein (147000 x *g* for 1 hour at 4^{o}C, in an Optima L-80 XPUltra centrifuge Beckman Coulter, UK).

The lysate supernatant was then incubated at 95^{o}C for 30 mins on a Thermomiser C heat block (Eppendorf, Germany) and the denatured proteins and thermo-stable protein were then separated by centrifugation for 10 mins at 2879 x *g*, in a PK12R centrifuge (ALC Centrifuges UK). The poly-histidine tag was removed using 3C protease (4-7 mg.ml^{-1}, 1 µl per 200 µg of tagged protein) with samples being incubated overnight at 4^{o}C.

2.3 Measuring protein concentration

Theory

A colourimetric test known as the Bradford assay was used to determine the concentration of protein with the Coomassie blue dye in the Bradford reagent binding to the basic amino acid residues, thus deprotonating the dye and resulting in an absorbance measured with ultraviolet-visible(UV-vis) spectrophotometry at a wavelength λ of 595 nm [55].

Method

To determine protein concentration, a Bradford assay was used according to the manufacturer's protocol. A ferritin reference was diluted from known concentration, indicated on the certificate of analysis (COA), to 1 $mg.ml^{-1}$. Thereafter, 20 µl of the diluted samples were added to 880 µl of water, 100 µl Bradford reagent was added to the sample and left to incubate for 8 mins at room temperature. Samples were loaded into cuvettes and UV-vis absorbance measured on a Ultraspec2100 Pro (Amersham Biosciences, UK) spectrophotometer at λ= 595 nm to determine a reference standard.

2.4 Polyacrylamide gel electrophoresis

Theory

Sodium dodecyl sulphate-polyacrylamide gel electrophoresis (SDS-PAGE) electrical current to separate proteins based on their molecular weight. The polyacrylamide gel forms a resistant matrix; through which the charged proteins pass. Protein samples are prepared with the negatively charged SDS containing a reducing agent thus denaturing the protein, breaking di-sulphide bonds and ultimately creating a peptide with negative charge proportional to length [56]. As described in Figure 2.1, the electrical current running across the gel, causes the peptides to move towards the positively charged cathode with smaller peptide chains moving with little resistance through the gel, conversely larger proteins move with greater resistance thus separating proteins by molecular weight. Standard reference markers are used to qualitatively deduce molecular weight [57].

Method

To determine the presence of ferritin in the expression lysate, SDS-PAGE was according to manufacturer's protocol. Protein samples were mixed 1:1 in 2 x SDS loading buffer (0.25 M tris pH 9.5, 40% w/v sucrose, 4% w/v SDS, 0.002% w/v bromophenol blue and 50 mM 2-mercaptoethanol). To increase effects of denaturation, the samples were then incubated at 95^{o}C for 10 mins. Incubated samples were loaded into precast tris-glycine polyacrylamide gels (Invitrogen, UK). The gel cast was submerged into the electrophoresis tank (Bio-Rad, USA) containing running buffer (10X SDS-PAGE buffer 0.25 M Tris HCl, 1.92 M glycine and 1% w/v SDS; pH 8.3). A current was run across the gel (120 V applied for 30 mins). The resulting gel was removed from the tank and the protein bands were visualised with Coomassie protein stain Instantblue (Invitrogen, UK).

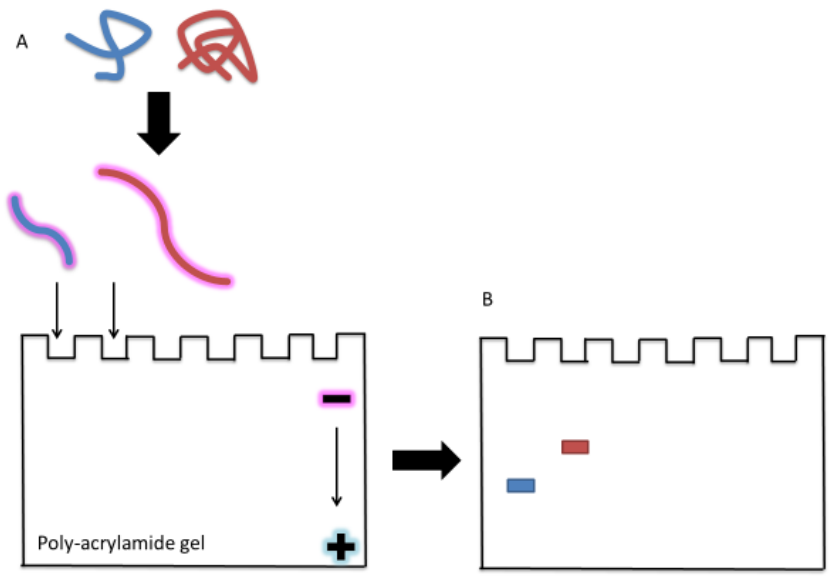

Figure 2.1 Schematic of SDS-PAGE gel electrophoresis

(A) Proteins are incubated at high temperature with reducing agent, with the denatured proteins becoming charged with anionic detergent (SDS). Samples are loaded onto polyacrylamide gel, where migration towards cathode depends on dimension and SDS associated charge. (B) Result is smaller proteins (blue) migrate further than larger proteins (red), visible on the gel as bands, once stained.

2.5 Protein purification

2.5.1 Size exclusion chromatography

Theory

SEC purifies protein on the basis of hydrodynamic volume or particle size [58] Figure 2.2. The protein in aqueous buffer is loaded onto a column packed with particles of known porosity; small proteins diffuse into the particles relative to size, while larger proteins do not. As mobile solvent buffer is passed over the column, the proteins or particles are washed from the column. Elution is detected via UV-vis with larger proteins eluting from the column first, smaller proteins taking longer to elute as they are absorbed into the porous matrix, smaller molecules such as salts elute last as they diffuse freely into the matrix. When compared with known reference standards this technique can estimate the molecular weight of a protein, however this measurement is relative to conditions of the column and buffer used [58].

Method

SEC was performed using the AKTA FPLC purification system (GE Lifesciences, USA). 5 ml samples were loaded onto a Superdex200 (S200) column at flow rate of 1 $ml.min^{-1}$ at room temperature. S200 was chosen for its high resolution and an exclusion limit of ~1.3×10^6.

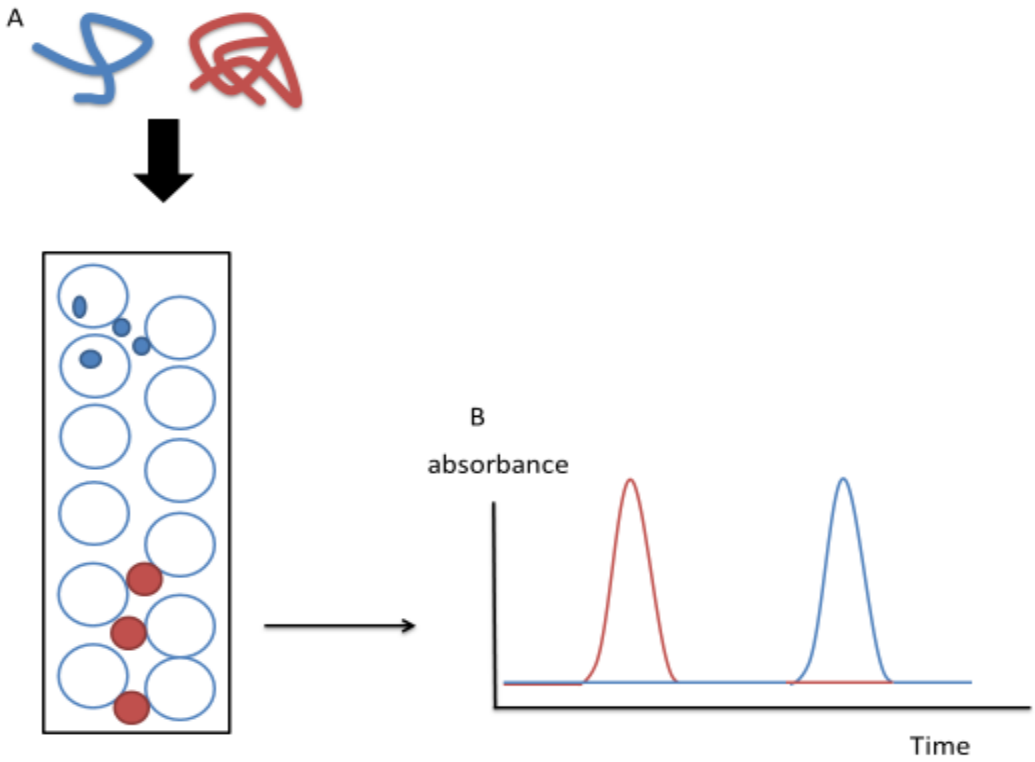

Figure 2.2 Schematic of size exclusion chromatography

(A) Proteins are loaded onto a column. Porous matrix absorbs smaller proteins (blue), they elute from the column later than larger proteins (red). Therefore proteins separated based on hydrodynamic volume or size (B) UV-vis absorbance of eluting proteins results in a chromatogram.

2.5.2 Ion exchange chromatography

Theory

Another protein separation technique, ion exchange chromatography (IEC), purifies proteins based on surface charge associated with those proteins. The matrix within ion exchange columns is oppositely charged, and proteins bind to the matrix via electrostatic interactions. An ionic gradient is created by the gradual increase of salt concentration in a mobile solvent buffer, this disrupts the electrostatic interactions resulting in the elution of protein from the column, Figure 2.3. Those proteins with less surface charges are removed by lower salt concentrations, with the salt ions competing for the matrix. Increased salt concentrations elute the proteins bound with a higher affinity and the result is a specific elution profile measured by UV-vis spectrometry [53].

Method

IEC was performed using the AKTA FPLC purification system. 50 ml samples were loaded onto a column containing a cationic matrix of ANX Sepharose 4 Fast Flow. A salt gradient, from 10 mM to 750 mM, over 18 column volumes of HEPES buffer pH 8.6 was passed over the column at a flow rate of 5 $ml.min^{-1}$ at room temperature.

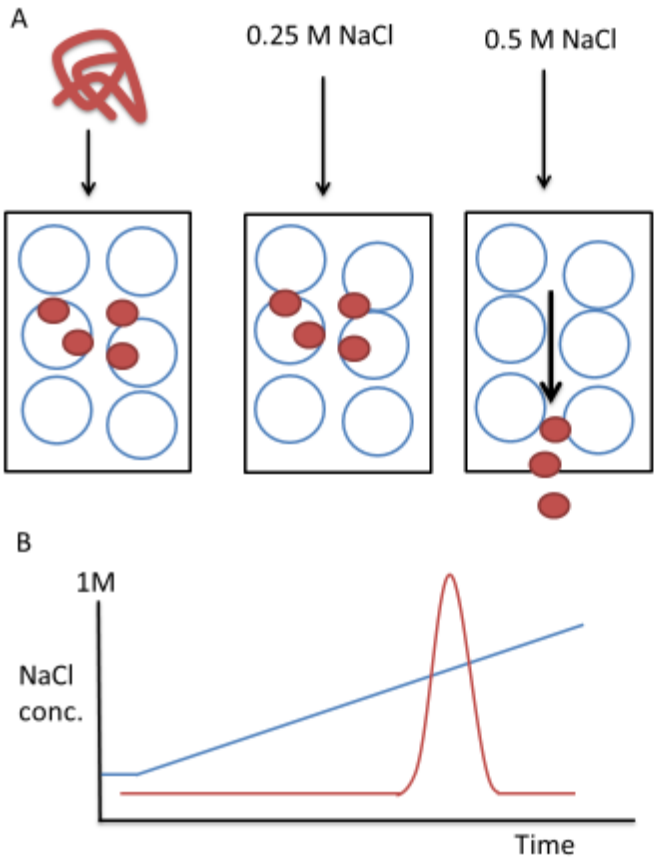

Figure 2.3 Schematic of ion exchange chromatography

(A) Proteins are loaded onto the column and bind to the oppositely charged matrix; an increasing salt concentration gradient is passed over the matrix. At a specific isoelectric point, the salt concentration disrupts the electrostatic interactions between particle and matrix resulting in the elution of the protein from the column. (B) UV-vis absorbance of eluting proteins results in a chromatogram.

2.6 Protein characterisation and analysis

2.6.1 Dynamic light scattering

Theory

DLS uses the scattering of light to determine particle dimensions. Particles in solution interact with each other or solvent particles. These interactions transfer a near constant energy causing the particles to move randomly. Smaller particles are heavily influenced by this energy transfer and will move in solution more rapidly, larger particles will move more slowly with the resulting phenomenon known as Brownian motion [59]. As a known wavelength of light irradiates a sample, fluctuations in signal intensity are detected as the particles move in solution and a diffusion constant can be determined from the Brownian motion using the Einstein–Smoluchowski Equation 2-1) where D is the translational diffusion coefficient, μ is the ratio of a particles velocity in relation to force, also known as mobility, k_B is the Boltzmann constant, and T is absolute temperature.

$$D = \mu k_B T$$

Equation 2-1

The Einstein-Stokes equation is then used to determine a spherical particle's hydrodynamic diameter (Equation 2-2) where η is the dynamic viscosity of the sample and r is the radius of spherical particle.

$$D = \frac{k_B.T}{6\pi\eta r}$$

Equation 2-2

Particle size is represented as hydrodynamic diameter, the hypothetical size of a hard sphere that diffuses in the same fashion as that of the particle being measured.

Equally, particle size can be represented as the Z-average, the mean hydrodynamic diameter derived from the cumulate particle correlation analysis. For a completely monodisperse sample, the Z-average will be equal to the mean diameter.

Method

In order to measure particle size distribution and sample polydispersity, DLS was used. Samples were adjusted to a concentration of 1 $mg.ml^{-1}$ suspended in HEPES buffer and passed through a 220 nm pore to remove any high intensity scattering debris. DLS was performed on a Zetasizer Nano-ZS (Malvern Instruments, UK). The Zetasizer self-calibrates to determine how many measurements are required based on sample polydispersity, with a total of 9 -15 measurements collected to achieve an accurate correlation depending on the molecular aggregation behaviour of the sample.

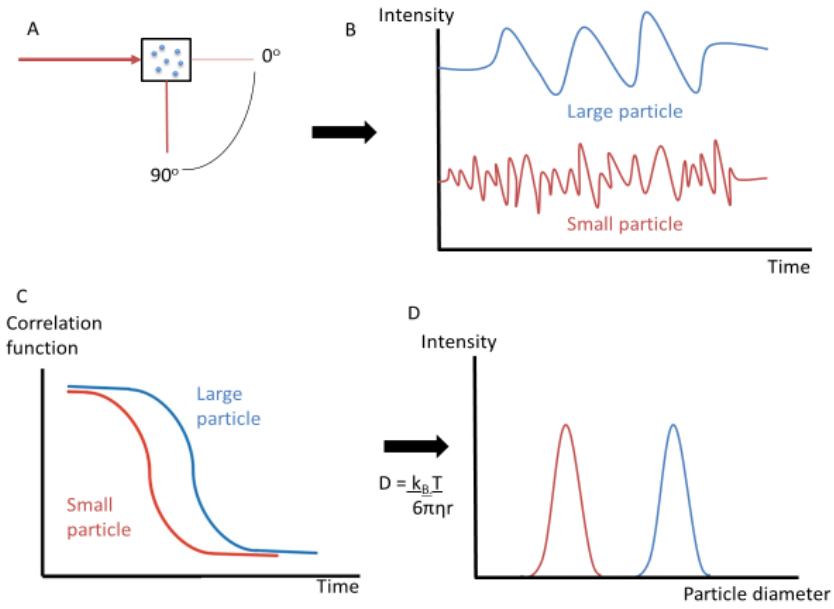

Figure 2.4 Schematic of dynamic light scattering measurement

(A) A laser illuminates the sample, particles moving in solution due to Brownian motion scatter the light which is measured at a specific angle (B) the signal intensity of scattered light is plotted against time, larger particles (blue) scatter at high intensity than smaller particles (red) (C) correlation coefficient applied to signal against time produces a correlogram. A monodisperse sample will produce a sigmoidal decay (D) distribution of particle size against intensity is calculated from the correlation coefficient using the Einstein-Stokes equation.

2.6.2 Transmission electron microscopy

Theory

High resolution imaging of a sample can be achieved using TEM. In this technique the sample is irradiated with a uniform electron beam with a wavelength around 50 pm and an energy between 60-150 keV allowing the resolution of images in order of 0.2-0.5 nm. The electron beam originates from a tungsten filament inside an electron gun and travels through vacuum, directed by electromagnetic lenses so that the beam illuminates the sample. The scattered beam is then focused through projector lenses onto a detector [60].

The atoms within the sample scatter the electron beam through elastic and inelastic scattering, providing a contrast image on the detector, known as bright field microscopy. Organic matter with low atomic number fails to scatter enough electrons to contrast against the background and are therefore must be stained with high atomic number metal-based stains, thus providing a negative contrast for a qualitative characterisation of image.

Methods

Samples were prepared on copper support grids, UV discharged under vacuum in a glow discharger (Lecia, Germany). Samples were diluted to a concentration of 0.2 $mg.ml^{-1}$ and 5 µl was applied to discharged grid. Grids were then washed with sterile water before staining with 1% phosphotungstic acid (PTA). Grids were viewed on a Tecnai 1200 Spirit BioTwin TEM (Thermo Fischer, USA) fitted with a tungsten filament. Images were recorded on an Eagle 4k x4k CCD camera (Thermo Fisher, USA). Particle size analysis was conducted using Image J [61].

2.6.3 Inductively coupled plasma-optical emission spectroscopy

Theory

Inductively coupled plasma-optical emission spectroscopy (ICP-OES) is an atomic analytical technique designed to detect trace elements within a sample down to parts per billion (ppb) by measuring the electromagnetic energy released by electrons as they change energy state, as described in Figure 2.5 [62]. Samples are vapourised and heated in a plasma to ensure the constituents are single atoms. With this energy increase, the electrons within the sample move to higher energy levels. The excited electrons energetically favour being in their ground state and as they return to lower energy states, they emit photons of discreet wavelength, characteristic to specific elements or ions. The intensity of light emitted at certain wavelengths, compared to element calibration standards can be used to calculate the concentration of trace elements down to ppb [62].

Method

ICP-OES analysis was achieved using an Agilent 710 ICP-OES spectrometer (Agilent, USA) in the Earth Sciences Department at the University of Bristol. Samples at known concentrations were digested in 50% v/v nitric acid to release any bound trace elements and auto-injected onto the nebuliser, along with 5 calibration standards. The spectrometer reads each sample via UV-vis, in triplicate to provide a mean and standard deviation (SD). A background sample was measured to subtract from the samples before analysis.

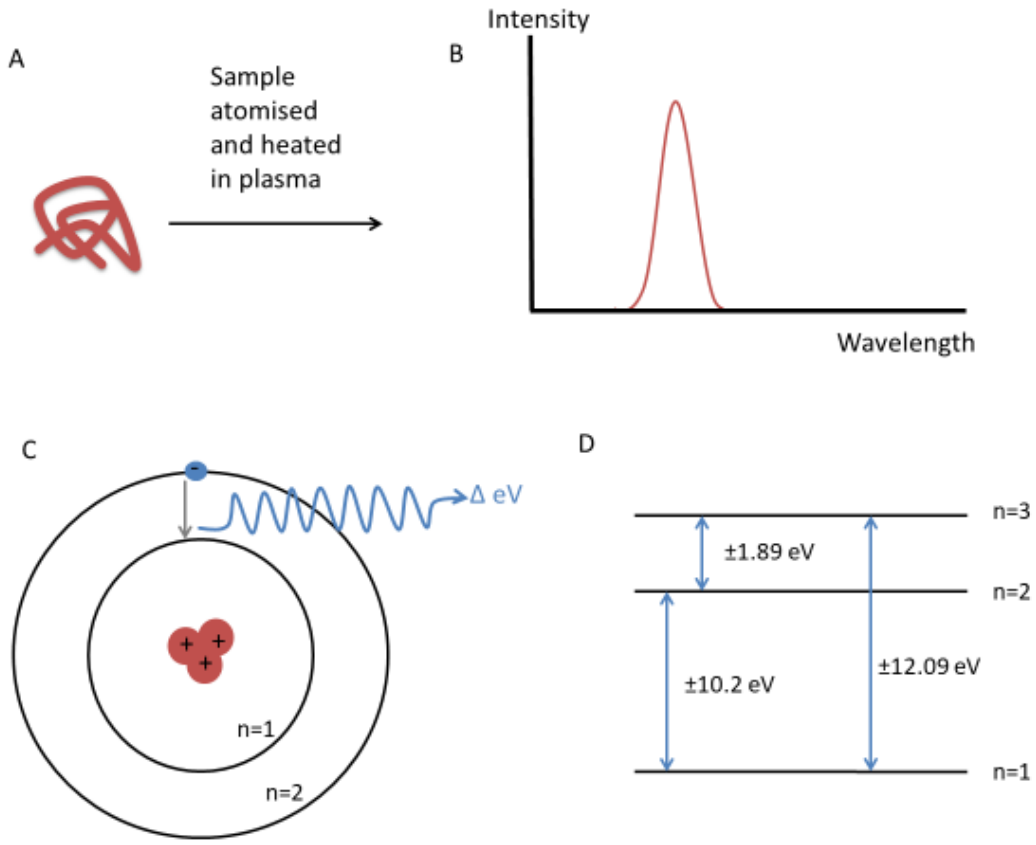

Figure 2.5 Schematic of ICP-OES measurement

(A) Sample atomised and heated in order to excite electrons; release of wavelength measured by spectrometer (B) signal intensity plotted against emitted wavelength. (C) Diagram of excited electron returning to ground energy state emitting energy in the form of photon, (D) table describing energy change through electron shift between energy states.

2.7 Ferritin mineralisation

2.7.1 Anaerobic *Pf* ferritin mineralisation

Method

Reconstitution of a magnetite Fe_3O_4 core inside the *Pf* ferritin was achieved using a protocol first described by Meldrum et al.[63] and optimised by Okuda et al.[49]. 225 mg of purified and degassed apo-ferritin was added to 75 ml HEPES buffer pH 8.6 (0.05 M, 0.1 M NaCl) to achieve a final concentration of 3 $mg.ml^{-1}$. The reaction was performed in a double jacketed vessel at 65ºC, and under nitrogen conditions. 30.3 ml of 25 mM ammonium iron sulphate hexahydrate was added at a rate of 0.15 $ml.min^{-1}$ with a Titrando 907 syringe pump (Metrohm, UK). Simultaneously, 30.3 ml of 8.33 mM hydrogen peroxide was added via titration to reduce the synthesis of hydrated iron oxide. Mineralised ferritin solution was separated from precipitates using centrifugation for 30 minutes at 4350 x *g*, at 4ºC in a PK12R centrifuge (ALC Centrifuges UK). The supernatant was passed through a 220 nm syringe filter and dialysed overnight in a HEPES buffer pH 8.6 (0.05 M, 0.1 M NaCl) containing 1 mM tris(2-carboxyethyl) phosphine (TCEP) and purified using SEC.

2.7.2 Aerobic *Pf* ferritin mineralisation

Method

Reconstitution of a hydrated iron III oxide core, $Fe_2O_3\,nH_2O$, was achieved aerobically using the protocol described by Weertunga [50] and later used by Le Vay [51] to characterise Fe^{2+} loading in bacterioferritin. Ammonium iron sulphate hexahydrate (AIS) solution containing 0.05% concentrated hydrochloric acid and 1 mM tris(2-carboxyethyl) phosphine (TCEP) was prepared anaerobically. Aliquots of 150 mM AIS solution were added to aliquots of apo-ferritin aerobically to make a total volume of 10 ml and stirred for 15 mins. Mineralised ferritin solution was separated from precipitates using centrifugation for 30 minutes at 4350 x *g*, at 4ºC in a PK12R centrifuge (ALC Centrifuges UK). The supernatant was passed through a 220 nm syringe filter and dialysed overnight into a HEPES buffer pH 8.6 (0.05 M, 0.1 M NaCl) containing 1 mM tris(2 carboxyethyl) phosphine (TCEP) and purified using SEC.

2.8 Results

2.8.1 Expression and purification of *Pyrococcus* ferritin

The over-expression of recombinant *Pyrococcus furiosus* (*Pf*) ferritin protein was required in order to produce the recommended yield (225-300 mg) for downstream mineralisation and advanced structural characterisation. SDS-PAGE was utilised to visualise the success of recombinant protein expression in BL21*(DE3) *E. Coli.* Initially there was strong evidence of the induced expression of a protein upon addition of ITPG, demonstrated by the bands indicated on Figure 2.6A which appear at an expected molecular weight for *Pf* ferritin monomers ~20 kDa, consistent with particle size analysis by Parker et al. [42]

After the cell lysate incubation at 95^{o}C, any denatured thermo-susceptible proteins were removed from the lysate through centrifugation. This left the thermostable proteins in solution, visible on the SDS-PAGE analysis, evident by a cleaner lane seen in “sample loaded onto SEC column” in Figure 2.6B. These samples were further purified by SEC, Figure 2.7.

Due to the large molecular weight of the *Pf* ferritin (~480 kDa) purifications were undertaken on a S200 SEC column, chosen for its high resolution and an exclusion limit of ~1.3 x 10^{6}. Assembled ferritin icositetramers with a molecular weight of 480 kDa are expected to be absorbed into the matrix and not elute in the void volume. A UV trace chromatogram of the purification was recorded to visualise elution peaks and compared with a commercially available reference, horse spleen ferritin, Figure 2.7A.

Eluting fractions from the first retention peak at 59.81 ml were collected and analysed via SDS-PAGE. This indicated the presence of the desired protein with the expected molecular weight bands seen in Figure 2.7B. Elution fractions from the other retention peaks at 78.67 ml and 107.77 ml were also analysed by SDS-PAGE.

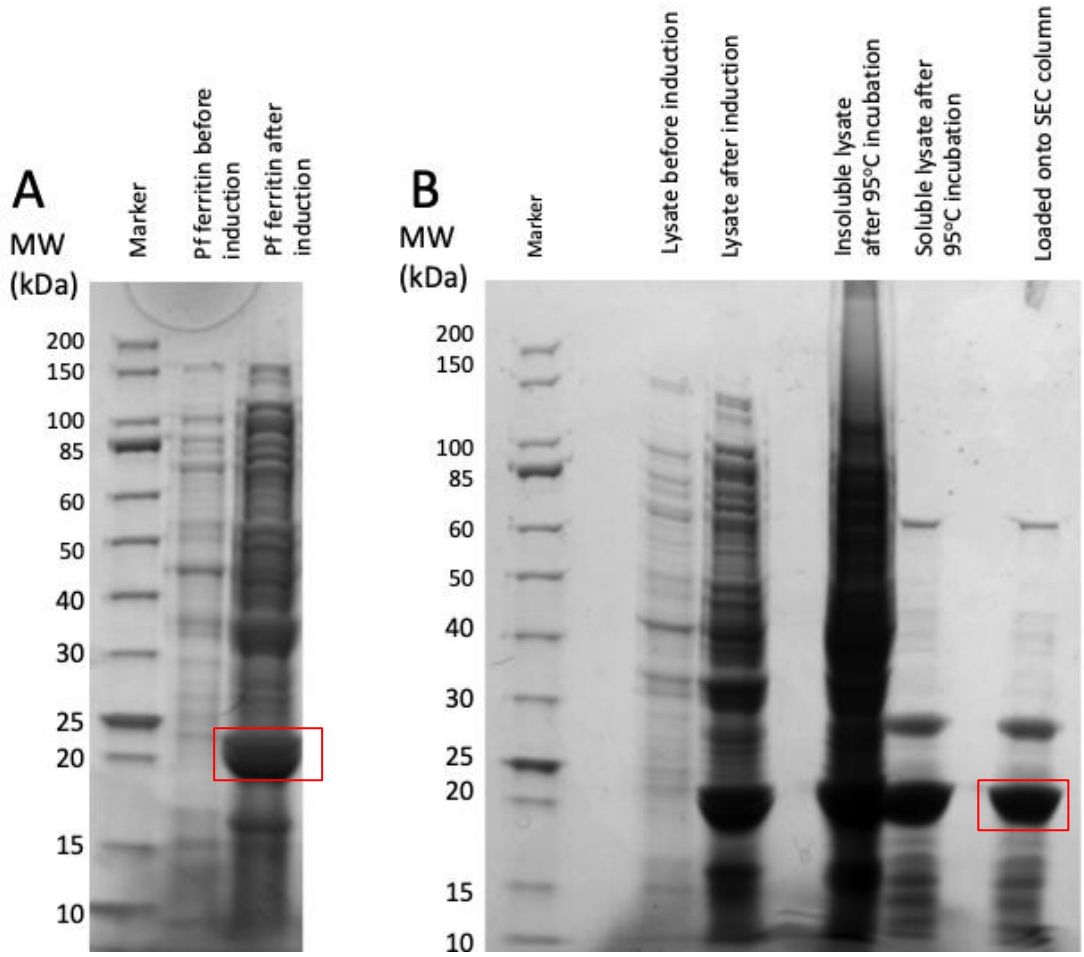

Figure 2.6 SDS-PAGE analysis of induced *Pf* ferritin expression

(A) SDS-PAGE analysis of induced ferritin expression in BL21*(DE3) cells. *Pf* ferritin with N-His tag expressed in BL21*(DE3), before induction after induction. Desired protein band indicated in red box.
(B) SDS-PAGE analysis of purification of N-His tagged *Pf* ferritin. BL21*(DE3) lysate before induction and after induction with IPTG. Lysate was incubated at 95^{o}C. Insoluble lysate fraction after incubation and soluble fraction, incubated with 3C-protease overnight to remove N-His tag ultimately loaded onto SEC. Desired protein band indicated in red box.

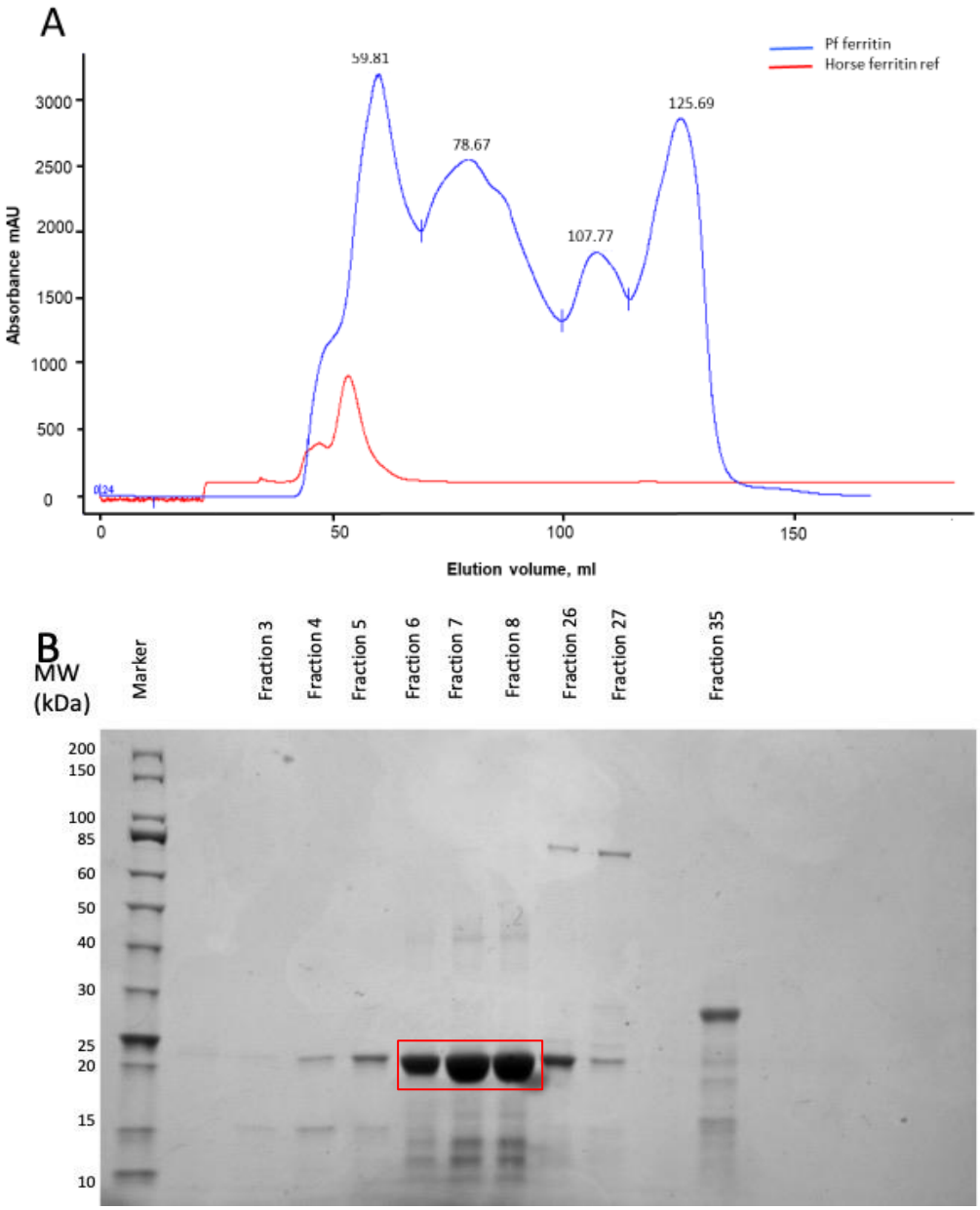

Figure 2.7 UV chromatogram from SEC with SDS-PAGE analysis

(A) UV chromatogram from S200 size exclusion. *Pf* ferritin protein lysate purified by incubation at 95°C (blue), protein standard horse spleen ferritin reference (red) both run at 1 ml.min^{-1}. (B) SDS-PAGE analysis of s200 Size exclusion chromatography purification of *Pf* ferritin. Fraction number indicated on image, fractions 3-8 are from the peak at 59.81 ml seen on chromatogram. Fractions 26 and 27 are from 78.67 ml. Fraction 35 is from 107.77 ml. The expected molecular weight of *Pf* ferritin is approximately 20 kDa. Desired protein band indicated in red box.

2.8.2 Particle characterisation

Comparisons between the chromatograms for the reference horse spleen ferritin and *Pf* ferritin lysate provides a strong indication that the elution retention peak at 59.81 ml contained the protein of interest. However, due to the presence of a shoulder seen on the peak at 50 ml, further analysis was required to resolve the protein from larger proteins or potential aggregates. DLS was carried out to elucidate the hydrodynamic diameter of the particles in the peak. DLS data for the two fractions from the size exclusion are shown in Figure 2.8. As the *Pf* ferritin contains no iron it is referred to as apo-ferritin with apoPf3 from fraction 3 seen eluting at 50 ml on the chromatogram in Figure 2.7A and apoPf7 from fraction 7 eluting at 59.81 ml.

A small number of large particles can generate higher scattered light intensities than a greater number of small particles and therefore skew the size distribution analysis. Therefore, three hydrodynamic diameter measurements were compared, these being hydrodynamic diameter as a percentage of volume, particle number and intensity shown alongside the correlation coefficient.

Considering the apoPf3 sample, the multimodal hydrodynamic intensity distribution coupled with uneven peak distributions of hydrodynamic volume and particle number can be seen in Figure 2.8. This provides evidence of sample polydispersity and heterogeneity. Conversely, the consistent hydrodynamic diameter peak distributions for apoPf7 in all three measurements, indicate a high level of monodispersity and homogeneity of sample. Figure 2.8 also shows the correlation coefficient as a function of time, the irregular decay in correlation curve seen for apoPf3 is representative of polydispersity. In contrast the sigmoidal decay evident in apoPf7 is a good example of monodispersity.

The DLS data report, Table 2-1, supports the peak distributions seen for apoPf3 and apoPf7. The earlier eluting apoPf3, with an increased hydrodynamic volume from aggregation contributing to its elution at 50 ml, showed a hydrodynamic diameter of 23.65 nm with a Z-average diameter of 152.6 nm and an increased polydispersity index of 0.49. Taken together these results are evidence for the apoPf3 sample being homogenous and polydisperse. Conversely, the data for apoPf7 show a mean

hydrodynamic diameter of 11.65 nm, with a z average of 16.08 nm,a polydispersity index of 0.08 is indicative of a much more monodisperse sample.

The monodisperse particles with lower hydrodynamic radii and a lower polydispersity index were chosen for further characterisation using TEM, Figure 2.9. This was used to qualitatively and quantitatively consolidate the characterisation evidence from DLS. Spherical particles are evident in the TEM analysis, seen as either entirely white circles or white rings with darker centres. The particle diameter frequency distribution of 99 particles (using ImageJ) estimated a mean diameter of 12.71 ± 1.00 nm, supporting DLS measurements and in line with a 12 nm diameter reported in the literature [42].

Table 2-1 Dynamic light scattering size parameters

Dynamic light scattering size parameters. Comparison of fractions from SEC, apoPf3 retention peak at 50 ml and apoPf7 retention peak at 59 ml.

				Volume Distribution			
	Number Mean d (nm)	Z-average d (nm)	PDI	Peak 1 Mean d (nm)	Peak 1 Area Percent	Peak 2 Mean d (nm)	Peak 2 Area Percent
apoPf3	23.65	152.60	0.49	303.97	86.30	42.17	13.70
apoPf7	11.65	16.08	0.08	17.51	100.00	0.00	0.00

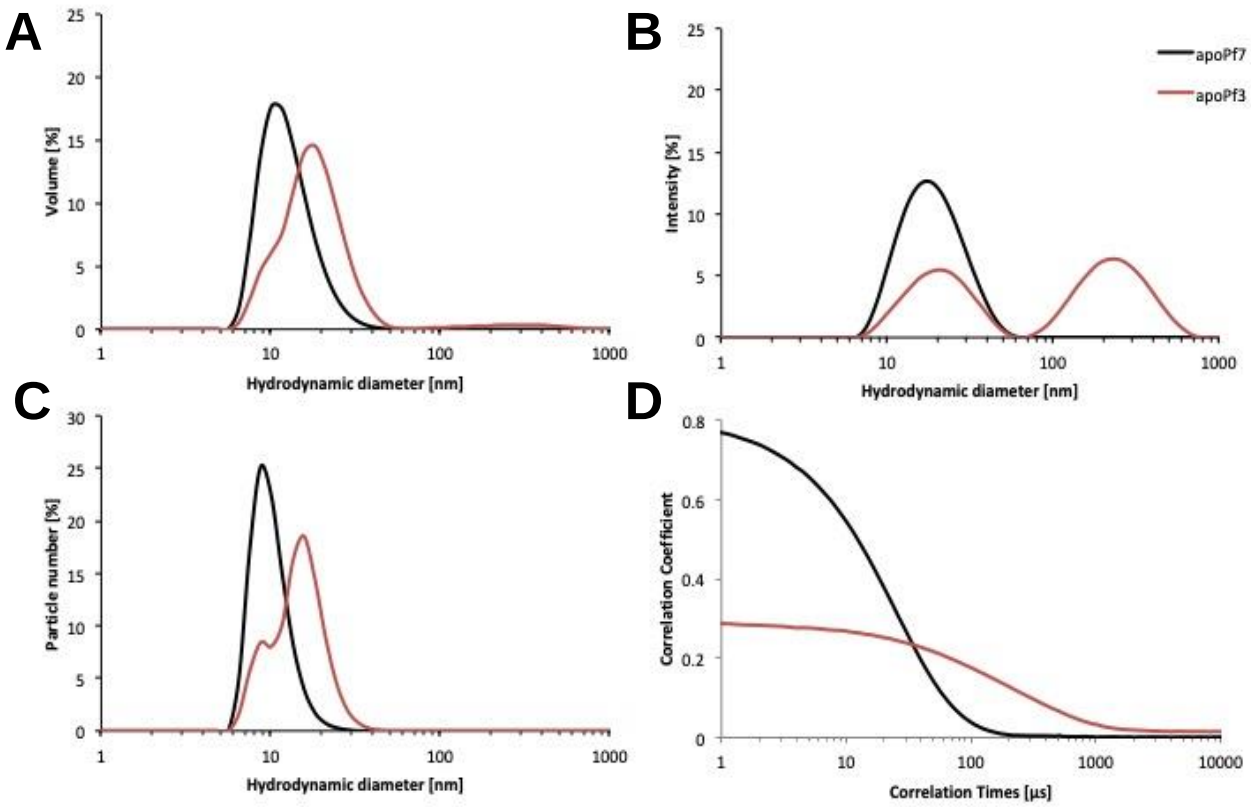

Figure 2.8 Dynamic light scattering size measurements

Hydrodynamic diameter measurements for the apoPf3 fraction that eluted at 50 ml (red) and apoPf7 fraction that eluted at 59 ml (black). Hydrodynamic diameter as volume of sample (A), intensity of signal (B), and mean particle number(C) and correlation coefficient (D).

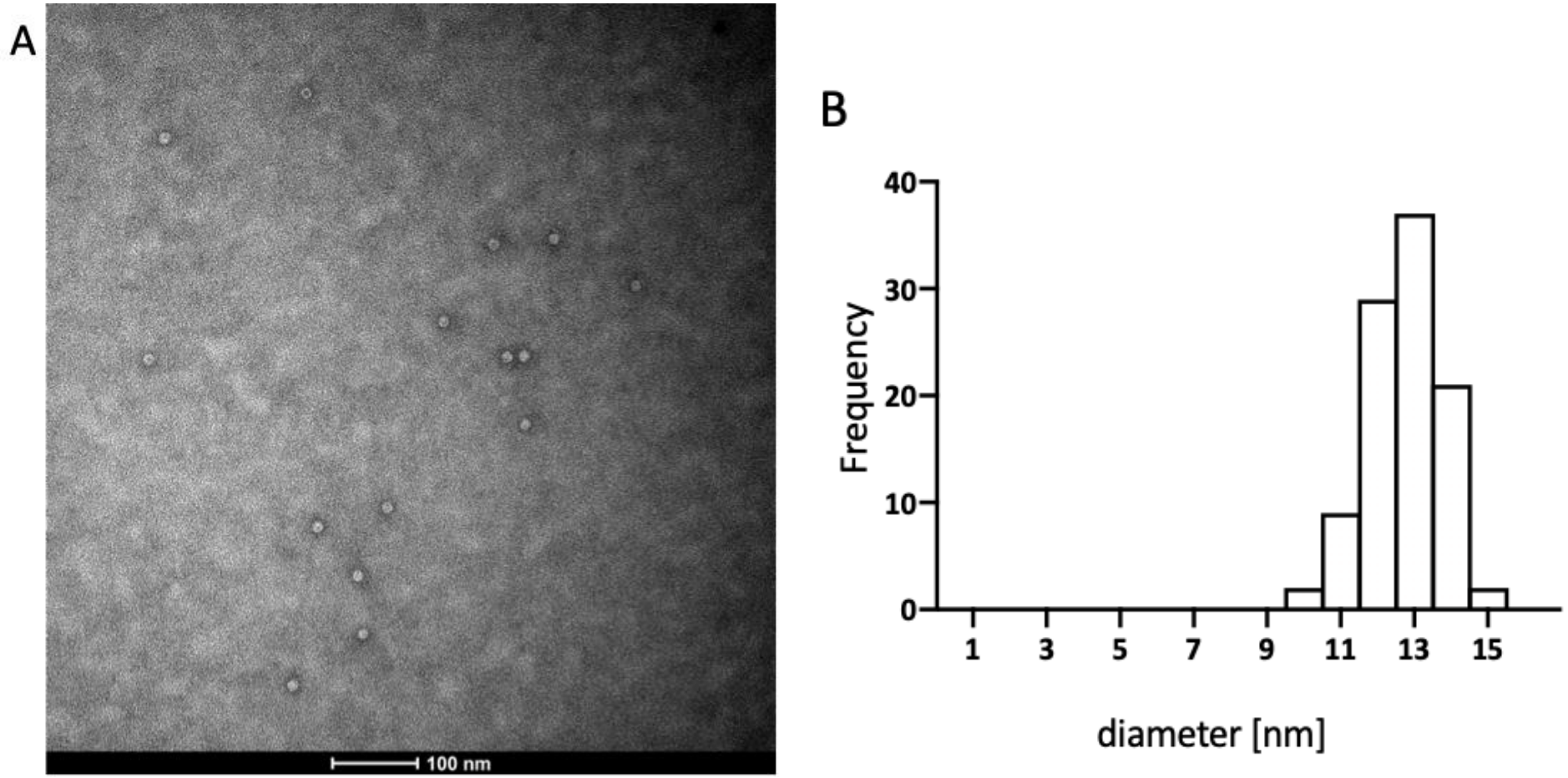

Figure 2.9 Transmission electron microscopy of apoPf7

(A) Example image of apoPf7 from S200 SEC fractions at 59.81 ml, stained with 1% PTA, magnification x49000, (B) Particle diameter frequency distribution analysis indicates a mean diameter of 12.71 ± 1.00 nm

The combination of results from DLS and TEM analysis strongly suggest that particles that eluted from the SEC peak at 59.81 ml are *Pf* ferritin particles of a high monodispersity with little to no aggregation. However, this analysis was not able to identify if the isolated ferritin contained iron. Therefore, ICP-OES analysis was used to identify the initial iron concentration shown in Table 2-2. A sample of 1mg.ml^{-1} apoPf analysed using ICP-OES identified a mean of 25.06 ppb iron present using six different characteristic emission wavelengths identified for iron. This is an equivalent to 2.5e^{-8} g.ml^{-1} and was calculated as 49.83 Fe atoms per ferritin molecule. An even distribution of iron was assumed.

Table 2-2 ICP-OES analysis of apoPf7

Average iron atoms per ml sample measured in ppb, mean calculated from six iron associated wavelengths

Wavelength (nm)	Fe (ppb)	SD (ppb)
Fe 234.350	26.31	2.22
Fe 238.204	25.83	2.19
Fe 239.563	22.57	3.47
Fe 259.940	25.00	2.38
Fe 260.709	24.38	4.17
Fe 261.187	26.24	2.54

2.8.3 Anaerobic mineralisation

The homogenous and monodisperse fractions from the SEC retention peak at 59.81 ml were pooled and used for iron core mineralisation. The samples were incubated with ammonium iron sulphate, and hydrogen peroxide in a double jacketed vessel, at 65^{o}C under nitrogen conditions in order to reconstitute a magnetic iron oxide core inside the ferritin cages. Samples were subsequently dialysed and analysed by DLS and TEM. Ferritin molecules after mineralisation steps are referred to as mineralised ferritin *Pyrococcus furiosus* (mfPf).

DLS was employed to quantitatively analyse hydrodynamic diameter and particle monodispersity of the post reaction solution, Figure 2.10. The distribution of hydrodynamic diameter measurements of both volume and particle number indicates that the sample does not contain monodisperse particles with the expected 12 nm diameter. Equally, a large and uneven distribution evident in hydrodynamic diameter intensity is an effect of larger particles in solution. The correlation coefficient as a function of time indicates a sigmoidal decay possibly due to a homogeneity of aggregation. From the DLS report, the solution contained particles of a mean diameter at 11.56 nm, however the *Z*-average was significantly larger at 62.67 nm.

To further qualitatively visualise the particle shape and detect aggregation electron, microscopy was employed. Aggregation of whole particles with large masses being visualised in Figure 2.11. There were very few frames containing evidence of monodisperse particles free in solution, this was illustrative of the sample polydispersity reported by the DLS measurements.

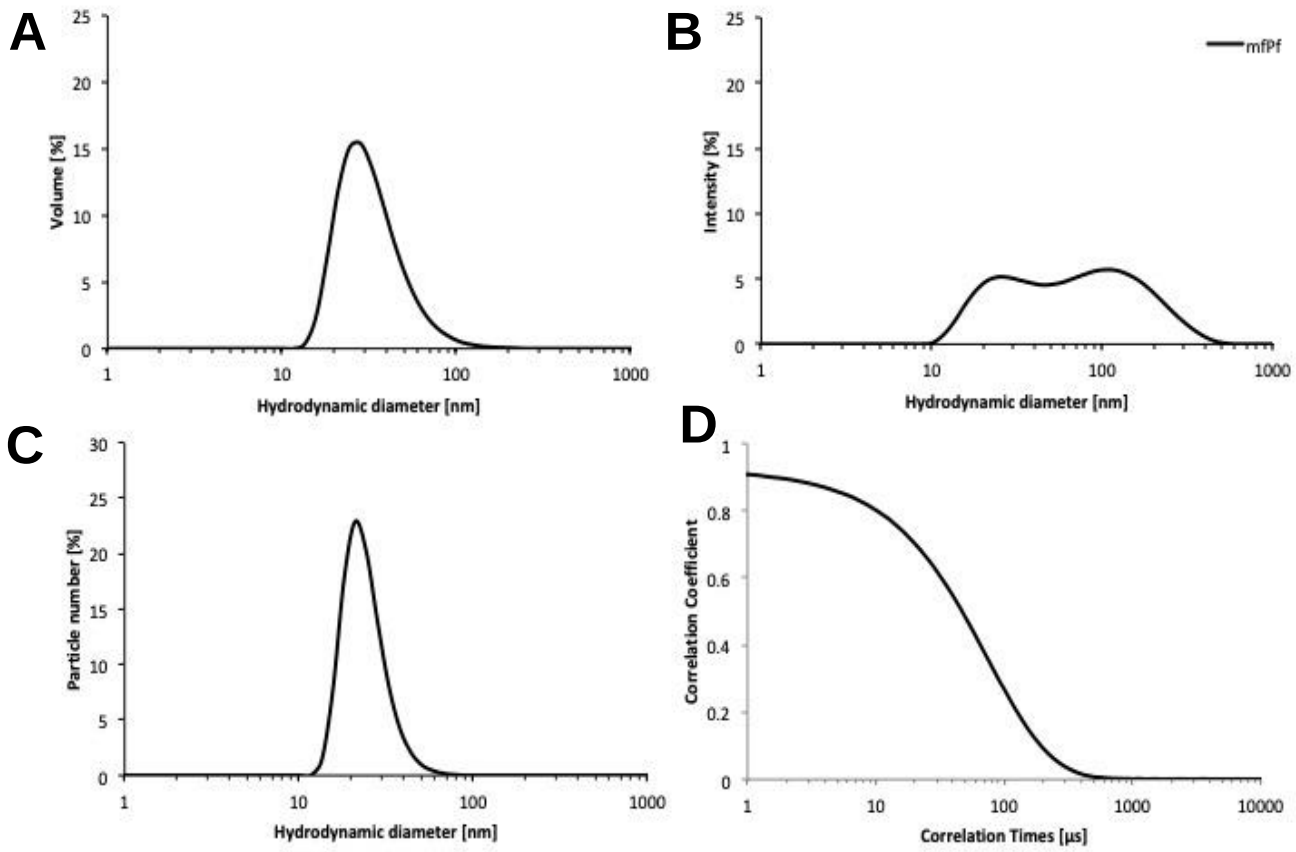

Figure 2.10 Dynamic light scattering size analysis of mfPf

Hydrodynamic diameter measurements of anaerobically loaded *Pf* ferritin reaction solution after dialysis. Hydrodynamic diameter as volume of sample (A), intensity of signal (B), and mean particle number (C) and correlation coefficient (D)

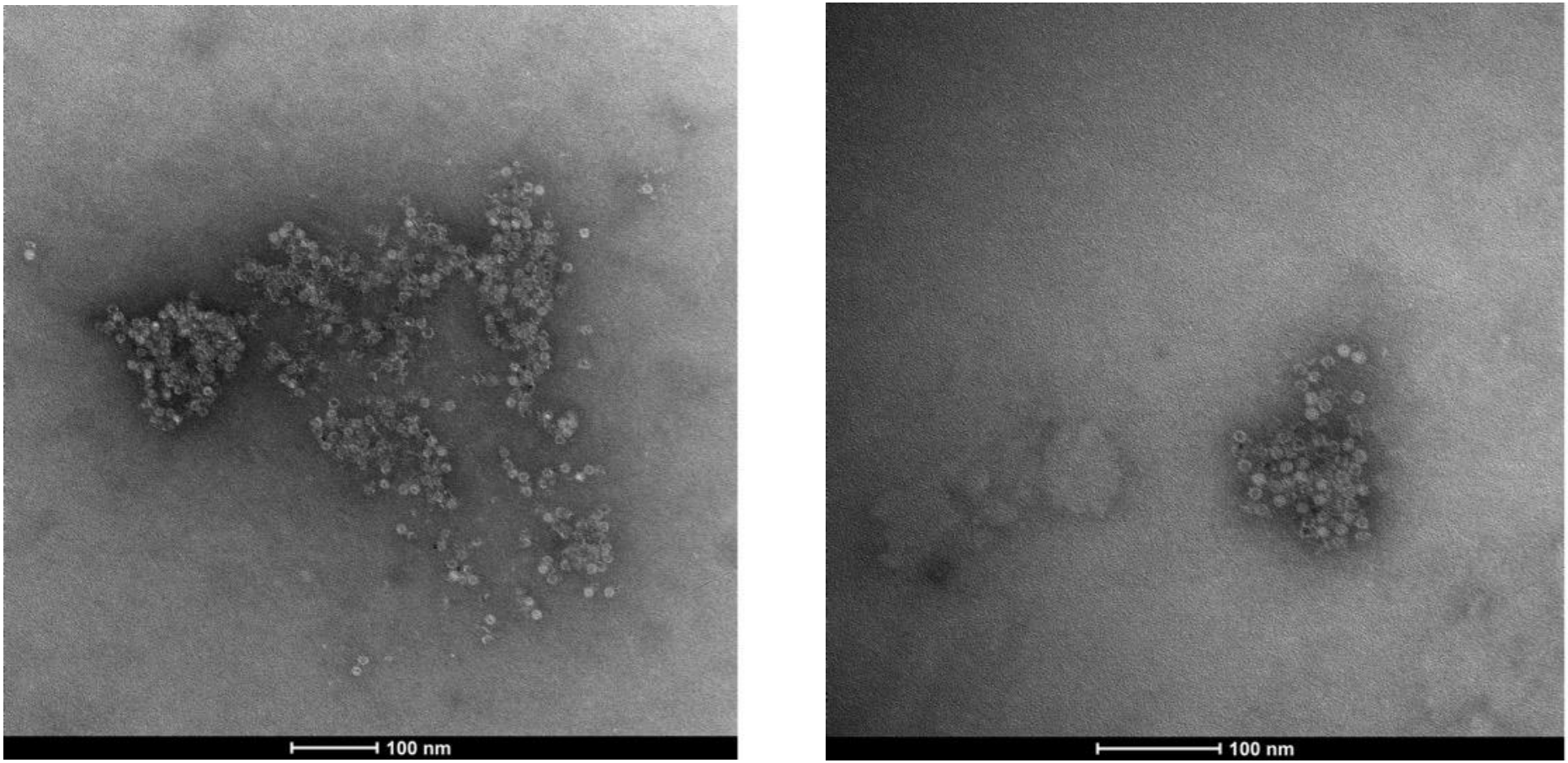

Figure 2.11 Transmission electron microscopy of mfPf aggregation

TEM of mfPf mineralisation solution stained with 1% PTA, at x49000. Both images show examples of aggregation of ferritin-like particles.

The DLS and TEM data suggest that the mineralisation process contributes to particle aggregation. Further investigation was required to purify monodisperse mineralised particles from aggregate masses in the polydisperse post mineralisation solution.

Firstly, ion exchange chromatography (IEC) was used to purify the mfPf cages, by separating monodisperse particles from aggregates and waste particles by surface charge. ANX Sepharose was chosen for its positive charge, with negatively charged ferritin particles expected to bind. Particles with iron bound to the exterior, protein aggregates or iron aggregates would not bind to the cationic matrix of the column. Therefore, these particles will elute from the column at low salt concentrations in the wash buffer. The mfPf nanoparticles that were fully formed and monodisperse would bind to the cationic matrix and elute at a specific salt concentration. UV chromatograms of the IEC elution profile can be seen in Figure 2.12. Here two elution peaks are evident at 495.05 ml, around 400 mM NaCl and 606.85 ml, at 480 mM NaCl.

To characterise the elution profile seen on the IEC chromatogram, fractions from both retention peaks were concentrated and subject to SEC on a S200 column. Here the characteristic elution profile of 480 kDa ferritin nanocages is not as prominent as seen in previous SEC measurements. The UV chromatogram for each of the concentrated fractions, mfPf40 from fractions in the peak at 495.05 ml, and mfPf68 from fractions in the peak at 606.65 ml, can been seen in Figure 2.13. Both chromatograms report a peak at 57.91 ml, and at 106.90 ml.

Included is a standard reference trace with a peak at 99.35 ml from the elution of 13.7 kDa ribonuclease, a molecule smaller than a single 20 kDa ferritin subunit. Based on this evidence, fractions from the peak at 106.90 ml were not further characterised. Protein concentration measurements of the peaks at 57.91 ml were considered too low yield for functionalisation, with mfPf40 measured at 0.526 $mg.ml^{-1}$ and mfPf68 at 0.108 $mg.ml^{-1}$. Recovery of this protein was inappropriate for downstream characterisation and functionalisation.

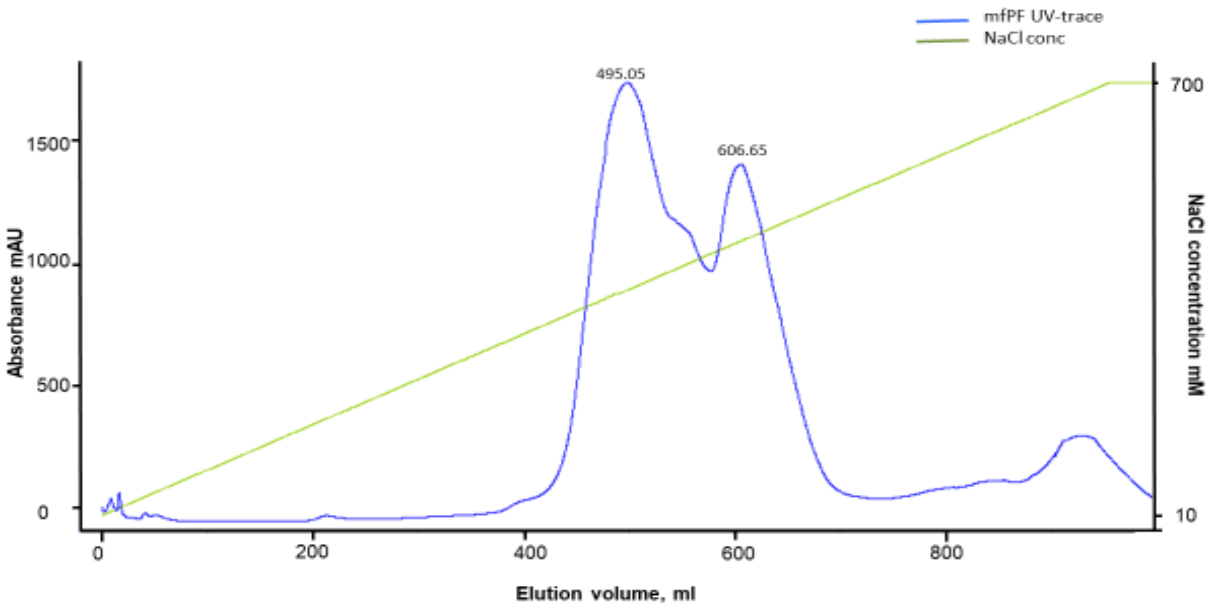

Figure 2.12 UV chromatogram of mfPf ion exchange

50 ml mineralisation solution loaded onto cationic matrix, at a flow rate of 5ml.min^{-1} for 18 column volumes, elution of sample at 495.05 ml, 400 mM NaCl. Elution of sample at 606.85 ml, 480 mM NaCl.

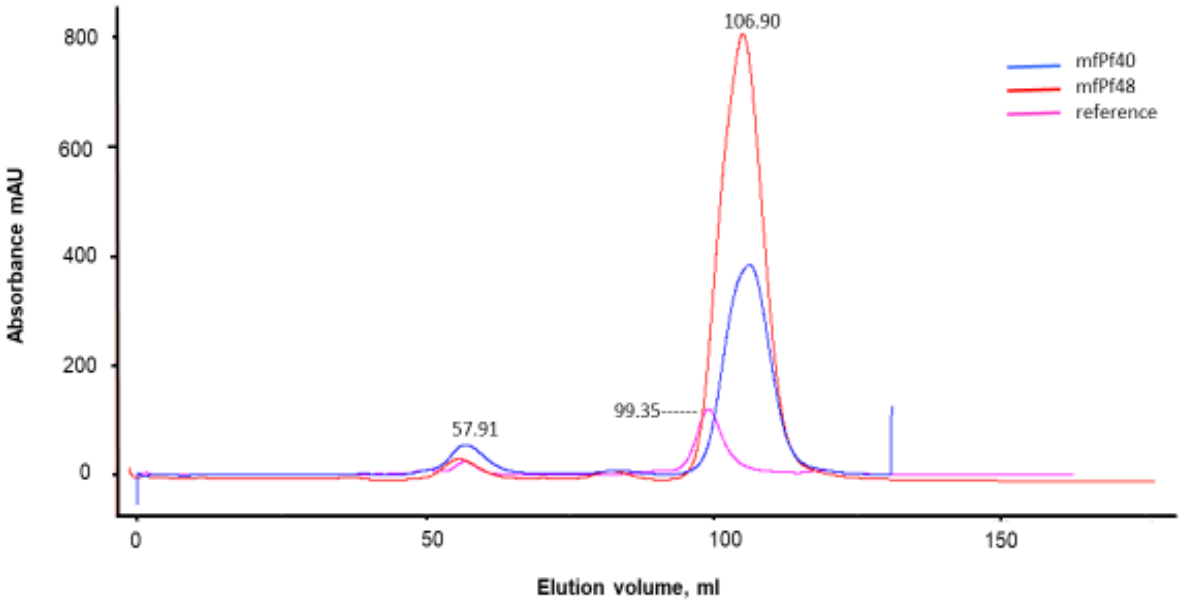

Figure 2.13 UV chromatogram of mfPf size exclusion

S200 size exclusion, with mfPf IEC elution fraction from 495 ml (mfPF40, blue) and mfPf elution from 606.85 ml (mfPf48, red). The mfPf40 peak eluting at 57.91 ml (0.526 mg.ml^{-1}) Two peaks were seen for each sample one at 57.91 ml, and another at 106.90 ml. UV trace of two commercially available reference proteins (reference, pink) with horse spleen ferritin (480 kDa) eluting at 57.91 ml and ribonuclease eluting at (13.7 kDa) at 99.35 ml.

2.8.4 Aerobic mineralisation

The anaerobic mineralisation protocol was deemed unsuitable for achieving an appropriate yield of mineralised *Pf* ferritin for downstream functionalisation and characterisation. An aerobic mineralisation procedure, as described by Le Vay [51] in the mineralisation of *E coli.* bacterioferritin, was pursued to mineralise an iron core inside the recombinant particle without particle aggregation. Following this protocol, the *Pf* ferritin was incubated with ammonium iron sulphate and hydrochloric acid at room temperature. As with previous particle characterisations of apoPf and mfPf, Section 2.8.2 and Section 2.8.3, SEC, DLS and TEM were employed to understand how iron oxide loading contributes to particle size, shape and aggregation. In this mineralisation procedure, different mineralisation ratios were calculated from the initial pre-reaction protein concentration of apoPf and assuming an even distribution of iron loading for all ferritin cages. The iron-to-particle ratio determines their nomenclature, e.g. Pf120 is mineralised with 120 iron atoms per *Pf* particle.

Aerobically mineralised apoPf samples were separated from the reaction solution using SEC. Particles where identified using the UV trace chromatogram. Figure 2.14 is an example of the UV chromatogram seen for the apoPf mineralised with an AIS to achieve 600 atoms per ferritin particle (Pf600). The elution profile follows those seen in previous apoPf characterisations and, as a result, the fractions eluting around the peak at 56.41ml were selected for further characterisation using DLS and TEM.

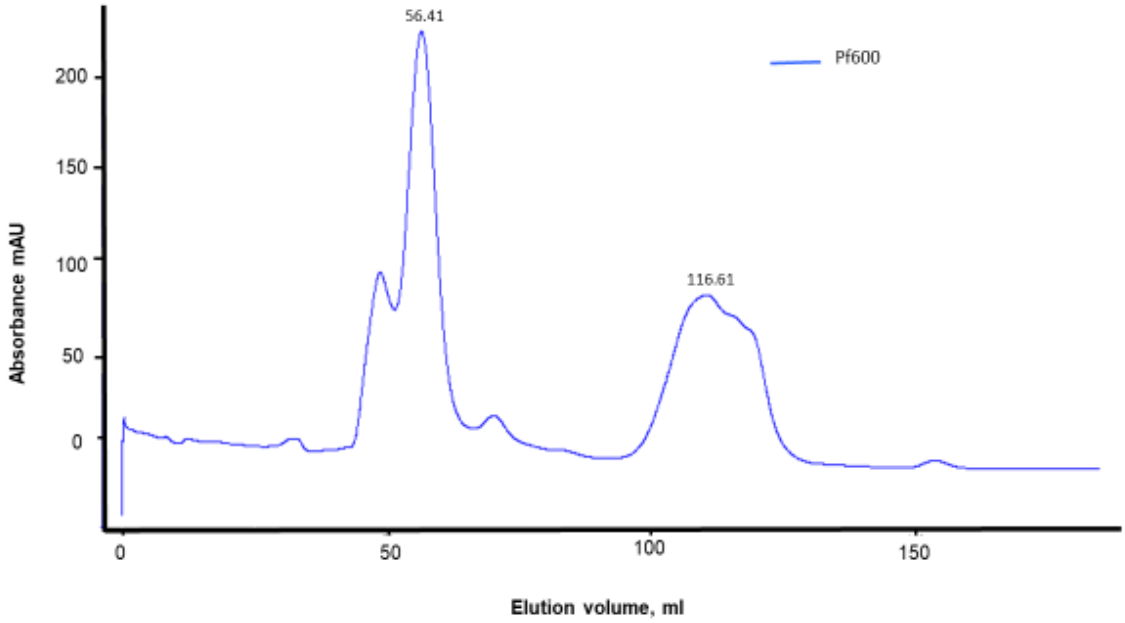

Figure 2.14 UV chromatogram of Pf600 size exclusion

UV chromatogram from S200 size exclusion of Pf600 mineralised ferritin with the fractions eluting at 56.41ml identified as ferritin particles.

DLS was used to determine hydrodynamic diameter and sample dispersity. Shown in Figure 2.15**,** the even distribution peaks for volume and mean particle number indicate a monodisperse hydrodynamic diameter consistent with that expected for ferritin. The hydrodynamic diameter intensity peak has a wider skewed distribution due to larger particles dominating the scattering. However, the correlation coefficient against time displays a sigmoidal decay, representing a homogeneous sample.

The DLS data for the aerobically mineralised ferritin (Pf600) is compared with those for the anaerobically mineralised ferritin (mfPf) in Table 2-3. Here the reported mean hydrodynamic diameter for Pf600 from the peak was 10.64 nm, with a Z-average of 17.64 nm and a polydispersity index reading of 0.18. Compared with a higher Z-average seen in mfPf samples of 62.67 nm and a higher PDI reading of 0.25, this DLS characterisation identified monodisperse particles in the Pf600 solution suitable for further characterisation.

TEM analysis provided evidence of particle homogeneity, identifying distinct circular particles present with darker circular cores, Figure 2.16. Quantitative size analysis of 72 particles identified a mean diameter of 11.37 nm SD 0.79 nm. These measurements supported TEM characterisations of *Pf* ferritin throughout this investigation and identified monodisperse homogenous particles suitable for downstream functionalisation.

Table 2-3 Dynamic light scattering size parameters of mineralised ferritin

Comparison of aerobic loaded ferritin (Pf600) and anaerobically loaded sample (mfPf)

				Volume distribution					
	Number mean d (nm)	Z-average d.nm	PDI	Peak 1 Mean d (nm)	Peak 1 Area %	Peak 2 Mean d (nm)	Peak 2 Area %	Peak 3 Mean d (nm)	Peak 3 Area %
Pf600	10.64	17.64	0.18	19.57	98.00	4510.5	2.00	4418	1.9
mfPf	11.56	62.67	0.25	88.73	96.73	15.25	3.95	0	0

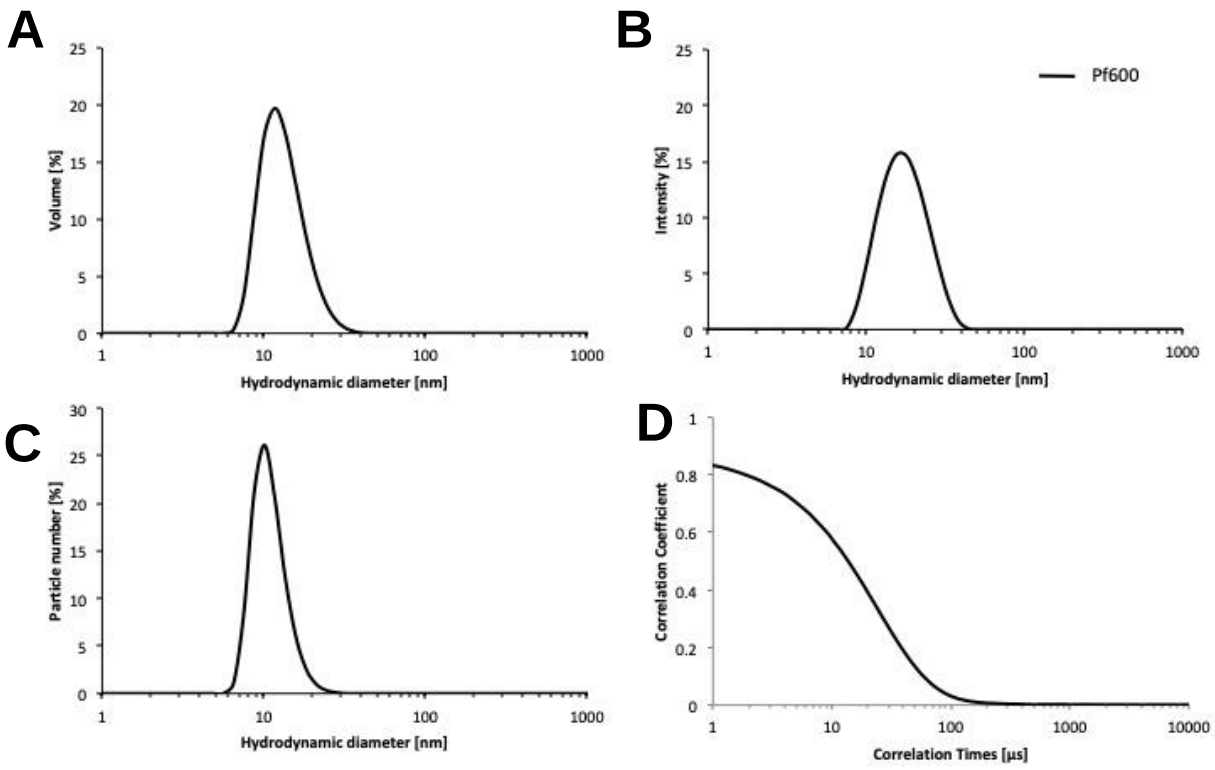

Figure 2.15 Dynamic light scattering size analysis of Pf600

Hydrodynamic diameter measurements of aerobically loaded Pf600 after SEC. Hydrodynamic diameter as volume of sample (A), intensity of signal (B), and mean particle number (C) and correlation coefficient (D)

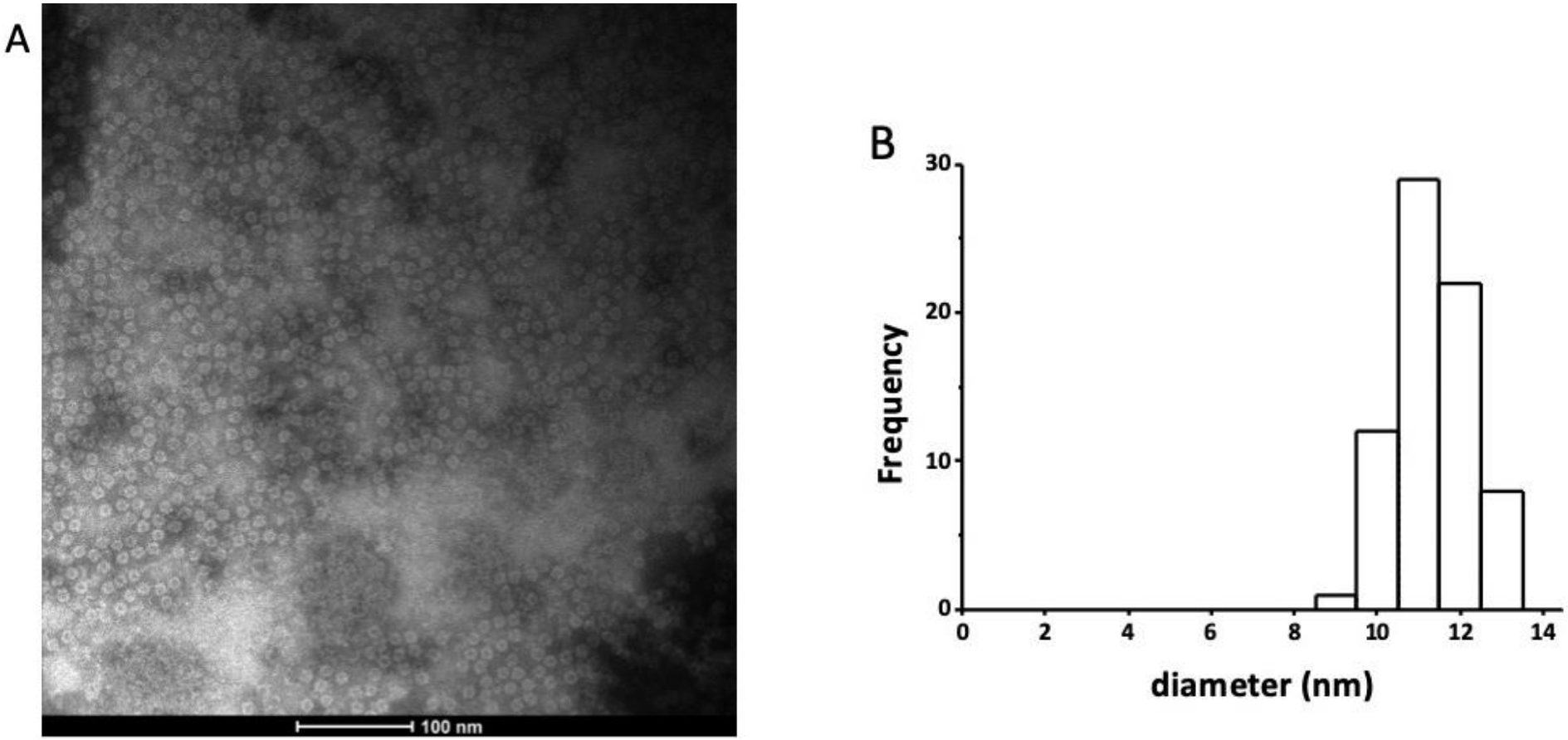

Figure 2.16 Transmission electron microscopy analysis of Pf600

(A) Images of Pf600 ferritin after SEC, stained with 1% PTA, at x49000, (B) Frequency of particle by diameter histogram image analysis indicates a mean diameter of 11.37 nm 0.79 nm

Using this anaerobic protocol different concentrations of AIS were added to the apoPf ferritin to provide evidence supporting the reconstitution of a tuneable iron oxide core within the particle. Five loading concentration ratios were calculated from the initial concentration of apoPf and assuming an even distribution of iron loading for the ferritin cages, with expected magnetic susceptibility increasing as iron concentration increases. As described by Le Vay [51] in the mineralisation of *E coli.* bacterioferritin these aerobically mineralised particles can be further characterised using SAXS. To accurately measure iron concentrations, post mineralisation solutions were purified using SEC and fractions containing digested ferritin particles were analysed using ICP-OES. This allowed the measurement of iron concentration in ppb. Figure 2.17 demonstrates the tuneable loading of different iron concentrations as measured by ICP-OES.

The three characterisation methods of DLS, TEM and SEC provide strong evidence supporting the presence of monodisperse *Pf* ferritin particles. ICP-OES analysis provides evidence of particles with distinct iron mineralisation concentrations. These samples were recovered at an appropriate yield and high monodisperse quality for downstream functionalisation as and advanced characterisation by SAXS. However, magnetometry is required to understand the nanoparticles magnetic susceptibility as a result of the mineralisation described here.

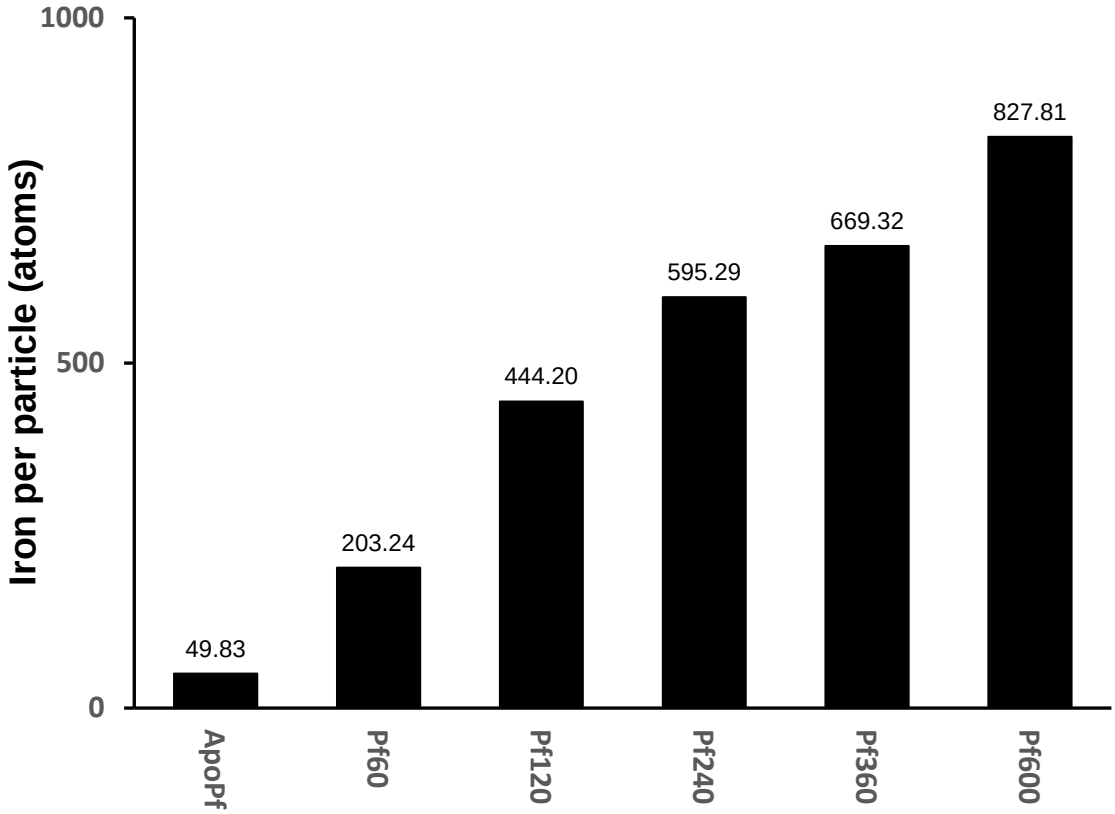

Figure 2.17 Iron atoms per ferritin particle

Iron concentration in atoms per ferritin molecule, iron concentrations measured from ICP-OES analysis. Protein concentration calculated using Bradford assay.

2.9 Comparison of Hsf and *Pf* ferritin

After the successful synthesis of monodisperse mineralised *Pf* ferritin nanoparticles using the aerobic mineralisation protocol, it was decided to adjust the anaerobic iron loading protocol to recreate monodisperse particles for functionalisation. Ferritin particles (apoPf) were incubated at 65^{o}C with hydrogen peroxide, inside an anaerobic chamber thus creating the right conditions for the reconstitution of a magnetite core as described by Okuda et al. [49]. Two different iron loading ratios were compared with a commercially available reference spleen ferritin to better understand the instability of the *Pf* ferritin seen in previous anaerobic reactions. Here, as with the aerobic loading, the iron-to-particle ratio determines the nomenclature, e.g. Pf120 is mineralised with 120 iron atoms per Pf particle. Hsf refers to horse spleen ferritin.

After the mineralisation protocol, ferritin nanocages were purified from the reaction solution using SEC, Figure 2.18**.** This was carried out on an S200 column and the resulting chromatogram indicated significant elution of peaks just before the expected 60 ml, with Pf120 eluting at 59.33 ml, Pf600 eluting at 57.61 ml, Hsf120 eluting at 58,47 ml and Hsf600 eluting at 58.28 ml, as described in previous ferritin size chromatography elution. Three elution profiles displayed uncharacterised peaks at 47 ml, which is too large molecular weight to be considered as monodisperse ferritin. The Hsf600 and Pf120 elution profile displayed a peak around 108 ml, too small to be considered assembled ferritin particles. The fractions from the identified peak from all four loading ratios were collected for downstream characterisation via DLS, TEM, ICP-OES and SAXS. All other fractions were disqualified from further analysis.

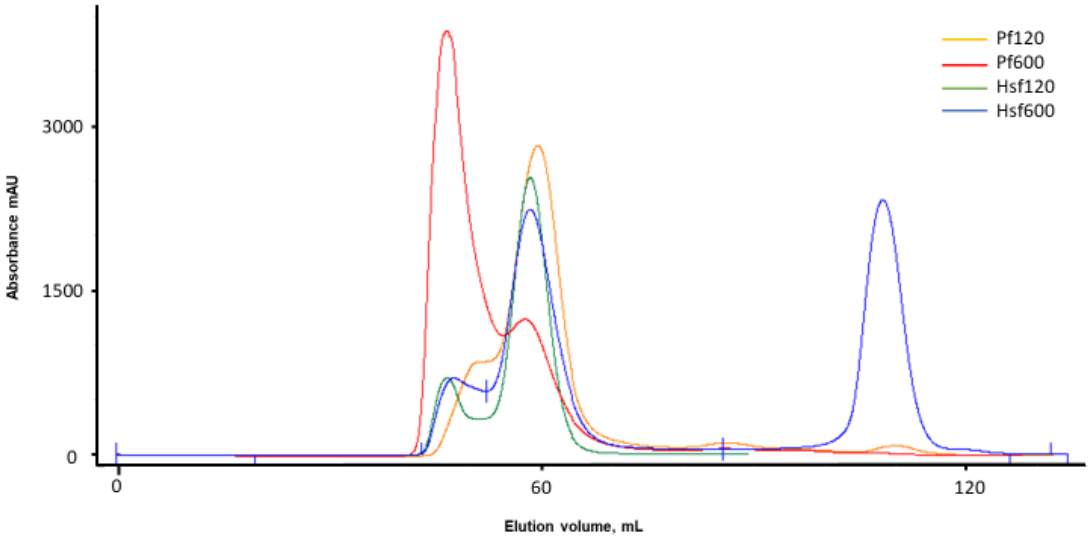

Figure 2.18 UV chromatogram of anaerobically mineralised ferritin

UV chromatogram from S200 size exclusion of mineralised ferritin. Pf120 (yellow) peaks at 51.59 ml and 59.33 ml. Pf600 (red) peaks at 46.44 mL and 57.61 ml. Hsf120 (green) peaks at 47.40 ml and 58.47 ml. Hsf600 (blue) peaks at 47.47 ml, 58.28 ml and 108.12 ml.

DLS analysis of the iron mineralised particles can be been seen in Figure 2.19 and Figure 2.20 for Hsf and *Pf* ferritin respectively. Looking at the three hydrodynamic diameter measurements for Hsf there is an even distribution peak for both particle number and particle volume. There is some uneven distribution on intensity, with higher intensity peaks identifying some polydispersity which is reflected in the size parameters reported by the DLS report in Table 2-4**.** Here, the Z-average has increased as a result of the higher intensity scattering. DLS parameters report a mean dimeter of 12.23 nm for apoHsf and 12.57 nm for Hsf600 as expected for ferritin particles. An increased mean diameter of 15.43 nm as a result of the increased peak volume distribution.

Considering the *Pf* ferritin iron loadings, there was an even peak distribution seen for particle number and volume, with a high degree of homogeneity seen with the hydrodynamic intensity measurements for apoPf and Pf120. This, reflected in a lower Z-average for those loading ratios. The DLS parameters report mean particle diameters of 11.08 nm for apoPf, 11.30 nm for Pf120 and 10.75 nm for Pf600, consistent with previous size analysis from the investigation, providing evidence for reproducibility across mineralisation protocols.

The coefficient correlograms presented as a sigmoidal decay for all samples and the polydispersity index was below 0.4 for all samples. This combined evidence strongly supported particle homogeneity and low polydispersity in solution after anaerobic mineralisation.

Table 2-4 Dynamic light scattering parameters

Comparison of two iron loading ratios, 600 atoms and 120 atoms per ferritin molecule, for Hsf and recombinant Pf ferritin

				Volume Distribution			
	Number mean d (nm)	Z-average d (nm)	PDI	Peak 1 Mean d (nm)	Peak 1 Area %	Peak 2 Mean d (nm)	Peak 2 Area %
apoHsf	12.23	21.23	0.26	20.80	85.6	257.90	14.40
Hsf120	15.43	30.23	0.32	40.33	97.30	3895	2.70
Hsf600	12.57	68.38	0.13	21.41	96.00	239.50	4.00
apoPf	11.08	16.29	0.12	18.40	100.0	0.00	0.00
Pf120	11.30	16.57	0.12	18.63	100.0	0.00	0.00
Pf600	10.75	20.40	0.24	22.45	93.10	2412	6.90

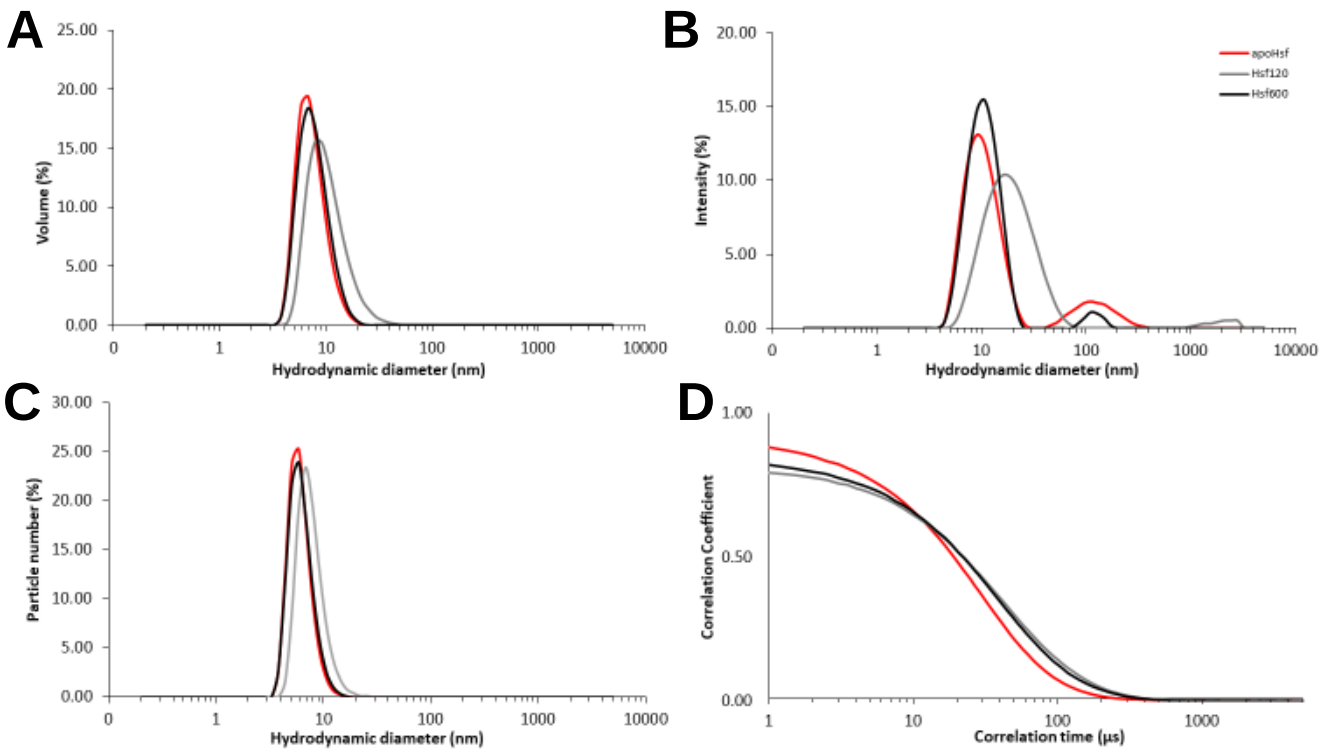

Figure 2.19 Dynamic light scattering size analysis of Hsf ferritin

Hydrodynamic diameter measurements of apoHsf (red), Hsf120 (grey) and Hsf600 (black) after SEC. Hydrodynamic diameter as volume of sample (A), intensity of signal (B), and mean particle number (C) and correlation coefficient (D)

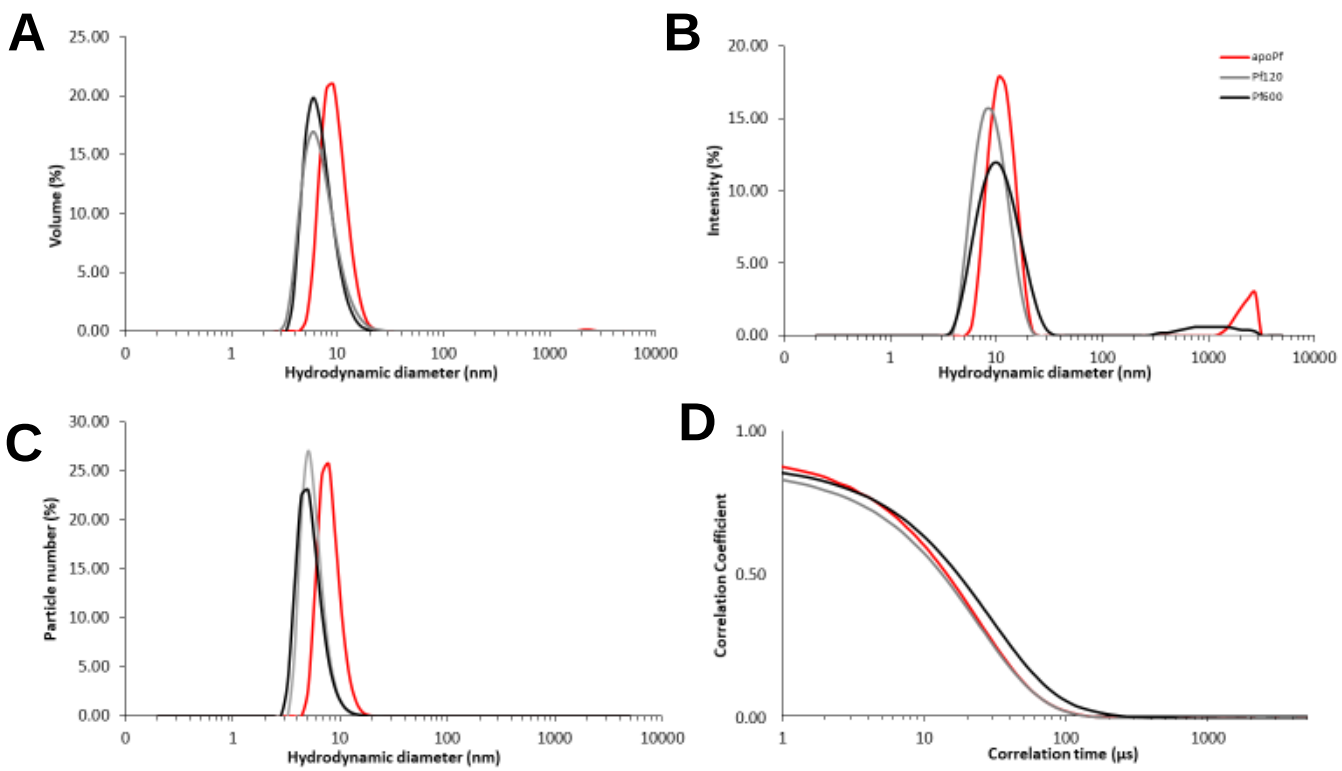

Figure 2.20 Dynamic light scattering size analysis of Pf ferritin

Hydrodynamic diameter measurements of apoPf (red), Pf120 (grey) and Pf600 (black) after SEC. Hydrodynamic diameter as volume of sample (A), intensity of signal (B), and mean particle number (C) and correlation coefficient (D)

To visualise the ferritin structures and characterise the reconstitution of iron cores TEM was used. As seen in Figure 2.21**,** the apoHsf appeared as the characteristic circles seen with the previous apoPf characterisation. Particle size analysis of 137 particles resulted in a mean diameter as 12.07 ± 1.02 nm. There were significant darker cores within each circle, a possible contribution from the electron dense iron core. This evidence was supported by ICP-OES analysis, which suggested that there was significant iron n the apoHsf before the mineralisation reaction.

Two iron loading ratios for Hsf were also analysed by TEM, with Hsf120 and Hsf600 both presenting as discreet circles with darker cores. Particle size analysis of 80 Hsf120 particles resulted in a mean diameter of 13.50 ± 0.69 nm, Figure 2.22. Similarly, quantitative analysis of 50 Hsf600 particles identified a mean diameter of 12.35 ± 0.69 nm, Figure 2.23. These diameters supported the previous size analysis using TEM and are in line with the reported diameters in the literature [33]. The homogeneity of diameter despite mineralisation concentration strongly supports the view that core formation does not significantly affect particle size.

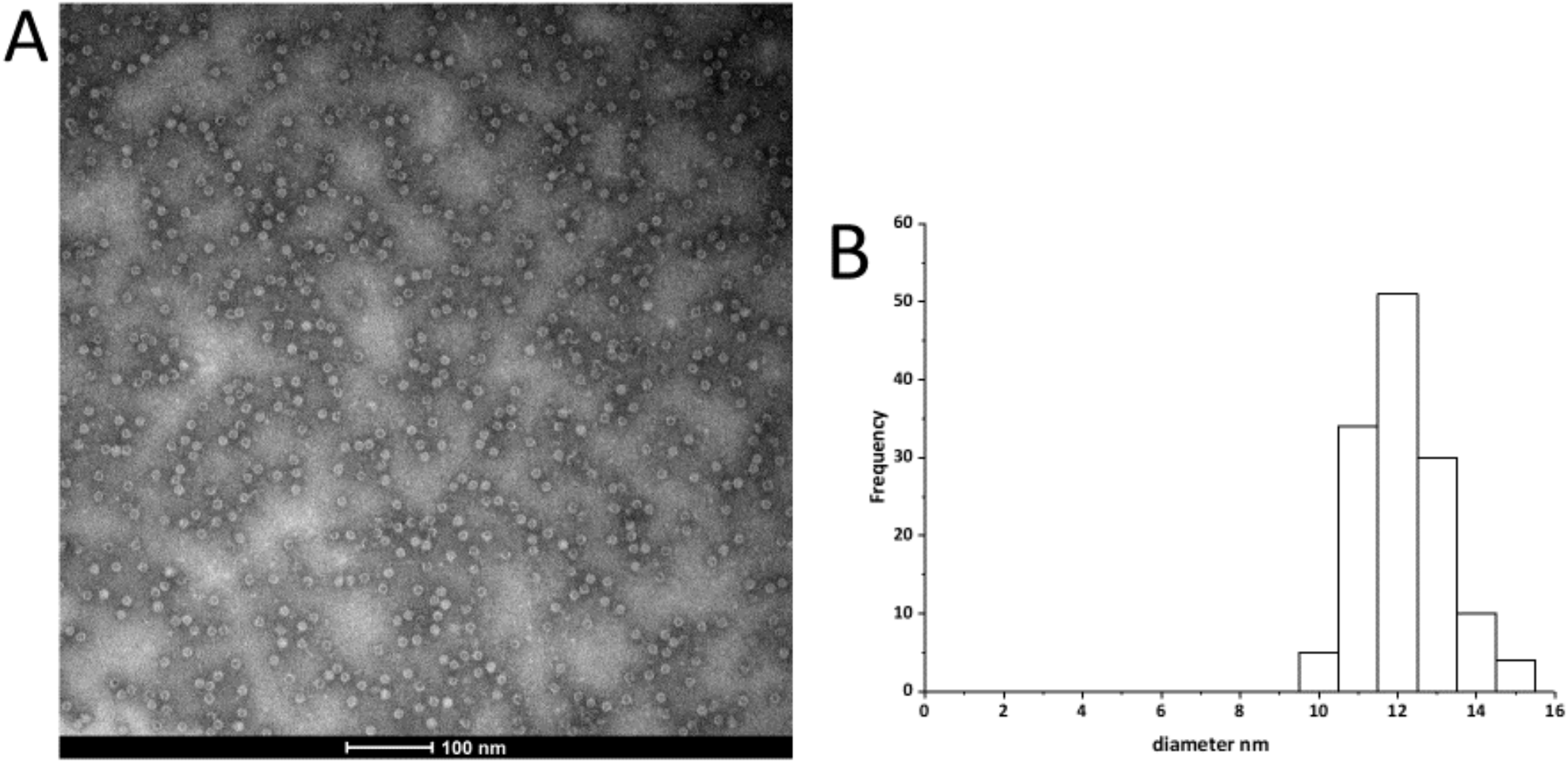

Figure 2.21 Transmission electron microscopy analysis of apoHsf

(A)TEM of pre-mineralisation horse spleen ferritin (apoHsf) solution stained with 1% PTA, at x49000, (B) Particle diameter frequency distribution analysis indicates a mean diameter of 13.14 ± 0.97 nm.

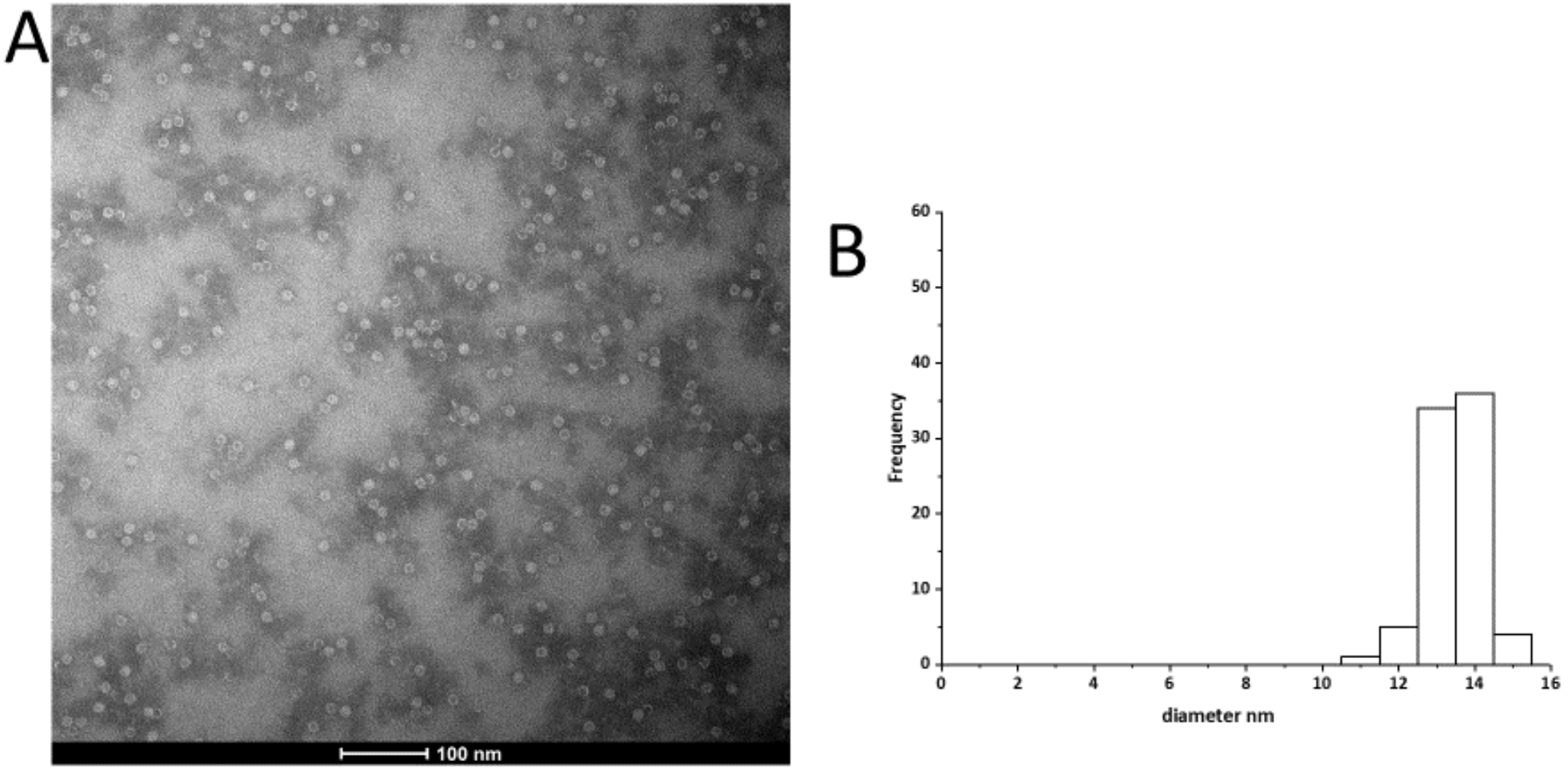

Figure 2.22 Transmission electron microscopy analysis of Hsf120

(A) TEM of mineralised horse spleen ferritin Hsf120 solution stained with 1% PTA, at x49000, (B) Particle diameter frequency distribution analysis indicates a mean diameter of 13.50 ± 0.69 nm.

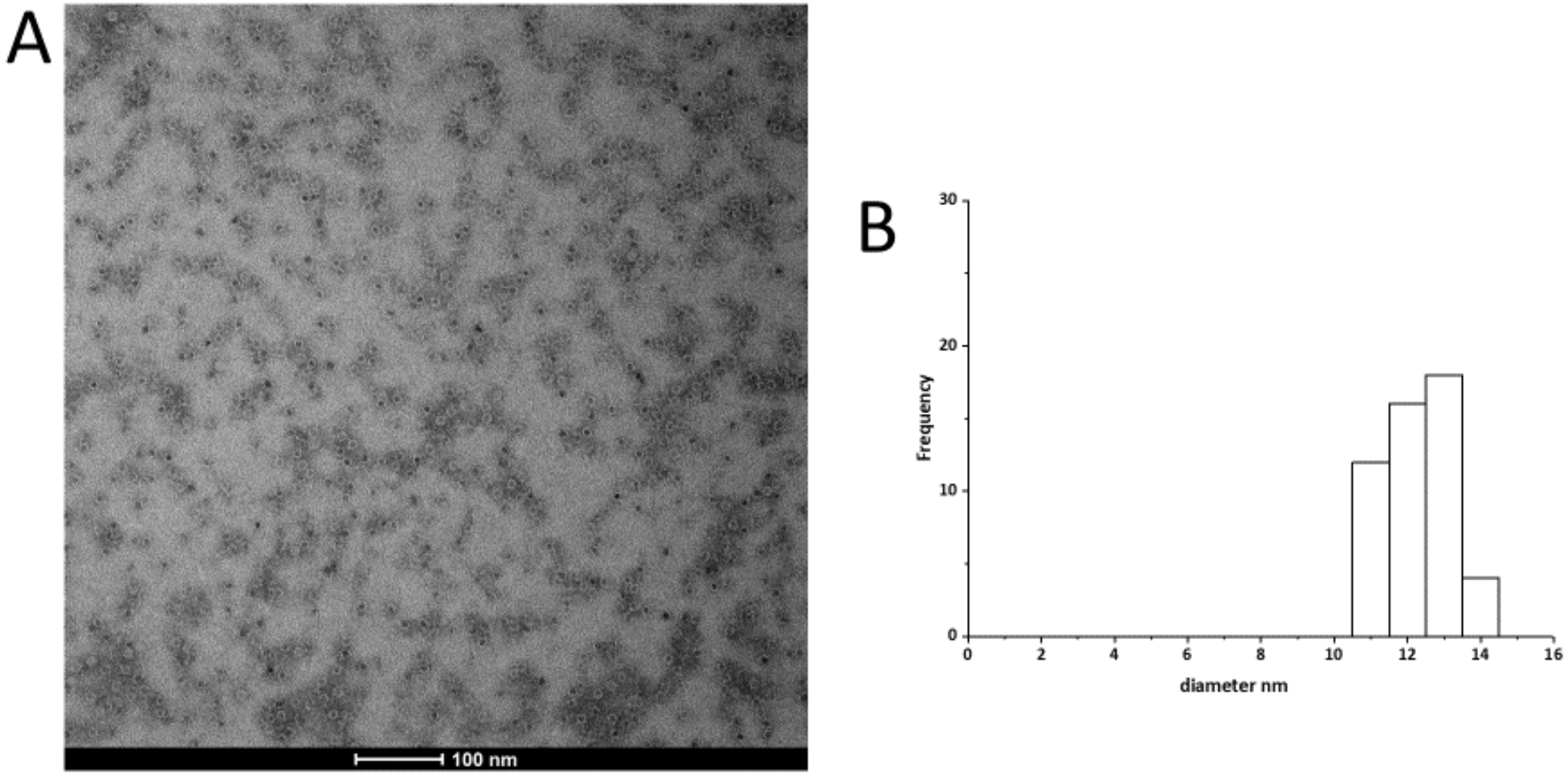

Figure 2.23 Transmission electron microscopy analysis of Hsf600

(A)TEM of mineralised horse spleen ferritin Hsf600 solution stained with 1% PTA, at x49000, (B) Particle diameter frequency distribution analysis indicates a mean diameter of 12.35 ± 0.83 nm.

To compare the recombinant ferritin structure after mineralisation with the findings of mineralised Hsf, and to characterise the reconstitution of iron cores, TEM analysis was carried out on samples of the mineralised recombinant *Pf* ferritin. Seen in Figure 2.24**,** the apoPf appeared as the characteristic circles as reported previously. There was evidence of darker cores within the particles, these appeared around the areas of high concentration of PTA stain. Particle size analysis of 78 particles measured the mean diameter as 13.14 ± 0.97 nm.

Two iron loading ratios for *Pf* were also analysed by TEM, with data for Pf120 and Pf600 shown in Figure 2.25 and Figure 2.26 respectively. These particles also presenting as discreet circles with darker cores. Particle size analysis of 57 Pf120 particles resulted in a mean diameter of 13.05 ± 0.97nm, Figure 2.25. Similarly, particle analysis of 86 Pf600 particles resulted in a mean diameter of 12.80 ± 0.87 nm, Figure 2.26**.**

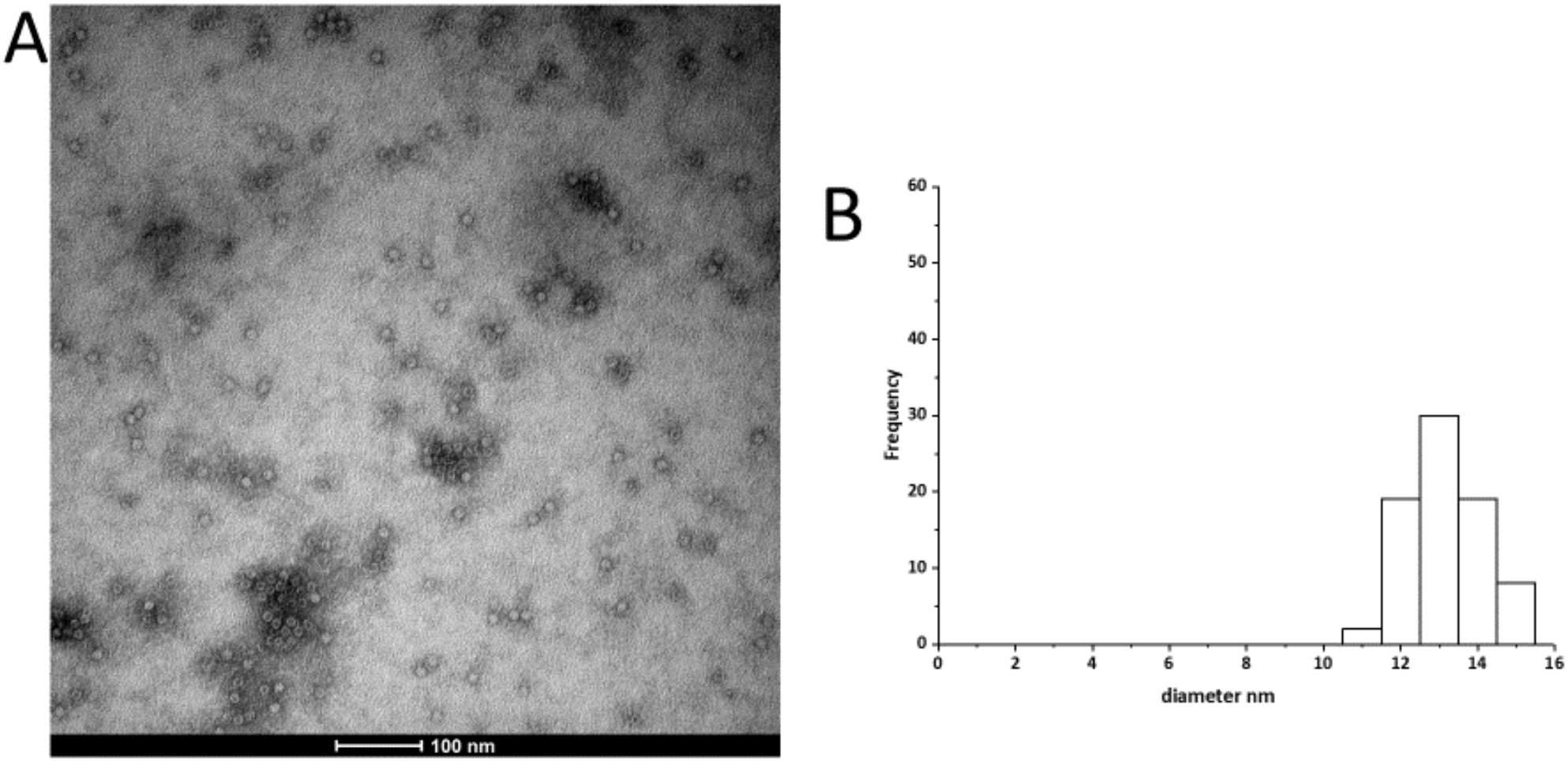

Figure 2.24 Transmission electron microscopy analysis of apoPf

(A)TEM of pre mineralisation apoPf solution stained with 1% PTA, at x49000, (B) Particle diameter frequency distribution analysis indicates a mean diameter of 13.14 ± 0.97 nm.

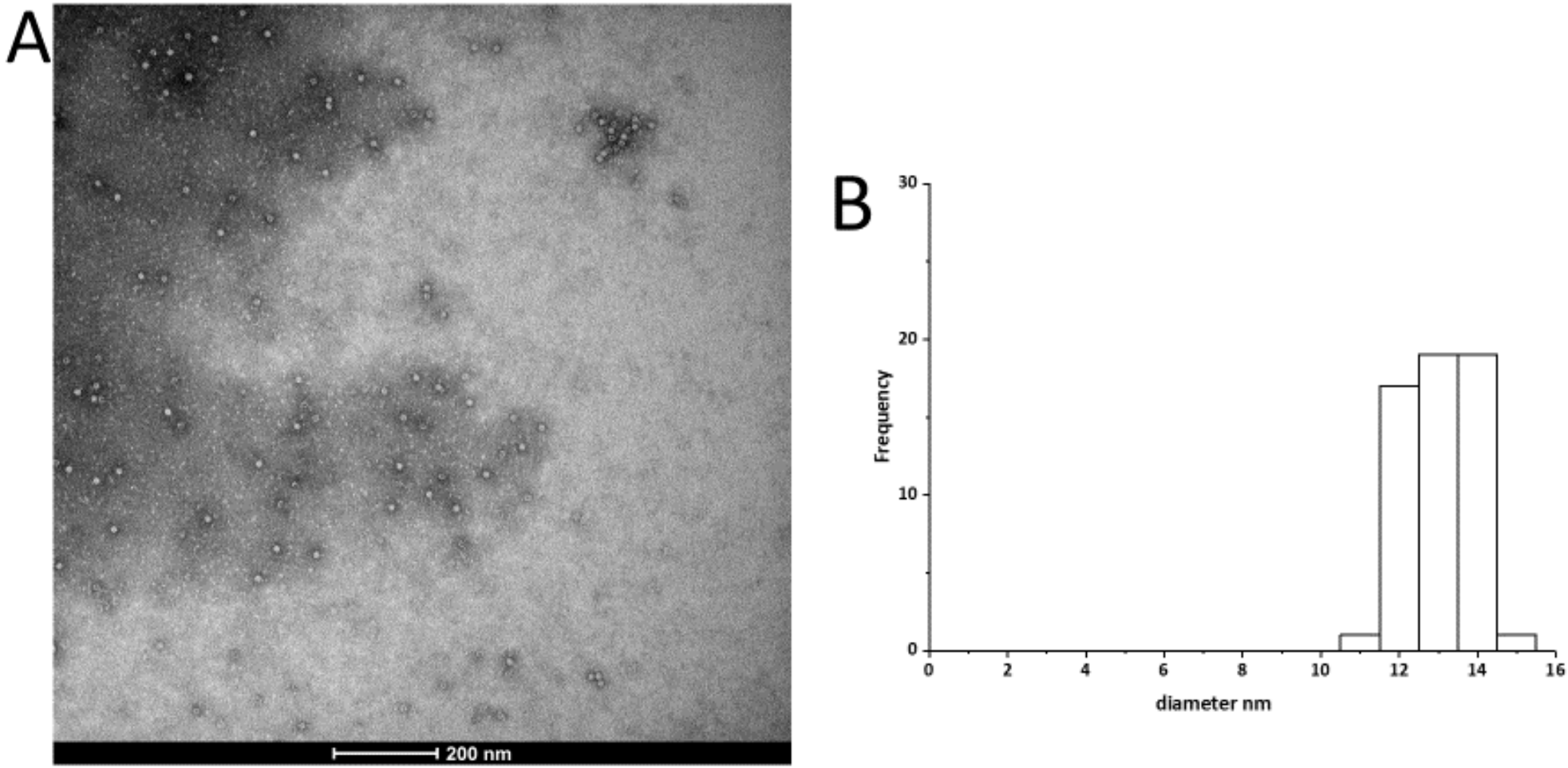

Figure 2.25 Transmission electron microscopy analysis of Pf120

(A)TEM of mineralised Pf ferritin Pf120 solution stained with 1% PTA, at x30000, (B) Particle diameter frequency distribution analysis indicates a mean diameter of 13.05 ± 0.97 nm

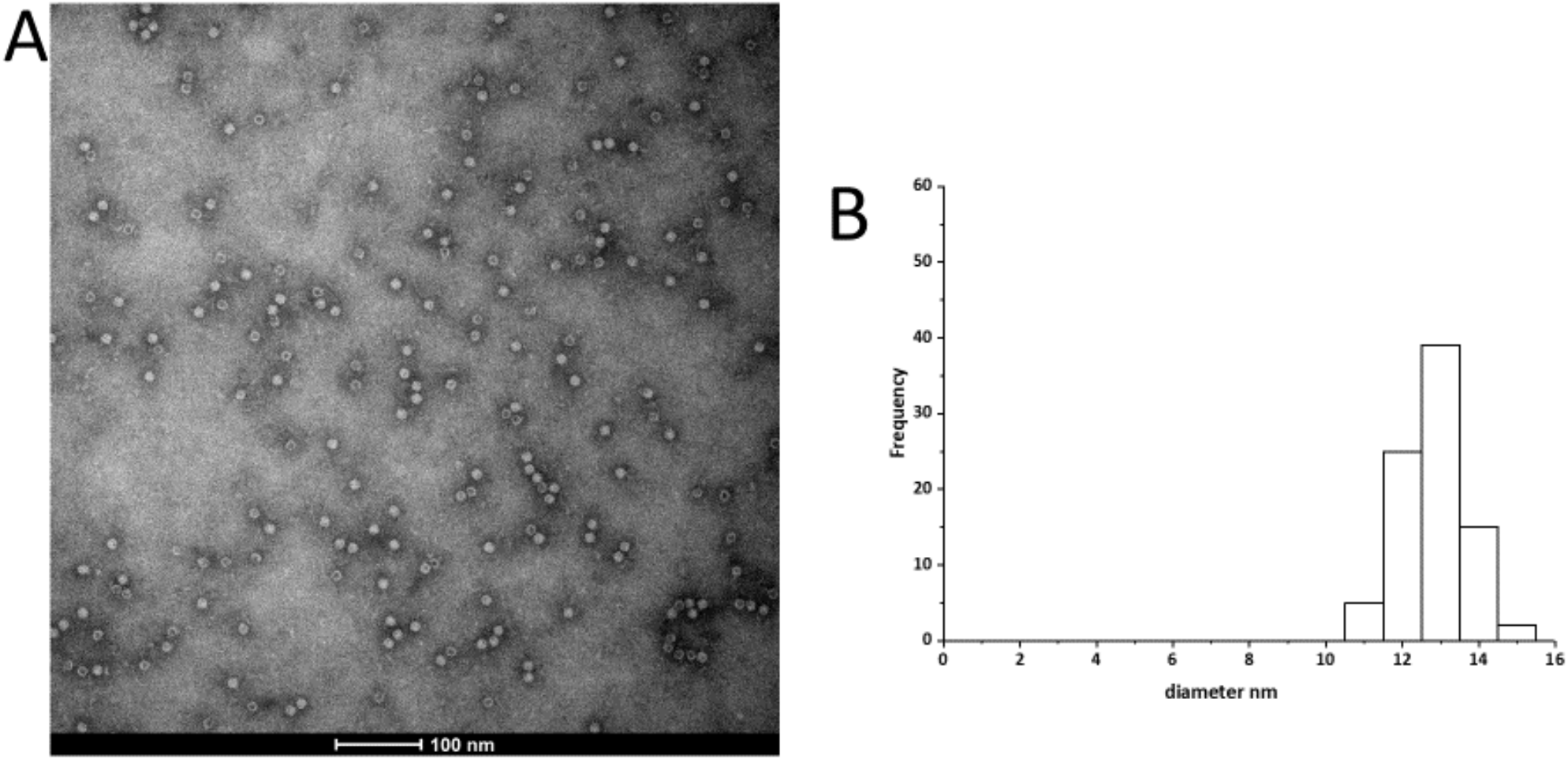

Figure 2.26 Transmission electron microscopy analysis of Pf600

(A)TEM of mineralised Pf ferritin Pf120solution stained with 1% PTA, at x490000, (B) Particle diameter frequency distribution analysis indicates a mean diameter of 12.80 ± 0.8 nm.

The purified fractions identified as ferritin nanocages by TEM and DLS were taken for ICP-OES analysis in order to characterise iron mineralisation. As seen with the aerobic iron loading, increases in iron concentration of the reaction increased the loading factor per ferritin particle thus demonstrating the tuneable loading of both types of ferritin, Figure 2.27. However, from the ICP-OES it is evident that the commercially available apoHsf started with a much higher pre-reaction iron concentration at 552.73 iron atoms per nanocage whereas the apoPf ferritin contained 38.88 atoms per cage. This iron concentration of apoPf was similar to concentrations reported in Section 2.8.2 where the presence of 49.83 iron atoms was measured and Section 2.8.4 where the presence of 47.76 atoms per cage was measured.

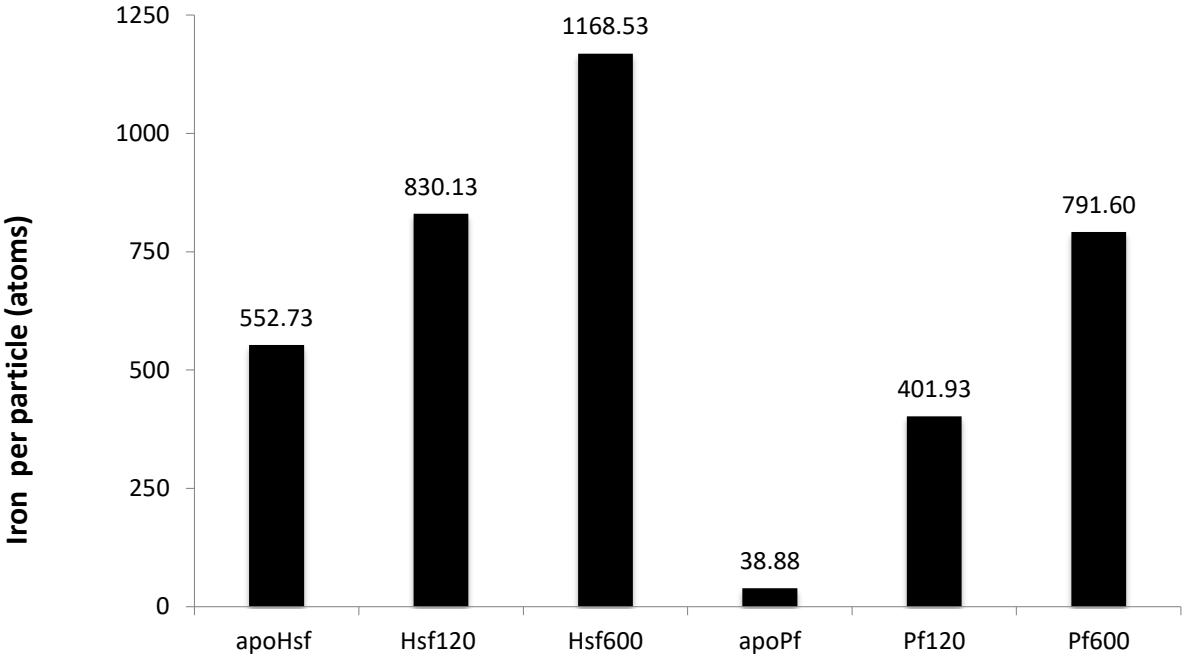

Figure 2.27 Iron atoms per ferritin particle

Iron concentration in iron atoms per ferritin molecule, iron concentrations measured from ICP-OES analysis. Protein concentration calculated using Bradford assay.

2.10 Discussion

Recombinant apoPf ferritin was successfully characterised by three separate techniques. DLS and SEC provided quantitative evidence of particle polydispersity and size, helping to identify the desired protein from aggregates, evident when compared with a horse spleen ferritin standard. This was supported by TEM, which allowed qualitative and quantitative analysis supporting the particle characterisation.

DLS was the preferred method to analyse the nanoparticle polydispersity in buffer solution. There are three factors to consider when interpreting DLS data. Firstly, the Z-average is the mean hydrodynamic diameter derived from the cumulate particle correlation analysis. It is an intensity weighted mean, and therefore increases as particle size increases [64]. If the sample is monodisperse, the Z-average should be equal to the mean diameter. However, the Z-average is harder to interpret with more polydisperse samples due to higher intensity particulates dominating the measurement. With polydisperse samples the Z-average is different to that of mean size diameter.

Secondly, the polydispersity index (PDI) is calculated from a two-parameter fit and indicates the width of the overall distribution. The broad size distribution seen in an aggregated polydisperse sample would result in a PDI greater than 0.7 [65].

Thirdly, the size distribution reports a mean size and distribution for separate peaks in the sample. Distribution analysis can be broken down for the separate peaks or a fitting algorithm used by the Zetasizer to calculate a mean size hydrodynamic diameter. When interpreting the DLS data, a lower PDI coupled with similar Z-average and mean hydrodynamic size distribution is strong evidence for a highly monodisperse sample. The Zetasizer was designed for the analysis of synthetic particles, and some interpretation of the three factors mentioned should be considered for organic protein particles. DLS should be used alongside other characterisation techniques, such as TEM or SAXS.

When mineralised aerobically, ferritin particles retain the monodispersity seen for purified apoPf fractions, with DLS data indicating a low PDI and a similar Z-average

and mean distribution with this analysis supported by the presence of homogenous particles in the TEM images.

However, the increased Z-average and wide size distribution DLS measurements seen in the anaerobically mineralised mfPf samples indicate particle aggregation and microscopy images supported this evaluation through qualitative evidence of particle aggregation. The TEM images of the anaerobically mineralised samples show clear ferritin structures inside large aggregate masses. This difference between the two sample homogeneities suggests that the reaction conditions of anaerobic mineralisation are causing the protein to aggregate.

Previous anaerobic mineralisation of horse spleen ferritin, using a double jacketed vessel, yielded appropriate mineralised nanoparticles for downstream cationisation as described by Carreira et al. [66]. When this protocol was employed for *Pf* ferritin, the result was an aggregation of protein inappropriate for downstream application. Perhaps the double subunit L-chain and H-chain structure of horse spleen ferritin is contributing to the particle's stability during the mineralisation process.

The improved monodispersity of sample, seen in the aerobic mineralisation, inspired the change in protocol to a new anaerobic mineralisation technique. Instead of using a double jacketed vessel and a magnetic stirring flea, the reactions were kept at a constant temperature of 65^{o}C in a heat block with an automatic stirrer operating at 300 rpm. To reduce any oxygen entering the reaction the mineralisation was performed in an anaerobic chamber. As a result of these controls the anaerobically mineralised ferritin was tuneable and increased the yield of monodisperse particles after SEC. This was evident through the lower PDI numbers, lower Z-averages and mean hydrodynamic size distributions These particles were identified as suitable for downstream functionalisation, and further characterisation using SAXS.

Comparison between the anaerobically mineralised Hsf and *Pf* ferritin using the changed protocol, produced strong evidence for low particle polydispersity post-reaction. However, there was heterogeneity in the iron core appearance as seen via TEM, with some particles displaying iron core formation and others not. These should

be further segregated through a magnetic separation column as described by Okuda et al. [49] to produce a homogenous nanoparticle with magnetic susceptibility.

The degree of particle mineralisation was measured by ICP-OES. This methodology was chosen over colourimetric testing as it reduced pipetting error and could differentiate iron concentrations down to parts per billion. It was important to get an accurate protein concentration measurement in order to characterise the iron loading ratio accurately. This ICP-OES analysis at face value suggests that the mineralisation of ferritin can be tuneable, with distinction between each iron loading ratio. However, the TEM images indicate some particles with iron cores and others without. This implies that there may not be even distribution of iron across the nanoparticles. It is unclear if this is just an artefact of the TEM, as snapshot in time, or a genuine characterisation of an uneven distribution of iron cores throughout the samples. None the less, magnetic separation would allow further particle purification and establish a truly homogenous sample.

Alongside the DLS measurements, TEM images of the mineralised nanocages for both Hsf and *Pf* ferritin provided quantitative evidence of particles shape and structure. Particle size analysis using ImageJ provided confirmatory particle diameter measurements and this correlation allowed for confidence in these samples being appropriate for SAXS analysis. These initial size measurements are valuable for the interpretation of SAXS data and for the model fitting in Chapter 3. Further analysis of magnetic susceptibility using super conducting magnetometry and particle cationisation is explored in Chapter 4.

Chapter 3 Characterisation of mineralisation using small angle X-ray scattering

With an assembled ferritin particle spanning 12 nm in diameter, one is dependent on advanced characterisation techniques that do not utilise visible light to measure size, shape and structure. This project uses two techniques, transmission electron microscopy (TEM) and small angle X-ray scattering (SAXS), in order to make the invisible, visible. Scattering is a common tool used to support TEM characterisation, where a lot of structural information is lost as the proteins are fixed in a cross section two-dimensional point in time [67].

This chapter focuses on the shape and structural characterisation of recombinant *Pf* ferritin and Hsf and the differences in scattering associated with the loading of variable iron concentrations as previously described in the SAXS analysis of recombinant E coli. bacterioferritin by Le Vay [51]. Similar size and structural analysis of Hsf ferritin has been reported by Okuda et al. [49].

Using the high flux X-ray beamline 21 at Diamond Light Source, the SAXS experimentation provided three-dimensional data for particle shape and structure. This information supports the generation of ab initio dummy atom envelope models built using a Monte Carlo based simulated annealing method.

With a contrast in scattering length densities between the organic protein and iron core, it is expected that SAXS will provide information about how the iron core reconstitutes within the nanoparticle, and how this promotes magnetic susceptibility and particle stability. Form factor modelling will allow the deduction of three-dimensional shape and structure when compared to mathematically calculated models.

3.1 Small angle X-ray scattering

Electromagnetic waves, with a wavelength of 10 – 0.01 nm, are used to characterise size and structure of biological molecules such as proteins and nucleic acids through techniques such as X-ray diffraction and X-ray scattering. Matter exponentially absorbs X-rays, however it is the elastic scattering of X-ray from electron densities at particle-matrix interfaces that can be measured to deduce particle dimensions [68]. X-ray diffraction or crystallography provides a high resolution of atomic structure from a crystallised sample, using the wide-angle X-ray scattering sample-detector dimensions [69]. However, some matter such as lipids or gels may not crystallise. In this case lower resolution SAXS sample-detector dimensions are used to define the macro molecular parameters rather than atomic structure. A benefit of not requiring a crystal is that this technique can provide alternative dynamic experimental analysis, for example, how a protein structure changes in response to pressure or temperature. The crystal structure of *Pf* ferritin has previously been solved [41] and this chapter will focus on the utilisation of SAXS to characterise ferritin shape and structure.

SAXS is a contrast method reliant on the difference between the electron density of particles in solution and the solvent itself, and for that reason pure solvent scattering measurements are required in order to subtract from the sample as explained by Equation 3-1 where $\Delta p(r)$ is the difference in average electron density, $p(r)$ is solute molecule electron density and $p(s)$ is bulk solvent electron density [70].

$$\Delta p(r) = p(r) - p(s)$$

Equation 3-1

Scattering requires a beam of collimated monochromatic X-ray light, of known wavelength, to pass through a sample. A Fourier transform of the electron density is detected from the scattering of the X-rays. In soft systems with order, all possible orientations are measured due to the random arrangement of particles in solution. As a result, we observe the formation of smears and rings, an isotopic equivalent to the Bragg spots seen in crystallography [71]. The intensity and proportion of rings gives information on structure and shape and these data are described one-dimensionally by scatter radiation intensity (I) in terms of scattering vector (q) described in Bragg's law, Equation 3-2,where 2θ is the scattering angle and λ is the incident X-ray beam wavelength. As illustrated in Figure 3.1, SAXS data are presented in the form of a reciprocal scattering curve with intensity of scattering signal (I) measured against scattering angle (q). From the resulting graph, the data at lower q values allow determination of particle size and shape, whereas the data at higher q values apply to internal atomic interactions.

$$q = (4\pi \sin \theta) / \lambda$$

Equation 3-2

Because it is the electron densities of atoms that scatter the X-ray light, scattering power scales with the electron density of the sample. With organic matter, the sample is made from elements with small electron densities. The electron number of solute proteins is very similar to that of the solution they are in, therefore making the contrast characterisation difficult. Higher electron densities contribute to a higher $p(r)$ and provide increased contrast from solution. Scattering length densities (SLD) have been calculated for each atom and lower electron densities are associated with organic atoms that scatter ~1 in 10^4 X-rays. Because of this, a synchrotron is used to generate an increase in photon flux. Synchrotrons can bombard a sample with a flux of ~3 billion photons per second [72], in doing so, increasing the chance of the lower electron densities scattering and therefore resulting in a more powerful characterisation.

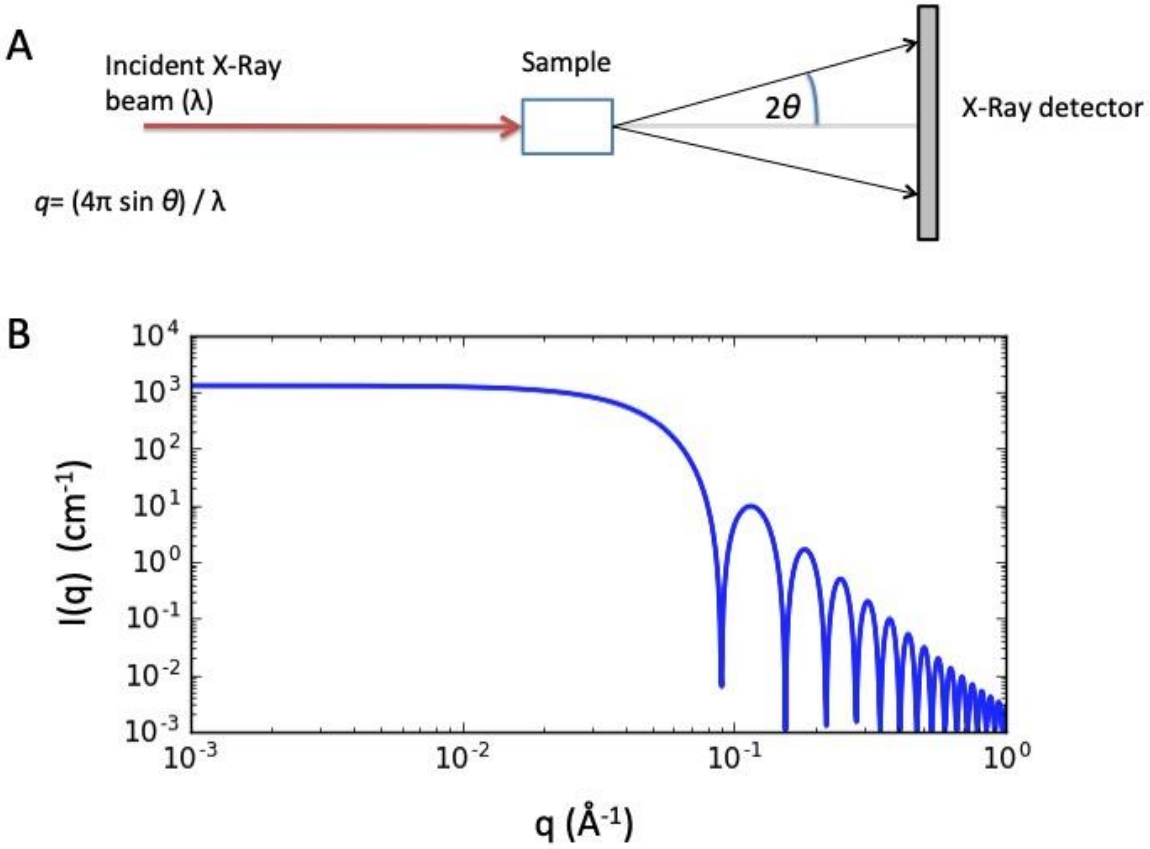

Figure 3.1 Schematic of classic setup for a static SAXS beam line

(A) Schematic of typical static SAXS measurement (B) a 1D plot of a model sphere particle with uniform scattering length density. I(q) scattering intensity is plotted against q scattering vector.

3.2 Scattering analysis and The Magic Square

It is the scattering intensity of electron density that when analysed through theoretical calculation, Fourier transform, and model fitting provides structural resolution of nanostructures between 3 nm and 50 nm. The relationship between real space electron density and reciprocal scattering perception can be described using the "Magic Square" [69] seen in Figure 3.2.

The left-hand side of the square relates to real space electron densities, conversely the right-hand side of the square describes the reciprocal space scattering. As seen in the top half of the square, the reciprocal space amplitude *A*(s) of scattering is a Fourier transform of the real space electron density *ρ*(r). Down the right-hand side of the square, intensity *I*(s) is calculated as the square of absolute value of *A*(s). The inverse Fourier transform can be applied to scattering intensity to result in the pair distribution function *P*(r). This transforms the scattering intensity into real space, which is closer to human perception, the P(r) can be used as a platform for *ab initio* bead modelling. Simply, the P(r) is SAXS equivalent of the Patterson function [73] and is described as the autocorrelation operation ⋆**2** of *ρ*(r) [69].

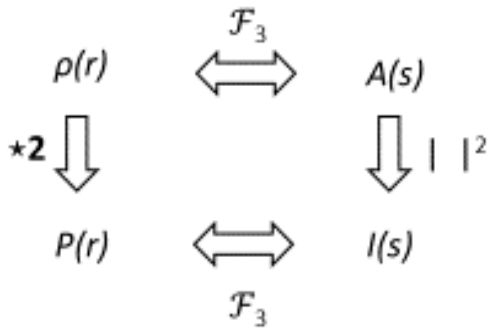

Figure 3.2 The Magic Square

Used to describe the relationship between real space electron density and reciprocal scattering perception. P(r) is the real space electron density, A(s) is the amplitude of scattered photons, I(s) is the intensity of scattered photons, P(r) is the pair wise distribution. *2 SAXS correlation function, I I^2 is the absolute square, f_3 is the Fourier transform. Power Adapted from Stribeck 2007. All rights reserved Springer

3.3 Theoretical analysis of SAXS data

The Guinier approximation is used to theoretically determine particle dispersity and estimate particle size parameters without using a model [68]. Low q values are known as the Guinier region. Guinier analysis can be used to determine the zero-angle scattering intensity I(0) and radius of gyration (Rg). These parameters are deduced from the y intercept and the slope of Guinier plots when low q data are plotted as ln(I(*q*)) against q^2, which for monodisperse particles is linear, whereas particle interactions influence intensity resulting in a curvature along the regression, Figure 3.3**.**

$$I(q) = I_0 e^{-q^2 R_g^2/3}$$

$$\ln I(q) = \ln I_0 - \frac{R_g^2}{3} q^2$$

$$y = b + m * x$$

Equation 3-3

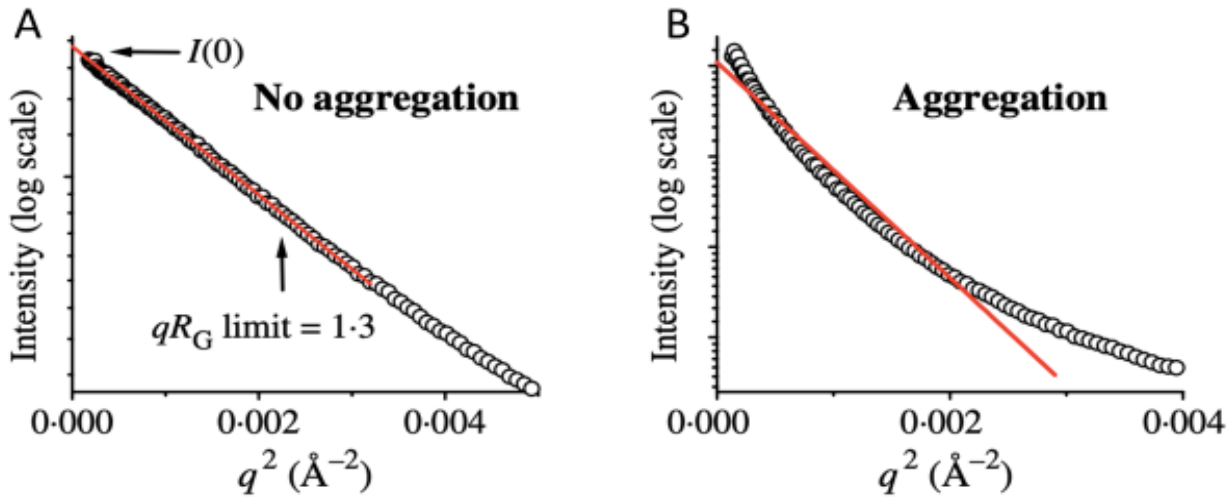

Figure 3.3 Using the Guinier approximation

The Guinier approximation is used to infer particle dispersity and calculate particle size parameters. The inverse of Guinier approximation results in a regression and the slope-intercept can be used to calculate I(0) and Rg.
(A) Data from monodisperse samples with no or little aggregation will be well fitted by the line (B) Data from aggregating samples produce a curve when transformed. Figure adapted with permissions from C. Putnam *et al* [57].

The value of q for the minimum data point must be less than the longest dimension of the particle. Similarly, the value of q for the maximum data point must be less than 1.3 divided by Rg. This is true for globular proteins, such as ferritin. However, different rules apply to rod-like particles and polymers. The more data points within the Guinier region provides increased accuracy when calculating Rg [68].

Zero length scattering, , the intensity measured at zero angle, can provide information on a particle's size unaffected by shape, through its dependence on molecular weight (MW), particle concentration (C), scattering length density (ρ) and partial specific volume of particle (v), shown in Equation 3-4**.** N is the number concentration of scattering objects, V is the volume of a single particle , the intensity measured at zero angle and N_A is Avogadro's number[68].

$$I(0) = NV^2\,\Delta\rho^2 = \frac{C^2\rho^2v^2MW}{\mathrm{NA}}$$

Equation 3-4

The radius of gyration (Rg) is another measurement of overall particle size that is obtained through Guinier analysis. Rg is described as the average root-mean-square of distances from all scattering points to the center of density in the molecule. Due to the spherical nature of ferritin, this is an accurate measurement of shape and size, explained in Equation 3-53 [68]**.**

3.3.1 Kratky analysis

A Kratky plot represents scattering intensity profile as $q^2 \times I(q)$ vs q. The shape of the resulting plot provides evidence for proteins folding and flexibility [74]. As seen in Figure 3.4, globular proteins present as a distinct peak which converges towards the x axis at higher q regions. Proteins with multiple domains and flexible proteins present as different shaped curves or shoulders whereas unfolded proteins present as curves with no peak distribution and plateau at high q regions.

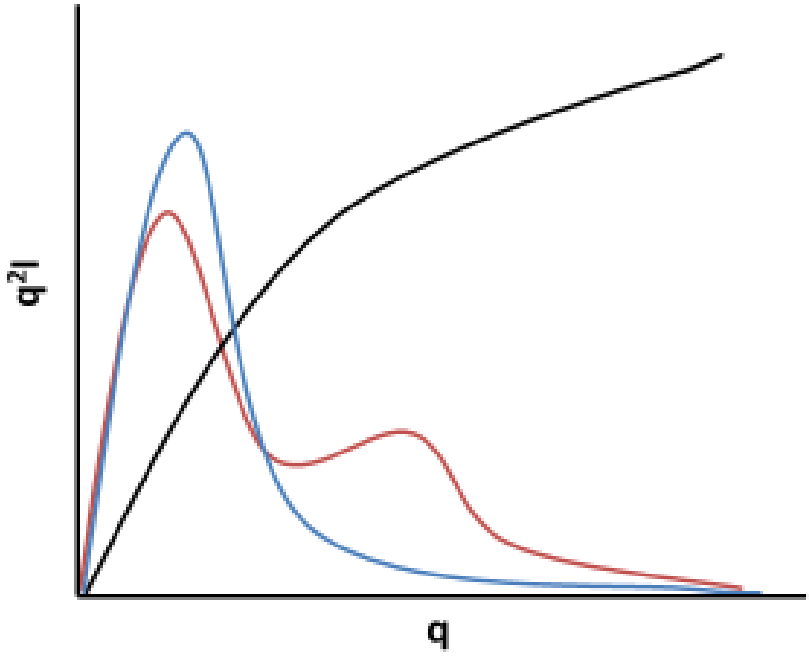

Figure 3.4 Examples of Kratky profiles

Schematic representation of typical Kratky plots with characteristic curves seen for globular protein (blue), unfolded protein (black). With multidomain (red) dependent on molecular size, shape and degree of flexibility.

3.4 Fourier transform analysis of SAXS data

As seen at the bottom right-hand corner of the magic square, the pair distance distribution is the real space indirect Fourier transform of the scattering angle intensity profile. P(r) is presented as a distribution histogram**,** describing the pair wise distribution of inter-atomic distances [73]. P(r) distributions give information on the maximum dimension of the particle (Dmax) and provide information on shape and structure with characteristic distribution curves for discreet particle shapes. Equally the data from P(r) distribution can be used to calculate the I(0) and Rg of a given particle.

The P(r) can also be used to deduce quality of sample, for example a globular monodisperse particle has a P(r) zero at r=0 and at $r \geq D$max. Whereas, aggregated particles will have a value r>0 at Dmax. The benefits of using the P(r) distribution to calculate size and shape rather than the Guinier approximation, is that the P(r) function uses more of the collected data rather than just the low q data from the Guinier region.

3.5 Modelling of SAXS data

3.5.1 Envelope modelling

Monte-Carlo based annealing is the gold standard envelope reconstruction method in SAXS analysis and provides qualitative information on particle shape and structure as a three-dimensional model based on the experimental scattering data [75]. The P(r) is used as a foundation for the generation of low-resolution bead models. From the P(r) fitting, a search volume with a diameter defined from Dmax is filled with dummy atoms which represent either particle (index=1) or solvent (index=0). Using an simulated annealing algorithm, dummy atoms are accepted or rejected on penalties as implemented by the software; the result is a compact interconnected dummy atom model (DAM) whose computed scattering curve optimally fits the experimental scattering curve [75].

3.5.2 Form factor fitting

Form factor fitting describes the three-dimensional structural characteristics such as shape and size from a one-dimensional scattering pattern. Form factor P(Q) refers to the size and shape parameters of an individual particle. Structure factor S(Q), provides information on the spatial arrangements and interactions of particles [76]. The fitting software uses a reduced chi-squared analysis to compare the model scattering curve optimally with the experimental scattering data.

3.6 Methods and materials

Using the aerobic iron loading protocol in Section 2.8.4 and the anaerobic protocol, Section 2.9. *Pf* ferritin and commercially available Hsf were mineralised with concentrations of iron. These samples were characterised as monodisperse for SAXS analysis.

SAXS measurements were performed at the B21 Beamline, Diamond Light Source (Harwell UK). Data were collected with an Eiger x 4M detector at a camera length of 3.9 m and measurements taken with a beam energy of 12.4 keV. The beam cross section was 1 x 5 mm and the X-ray wavelength 1.0 Å. Scattering data were collected in 600 successive frames, with 3 seconds per frame. 2D SAXS patterns were radially averaged from the beam centre, normalised to an absolute intensity using a glassy carbon standard before manual background subtraction. The scattering angle and absolute intensity were pre-calibrated using silver behenate and glassy carbon standards. As seen in the workflow diagram in Figure 3.5, in-line high performance liquid chromatography (HPLC) was employed to purify samples prior to measurement. Utilising the Agilent 1200 HPLC system, and a 2.5 ml Superose 6 column, samples were purified using HEPES 0.05 M, 0.1 M NaCl buffer pH 8.6. as the aqueous phase buffer and delivered to a glass capillary for measurement at a flow rate of 0.075 $ml.min^{-1}$.

As seen in the work flow diagram, Figure 3.5, SAXS data analysis software ScÅtter [70] was used to subtract the signal from the buffer and determine sample characteristics. Kratky plots were normalised by mass and concentration by ScÅtter software. Monte Carlo *ab initio* bead modelling was performed using the modelling software DAMMIN/F [75], part of the ATSAS suite from European Molecular Biology Laboratory [77]. Form Factor fitting was carried out with Sasview 5.0 [78]. Sasview allows the addition of a polydispersity ratio (PDR) to individual parameters, this is related to a mean value of the size distribution of a given parameter. PDR is applied in line with the workflow diagram in Figure 3.5 with a Schulz PDR [79] chosen for its accuracy in describing particle sizes [80].

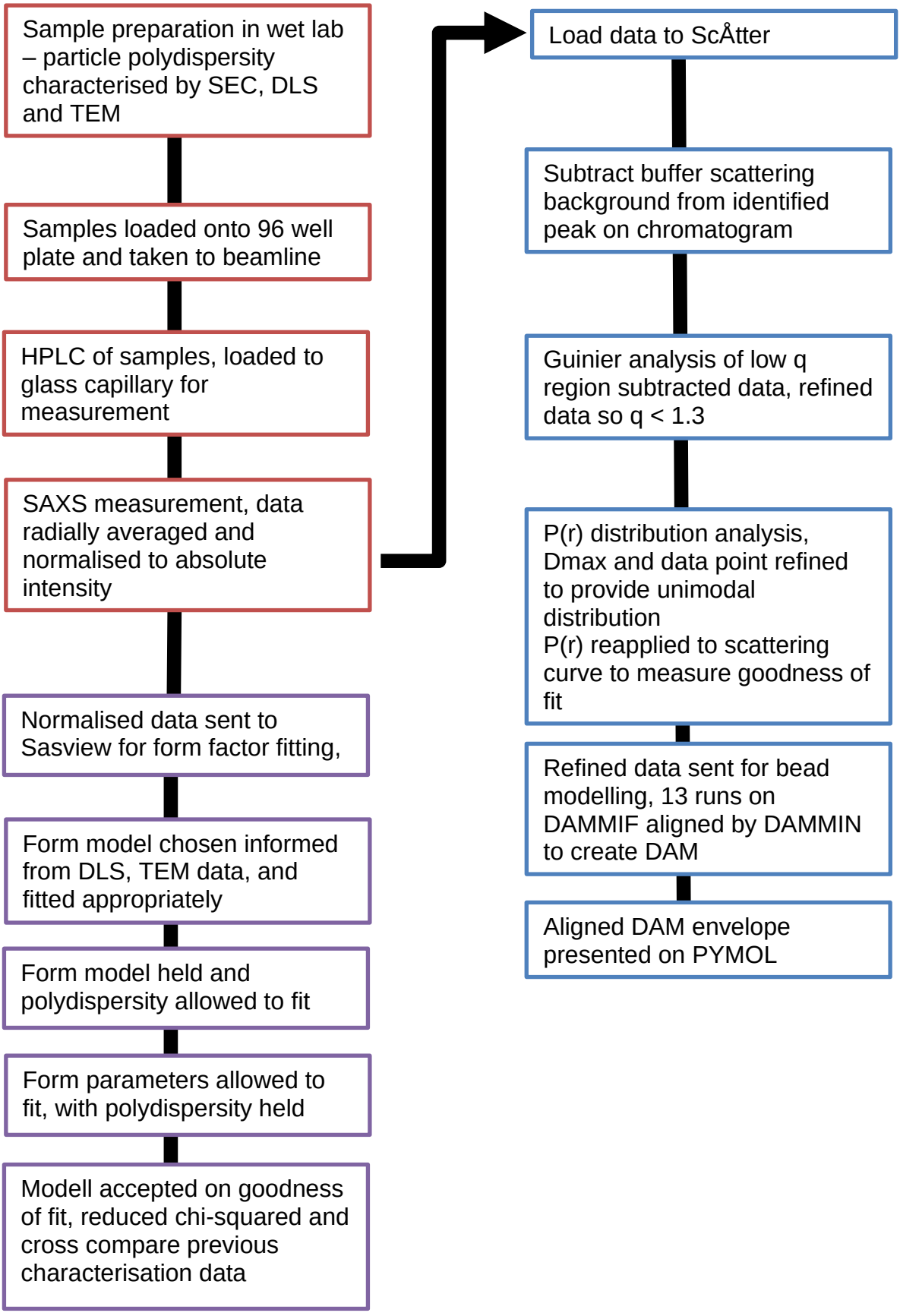

Figure 3.5 Workflow schematic of SAXS measurement and data analysis

SAXS measurement protocol (red), ScÅtter analysis and generation of bead model (blue) and Sasview form factor fitting (purple)

3.7 Aerobically mineralised SAXS results

3.7.1 Theoretical modelling of aerobically mineralised ferritin

Pf samples characterised as monodisperse and heterogenous from the aerobic mineralisation in Section 2.8.4 were analysed at the SAXS beamline (B21) at Diamond Light Source. These samples were subject to HPLC purification prior to measurement thus removing large particles, protein aggregates or contaminants that contribute to scattering intensities. The HPLC signal plot allowed for background subtraction. Normalised scattering intensity data were uploaded to ScÅtter to visualise the HPLC elution volume against scattering intensity as an integral of signal ratio against background. The signal plot was used to subtract a buffer background from the peak of eluting sample, grouped together for their consistent Rg. This peak was observed around 1.57 ml for all samples.

Frames, for which a consistent Rg was determined, were grouped together for background subtraction. This allowed for determination of sample quality with all six peaks displaying a consistent Rg number across the peak. This background subtracted peak gave a distinct scattering curve, for the apo-ferritin and lower iron concentrations where discreet fringes were present. As iron concentration increased the distinction of these fringes was less defined, Figure 3.7. The P(r) distribution analysis follows a similar trend as mineralisation concentration increases, with lower mineralisation ratios skewing the P(r) towards a higher radius value. In contrast, higher mineralisation ratios reported a lower particle radius, evident in Figure 3.6.

To understand particle interaction and monodispersity Guinier analysis software in ScÅtter was utilised. This checked for regression at low q and allowed the approximation of Rg and I(0). The Rg limits and reciprocal Rg and I(0) measurements calculated from this Guinier approximation are presented in Table 3-1. Appropriate, non-interacting monodisperse data with straight linear regression were then used for P(r) analysis using ScÅtter. Here, real space Rg, real space I(0) and Dmax approximations were made from the P(r) distribution, this data is compared with the reciprocal I(0) and Rg in Table 3-1. Goodness of fit was determined by comparing the P(r) fitting curve to the experimental scattering curve with Chi-squared ($\chi 2$) tests used to check accuracy of fitting. Similarly, previous particle characterisations with DLS and

TEM were considered when determining particle size through P(r) fitting. In addition, the numerical difference between real space and reciprocal space measurements were also used as a measurement of accuracy. For each iron loading ratio, there is a HPLC signal plot, scatter intensity plot, P(r) distribution and Kratky plot. The nomenclature corresponds to the target iron atom per ferritin molecule ratio based on protein concentration pre-mineralisation, e.g. Pf120 refers to 120 iron atoms per ferritin molecule. The apo- prefix refers to the ferritin molecule pre-mineralisation.

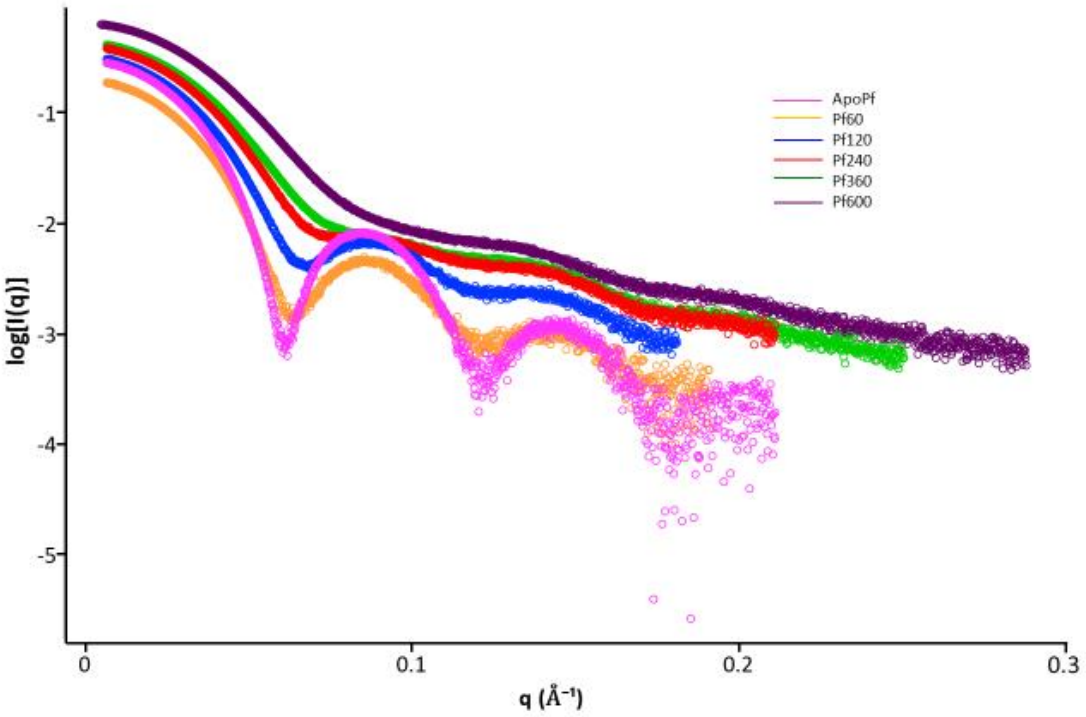

Figure 3.7 Log scatter intensity for aerobically loaded *Pf* ferritin

Log scattering intensity [I(q)] of mineralised Pf ferritin against the scattering vector (q) apoPf (pink) Pf60 (yellow) Pf120 (blue) Pf240 (red) Pf360 (green) Pf600 (purple)

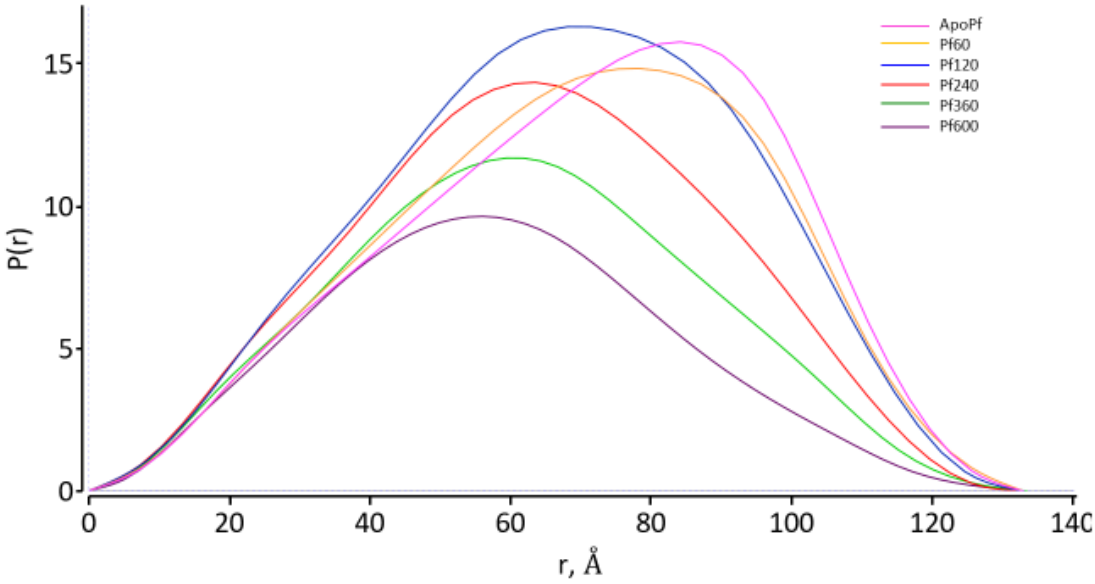

Figure 3.6 P(r) function for aerobically mineralised *Pf* ferritin

P(r) mineralised Pf ferritin. apoPf (pink) Pf60 (yellow) Pf120 (blue) Pf240 (red) Pf360 (green) Pf600 (purple)

Sample	q x Rg Guinier limits		I(0) Reci (Å)	I(0) Real (Å)	Rg Reci (Å)	Rg real (Å)	*r* average (Å)	*D*max (Å)	χ^2
apoPf	0.1766	1.2976	2.98 E -01	3.00 E-01	52.91	55.18	70.4	133	0.05
Pf60	0.1737	1.2957	1.93 E-01	1.98 E-01	51.84	54.28	68.9	133	0.06
Pf120	0.1683	1.2931	3.09 E-01	3.22 E-01	50.39	52.60	66.9	133	0.02
Pf240	0.1603	1.2842	3.80 E-01	3.98 E-01	48.29	50.10	63.7	133	0.05
Pf360	0.1544	1.2984	4.15 E -01	4.27 E-01	47.03	48.26	61.8	133.5	0.12
Pf600	0.1459	1.2998	6.45E -01	6.45 E-01	44.65	45.60	58.4	132.5	0.20

Table 3-1Small angle X-ray scattering size parameters of aerobically loaded *Pf* ferritin

SAXS size parameters as described by ScÅtter, reciprocal data (Reci) calculated from the Guinier approximation compared with real space (real) calculated from P(r).

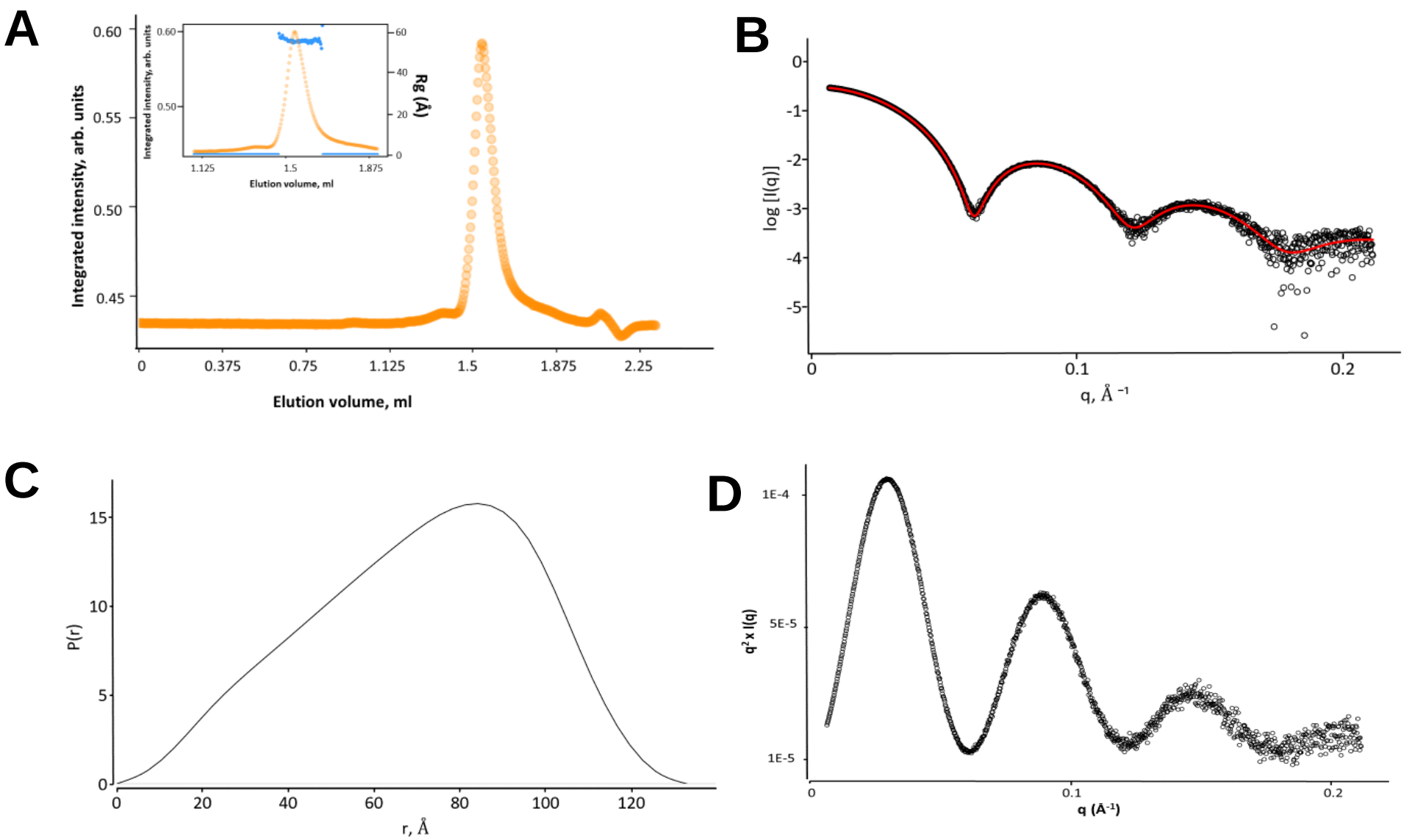

Figure 3.8 Small angle X-ray scattering analysis of apoPf

(A) HPLC signal plot with peak at 1.57 ml. (Inset) Rg across elution peak (B) Scatter intensity curve (black) fit to the P(r) analysis (red) (C) P(r) model histogram. (D) Kratky plot

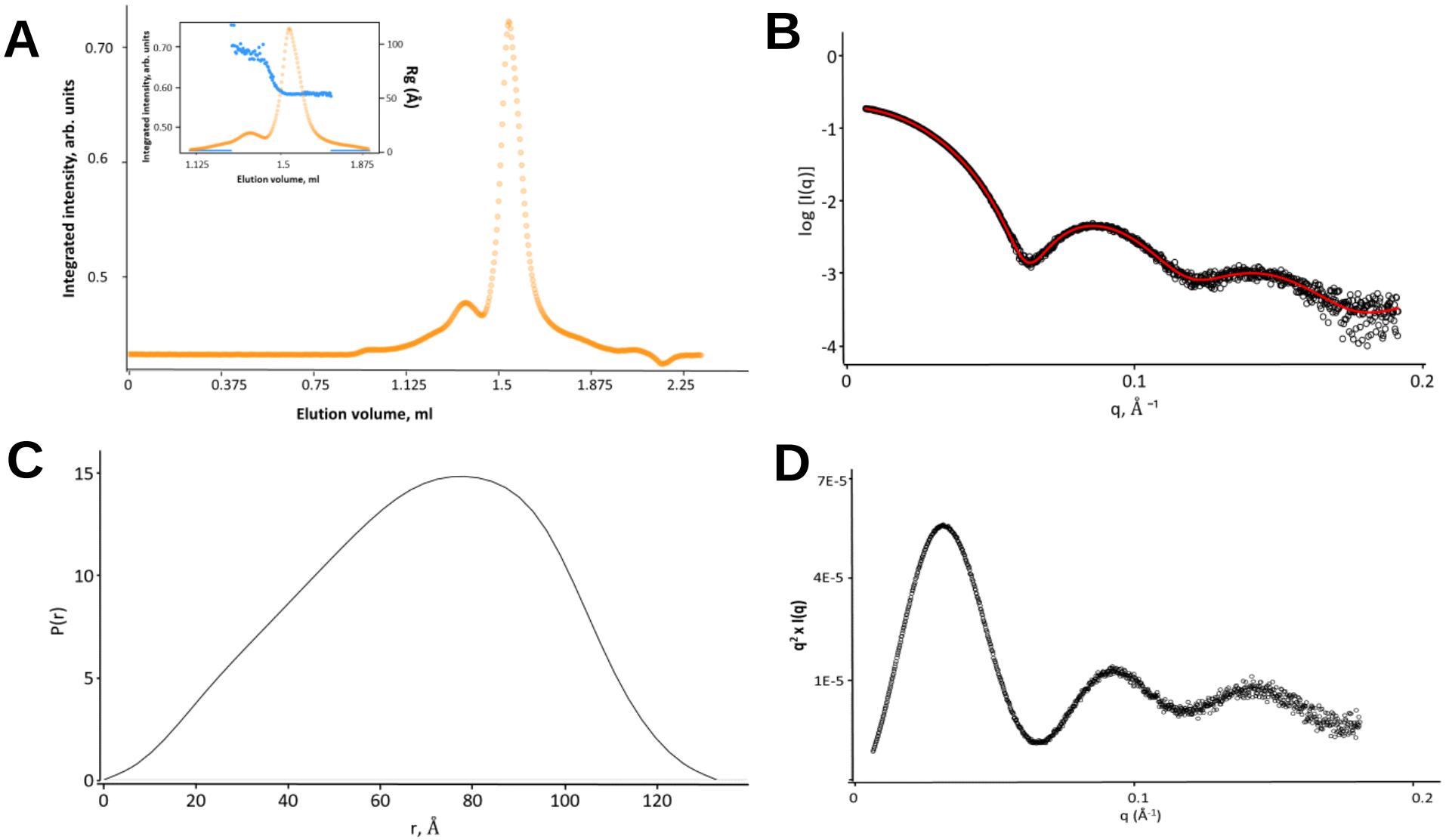

Figure 3.10 Small angle X-ray scattering analysis of Pf60

(A) HPLC signal plot with peak at 1.57 ml. (Inset) Rg across elution peak (B) Scatter intensity curve (black) fit to the P(r) analysis (red) (C) P(r) model histogram. (D) Kratky plot

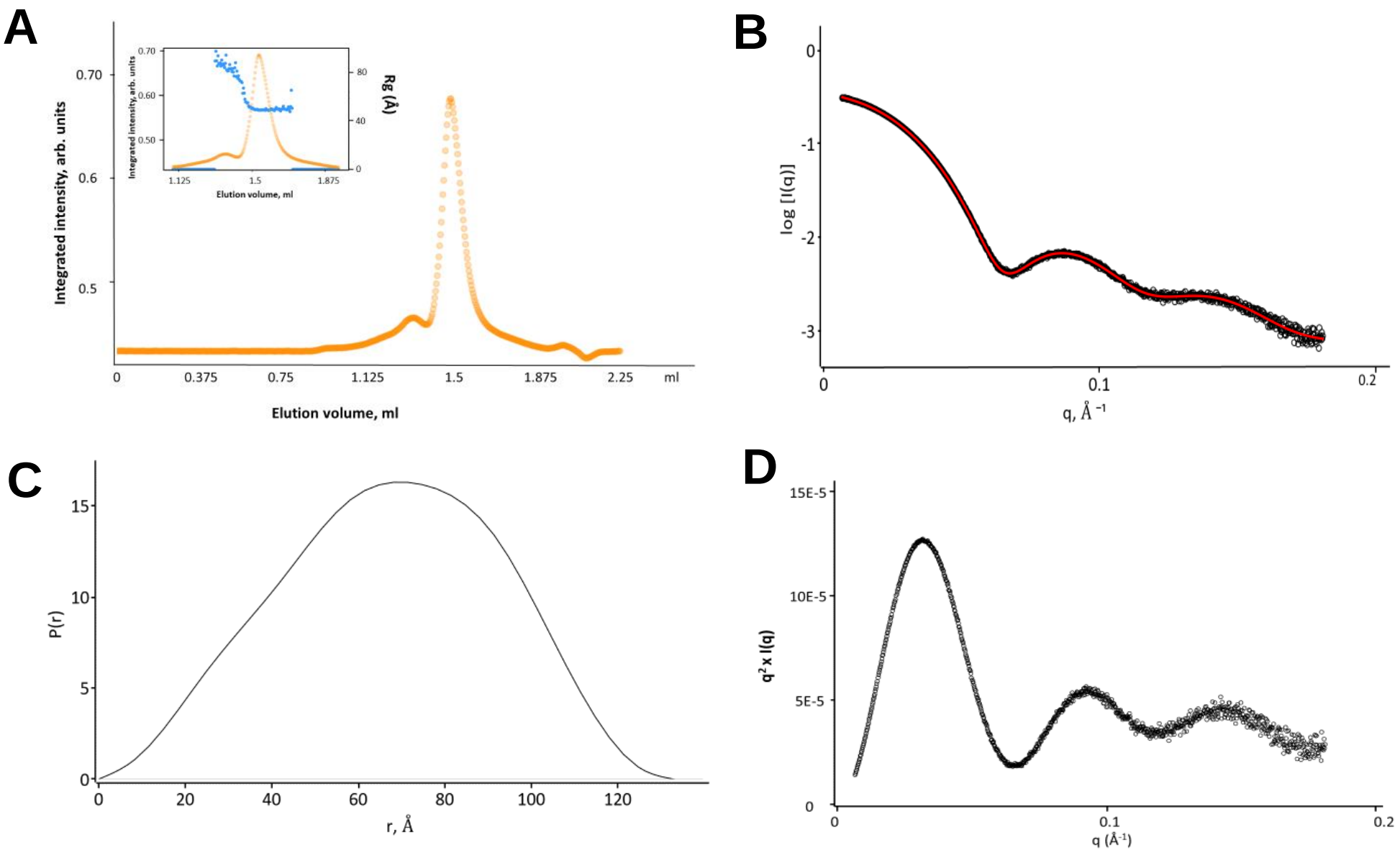

Figure 3.12 Small angle X-ray scattering analysis of Pf120

(A) HPLC signal plot with peak at 1.57 ml. (Inset) Rg across elution peak (B Scatter intensity curve (black) fit to the P(r) analysis (red) (C) P(r) model histogram. (D) Kratky plot

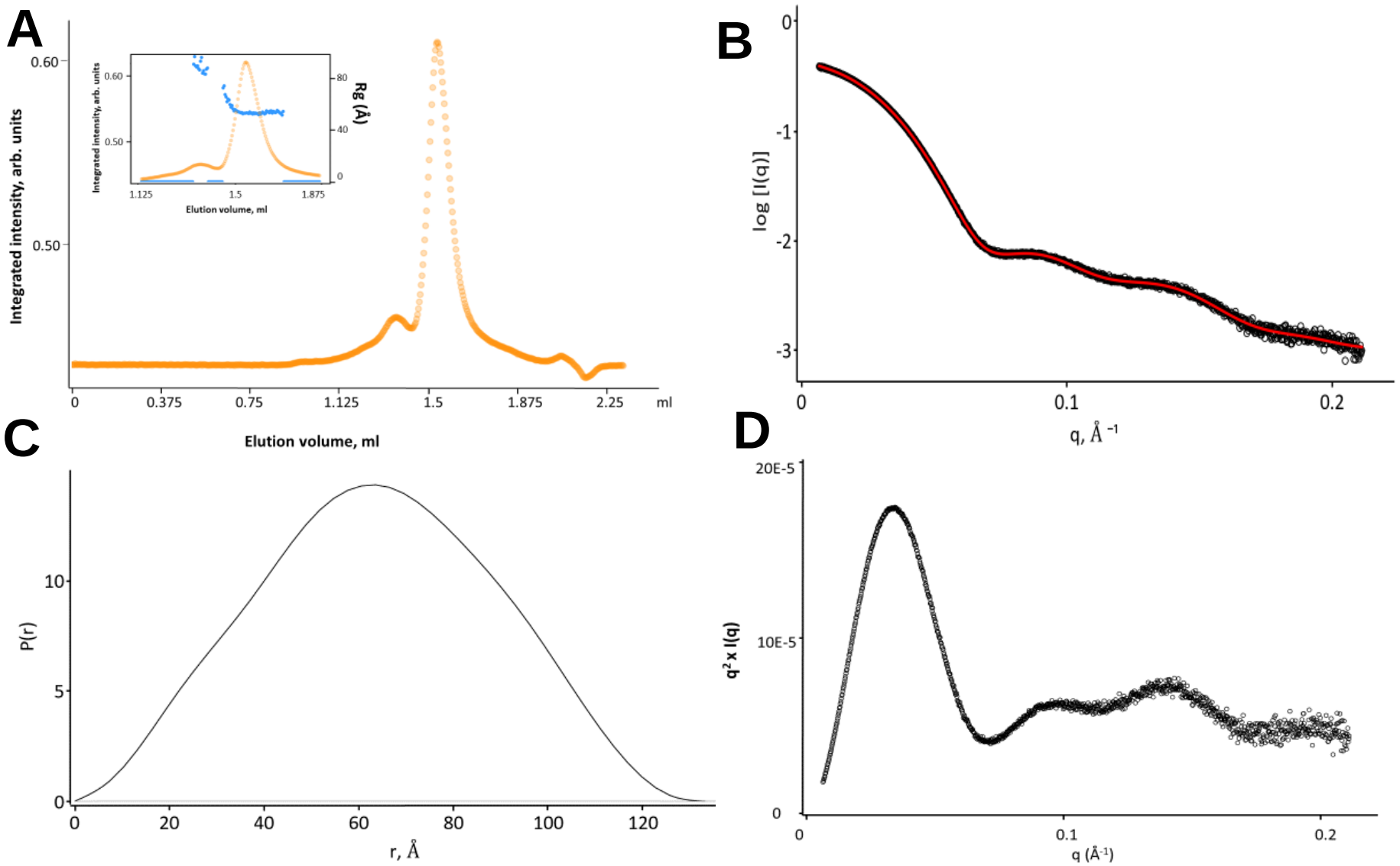

Figure 3.14 Small angle X-ray scattering analysis of Pf240

(A) HPLC signal plot with peak at 1.57 ml. (Inset) Rg across elution peak (B) Scatter intensity curve (black) fit to the P(r) analysis (red) (C) P(r) model histogram. (D) Kratky plot

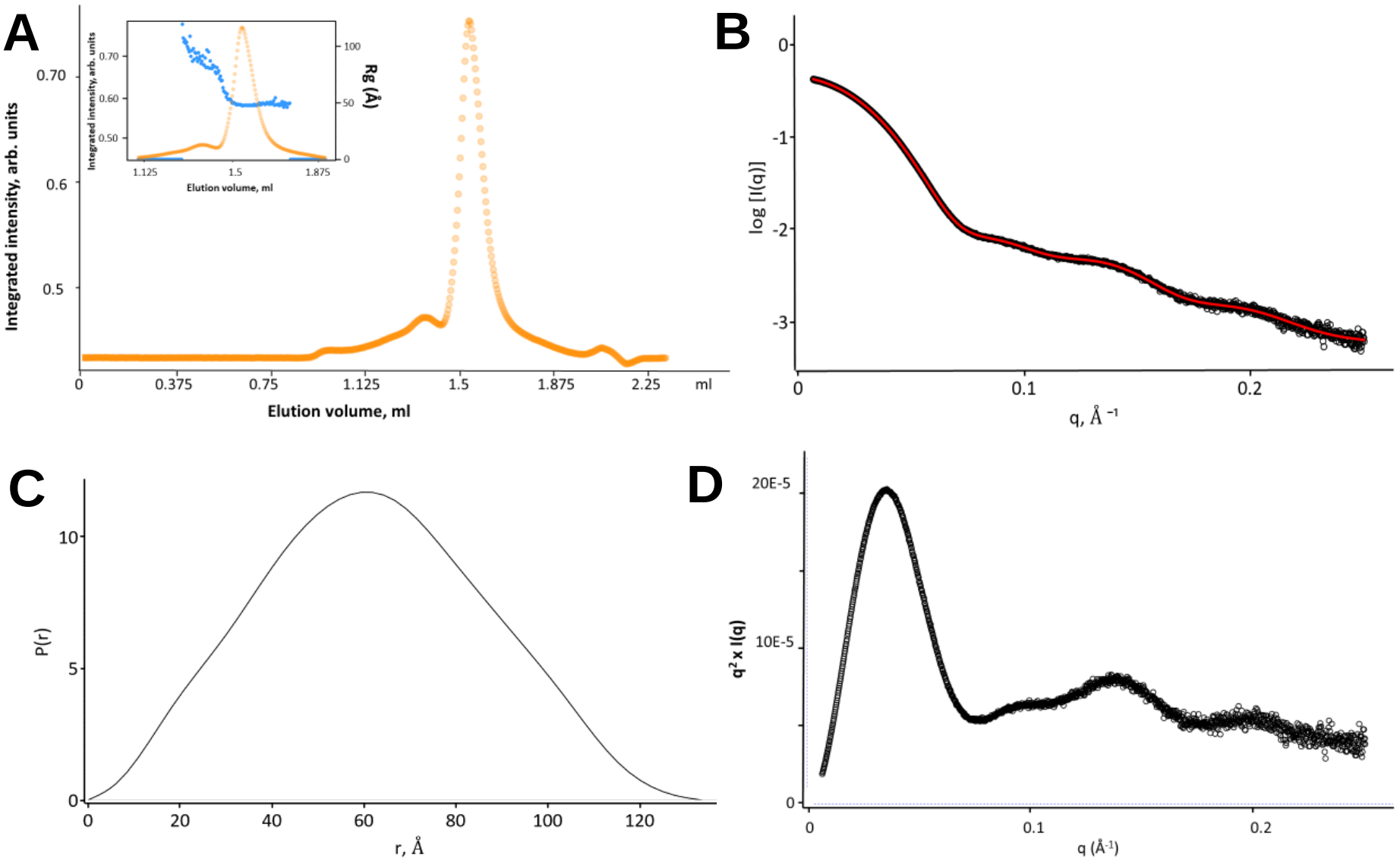

Figure 3.17 Small angle X-ray scattering analysis of Pf360

(A) HPLC signal plot with peak at 1.57 ml. (Inset) Rg across elution peak (B) Scatter intensity curve (black) fit to the P(r) analysis (red) (C) P(r) model histogram. (D) Kratky plot

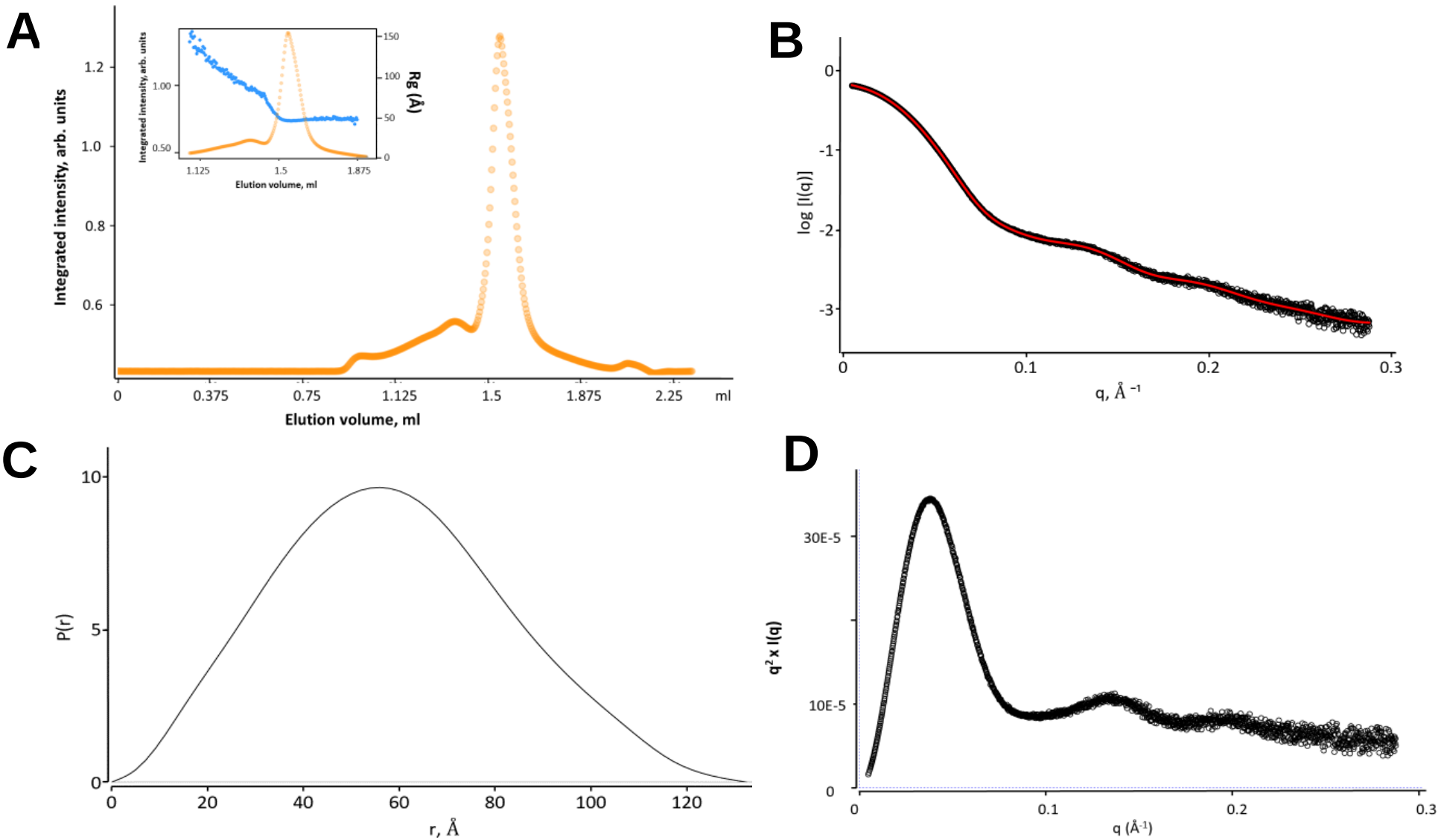

Figure 3.19 Small angle X-ray scattering analysis of Pf600

(A) HPLC signal plot with peak at 1.5 ml. (Inset) Rg across elution peak (B) Scatter intensity curve (black) fit to the P(r) analysis (red) (C) P(r) model histogram. (D) Kratky plot

There was confidence in ferritin particle identification from the HPLC signal plot with, with all six samples eluting as a clear peak at the same elution volume. Small peaks before the identified ferritin peak between 1.125 ml and 1.5 ml, seen in the apoPf HPLC trace, could be identified as aggregated particles and were discounted from further investigation do to their heterogeneous Rg on initial data inspection. From Table 3-1 it is evident that as iron loading concentration increases the real space Rg and reciprocal space Rg decreases, this may be explained by the smaller electron dense iron oxide core overpowering the scattering intensity of the protein shell. The apoPf radius seen here of 70 Å is in line with previous TEM measurements and DLS measurement and differs by 9 Å from measurements seen for Hsf measured at 61 Å by Fischbach et al. [81].

With the Guinier region of the scattering curve being a representation of particle size, ferritin size homogeneity across the iron mineralisation ratios is also evident from the shape of the curve below 0.1 Å. Higher q regions, just after the Guinier region, reflect a particles shape, and the fringes seen in the log scattering intensity plot at lower iron concentrations are characteristic of those seen for hollow sphere structures. Such fringes are seen in other SAXS analysis of horse spleen apo-ferritin by Kuklin et al [82]. As evident in Figure 3.7, the fringes become less distinct at higher mineralisation iron ratios as the iron begins to occupy the particle cavity.

As evident in Figure 3.6, there is a clear trend in P(r) as iron loading ratios increases, the D-max remains fairly homogenous through all six samples, however the distribution changes as iron concentration increases. At lower iron ratios there is a skewing of distribution to higher r values. The distribution for apoPf is skewed towards a higher r of 85 Å, characteristic of hollow sphere particles and identical to the SAXS analysis by Kuklin et al. [82]. As iron loading increases, the distribution becomes more evenly distributed around 55 Å, seen especially for the Pf600 sample, more characteristic of a filled sphere and in line with SAXS analysis of Hsf by Melníková et al. [83]. The P(r) all demonstrate homogeneity and monodispersity, without undulations with no irregularities in fitting. Furthermore, the distributions present a $P(r)$ value of zero at r=0 representative of globular, folded particles. Similarly, all P(r) histograms present a Dmax value of zero, an indication of sample monodispersity.
Demonstrated in Figure 3.9 through Figure 3.20, the P(r) complement the scattering curves with P(r) fitting compared to the experimental data as a red line, it is this P(r)

that is the foundation for *ab initio* bead modelling and will serve as a reference in form factor modelling.

Considering the Kratky analysis for each sample there is a clear peak signifying the presence of globular folded particles. Evident at lower mineralisation ratios, the Kratky peak converges towards the q axis but is followed by a second and third peak at high q values. These correspond to the fringes seen in the scattering plot and are representative of the domains within a hollow sphere. As seen with the scattering curve, the increased iron loading ratios contributes to these multidomain peaks becoming less distinct.

This analysis is vital for the generation of ab *initio* bead models and will inform the form factor fitting in Section 3.7.3. Combining these techniques will provide a better understanding of how the iron reconstitutes inside the particle and contributes to the distinctive scattering patterns seen in this scattering analysis.

3.7.2 Envelope modelling of aerobically mineralised ferritin

The P(r) of the experimental data for each mineralisation ratio were by the dummy atom modelling software DAMMIN/F. The *ab initio* bead modelling program builds an interconnected DAM from an arbitrary initial model through annealing to find a configuration that fits the data set while minimising interfacial area. An additional subprogram aligned the thirteen DAMs for each iron loading concentration and these models are presented in PYMOL, Figure 3.21.

This bead modelling provides perspective on atom configuration of the particle and provides *a priori* evidence on particle shape and structure which will facilitate form factor fitting. From the bead modelling it is evident that there is a clear spherical arrangement seen in the apoPf, Figure 3.21A, as expected for a ferritin nanoparticle. As iron loading concentration increases the model loses its uniform spherical shape and becomes more irregular. Finally, resulting in the more ellipsoid shape seen for Pf600, Figure 3.21F. Because the algorithms in the DAMMIF software only distinguish either particle (index=1) or solvent (index=0), there is no distinction between types of atom i.e. protein shell or iron core. It is reasonable to interpret the loss of homogeneity in DAM shape in response to concentration increase, as the iron oxide core forming within the particle. Iron oxide has a greater SLD than the protein and this overpowers the scattering from the protein shell. Therefore, the DAM could be perceived as a representation of the electron dense iron oxide core rather than the electron lucent protein shell, when combined with the TEM analysis, where data provides evidence that the shell is present and appears unchanged as iron populates the particle cavity. Further characterisation in form factor fitting is required to support the bead modelling and distinguish shape, structure, and polydispersity in relation to the previous characterisations using TEM and DLS.

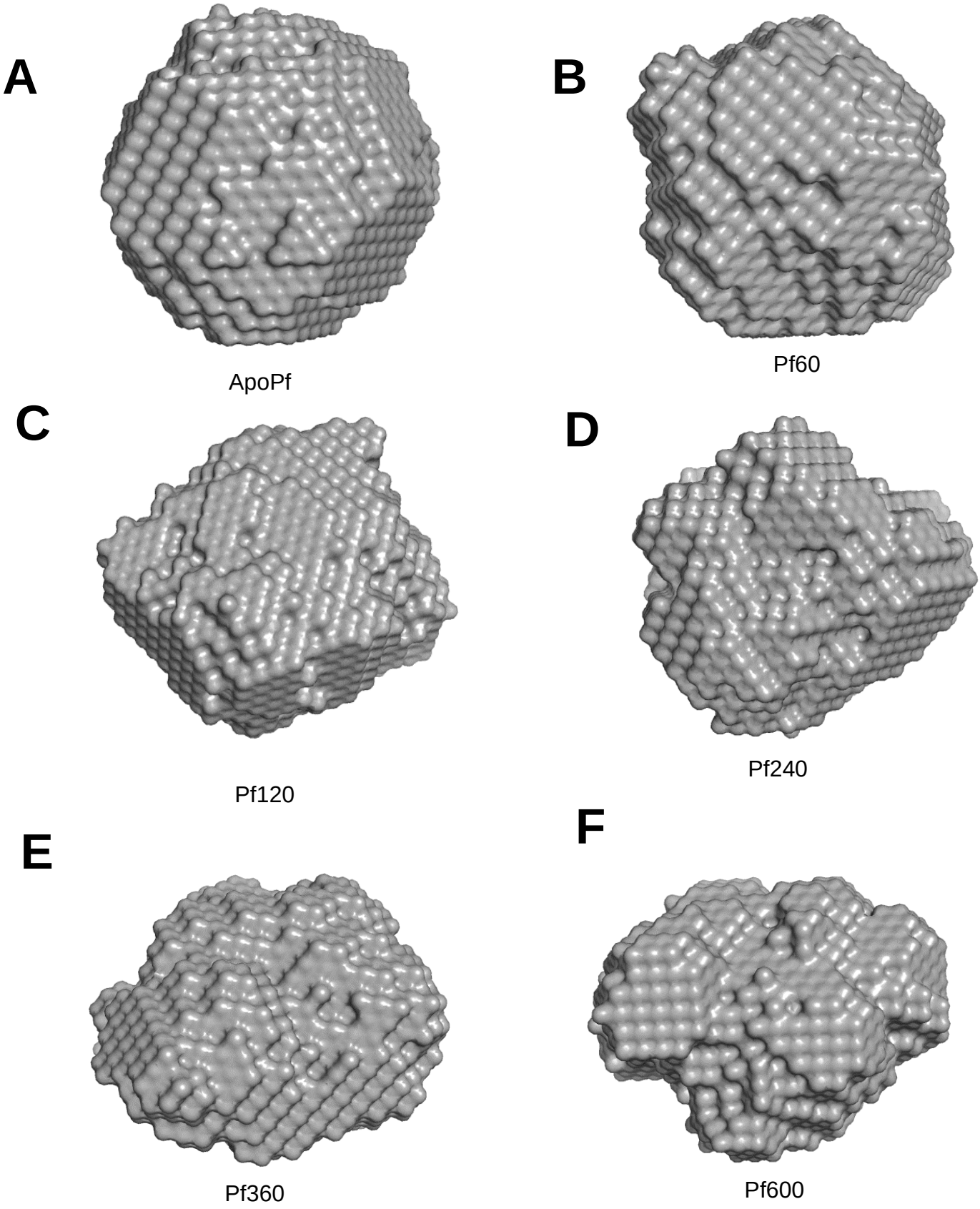

Figure 3.21 *Ab initio* bead models of aerobically mineralised ferritin

Ab initio bead models generated using the DAMMIN/F from the ATSAS suite, presented in PYMOL (A) ApoPf (B) Pf60 (C) Pf120 (D) Pf240 (E) Pf360 (F) Pf600

3.7.3 Form factor modelling of aerobically mineralised ferritin

Form factor fitting was performed using Sasview. This software has a library of form factor calculations and mathematical definitions provided by the NIST Centre for Neutron Research. Parameters can be adjusted on the user interface and fitting validation plots are tested against scattering data to provide a reduced chi-squared ($\chi 2$) result as an indication of fitting accuracy. Three iron loading ratios were focused on here in addition to apo-Pf. Pf60, Pf120 and Pf600 because they displayed an informative range of scattering data across the iron loading concentrations.

Considering the shape and structure of *Pf* ferritin reported in the literature, and the characterisations using TEM and DLS, there is strong evidence towards this recombinant *Pf* ferritin forming spherical nanocages. This was further supported by the scattering curves and P(r) plots, and the resulting *ab initio* bead modelling in Section 3.7.2. With such extensive *a priori* information it was rational to fit a core-shell model to the apoPf data shown in Figure 3.23. Again, there are clear distinct fringes indicative of a monodisperse hollow sphere with a radius of 60 Å.

For the mineralised samples, two models were compared to deduce how the iron oxide core is reconstituting within the protein shell. Based on observations by Le Vay [51] and Theil [33], that iron oxide could build up on the exit of four-fold and three-fold symmetry channels, it was rational to fit a multi-shell model alongside the core-shell model to explain anomalies in outer shell SLD. It is plausible that there are intermediary phases between apo-ferritin and mineralised ferritin, as iron travels through the channels, building up on ferroxidase areas on the exit before being displaced into the core, as explained in Figure 3.22.

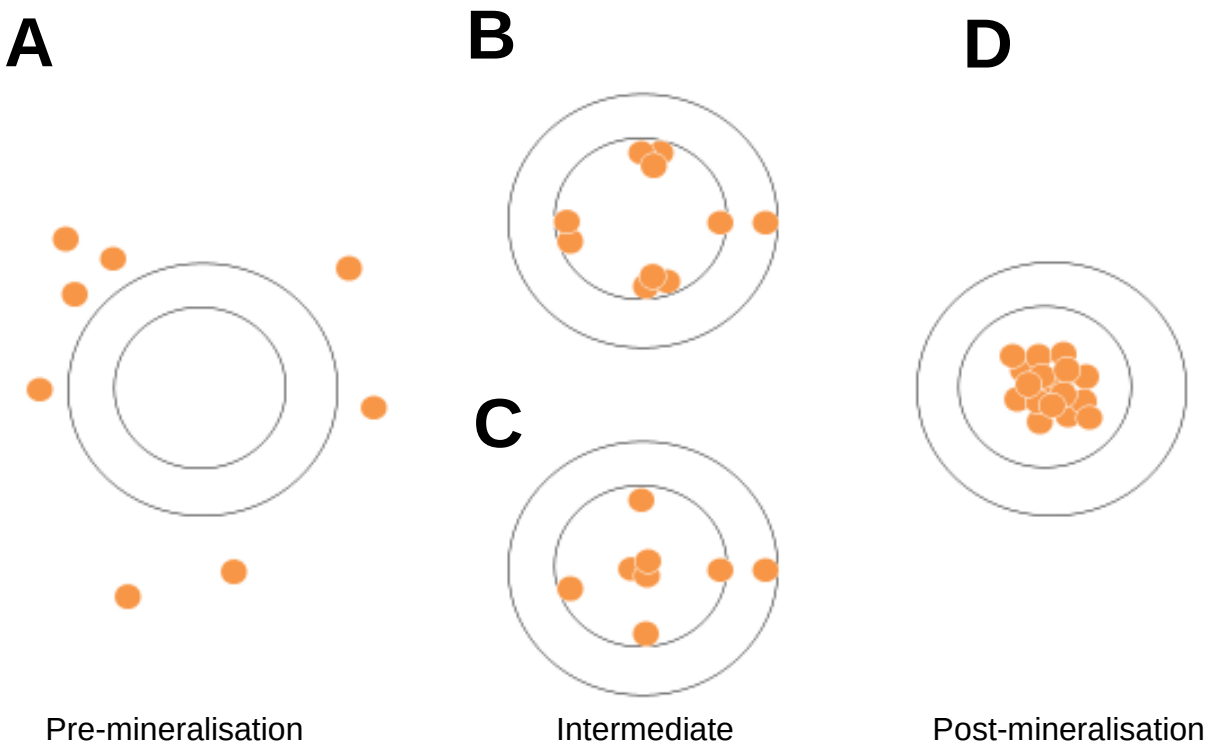

Figure 3.22 Schematic of iron deposition inside ferritin core

Cross section schematic of ferritin particle (A) Core-shell model of ferritin pre-mineralisation with iron (orange), (B) Potential location of iron at the exit of ion channels (C) Potential location of iron with more centralised core formation as iron is displaced into the core. (D) Reconstitution of iron oxide inside the ferritin core post mineralisation

The two sphere models for a particle with a radius of 60 Å (Figure 3.23) were fitted to the experimental data according to the workflow outlined in Figure 3.23. Accuracy and goodness of fit were judged by reduced chi-squared and cross compared with previous characterisations. The core-shell model for a particle with a total radius of 60 Å, was based on the reported particle core diameter being 80 Å and therefore the outer shell thickness being 20 Å [33]. Being a hollow sphere, core SLD was matched to that of the solvent in line with the literature value of 9.43 x 10^{-6} $Å^{-2}$. Outer shell SLD was set to 12.5 x 10^{-6} $Å^{-2}$, a rational figure for proteins as seen in previous ferritin fittings [51]. With the multi shell model, outer shell SLD and outer shell thickness were fixed at pre-determined values. The inner shell and core parameters fitted by Sasview. With a total particle radius of 60 Å, an SLD for the core (pcore) was applied from previous fitting examples (28 x 10^{-6} $Å^{-2}$) and a core radius (rcore) of 30 Å was set, reflecting the core shell model. The outer shell thickness (t2) was set at 20 Å and outer shell SLD (p2) was fixed at 12.5 x 10^{-6} $Å^{-2}$. The inner shell thickness (t1) was calculated as 20 Å and a similar inner shell SLD (p1) of 10 x 10^{-6} $Å^{-2}$ was chosen close to the literature value of the SLD of the solvent (9.43 x 10^{-6} $Å^{-2}$).

This core-shell model, fitted the apoPf scattering data, effectively returning a total radius of 64.72 Å and resulting in a chi-squared of 2.26. This fit did not provide any information on core size with the SLD of the protein shell and particle core being very similar (Table 3-2). As seen in Figure 3.24, the characteristic fringes associated with the scattering profile of a core-shell sphere are represented in the experimental scattering data as well as the computational model. Core-shell fitting of Pf60 scattering data was suitable (Figure 3.24), yielding a total radius of 64.96 Å and a chi-squared of 3.79. There was little difference between the form factor values for these samples, indicating that such low iron mineralisation ratios have little impact on scattering curve. Form factor fitting was extended to the scattering data for the mineralised ferritin, to understand how the iron core reconstitutes inside the nanoparticle and, how this

relates to the scattering intensity profile and ultimately the difference in particle homogeneity as seen in the *ab initio* models.

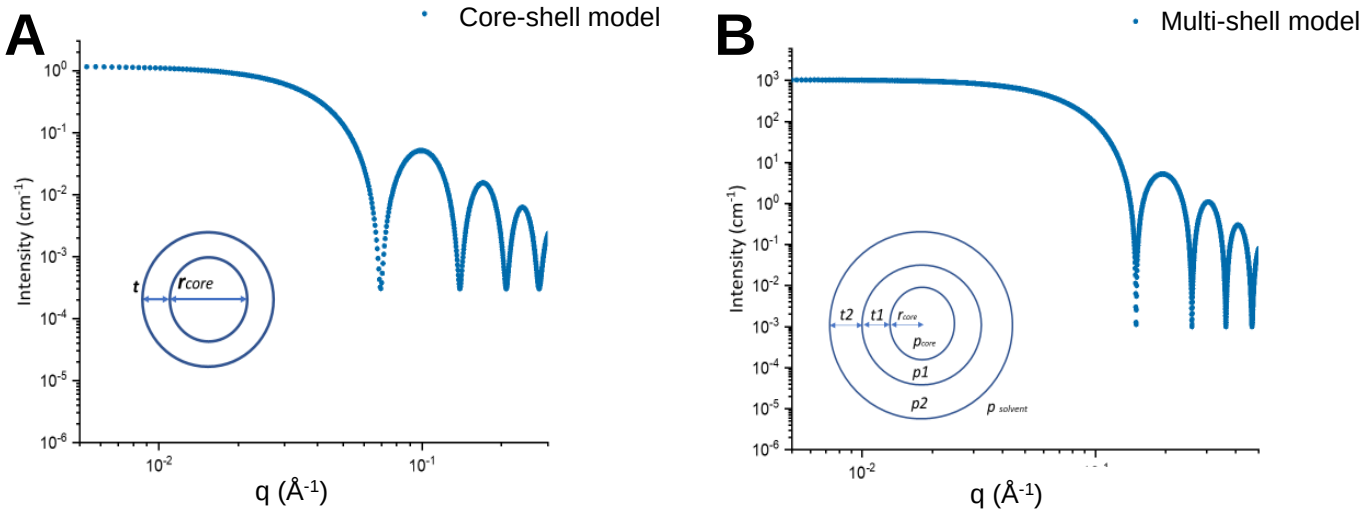

Figure 3.23 Form factor fitting sphere models

(A) Core-shell form factor model for a monodisperse particle with a total radius of 60 Å, a core radius of 40 Å and a shell thickness t1 of 20 Å. (B) Core-shell model for a spherical particle with a radius of 60 Å. Inner core SLD (pcore) and radius (rcore) fixed from previous fitting. Inner shell SLD (p1) fixed equal to solvent, inner shell thickness (t1). Outer shell SLD (p2) and thickness (t2) fixed in line with parameters described by Le Vay [51].

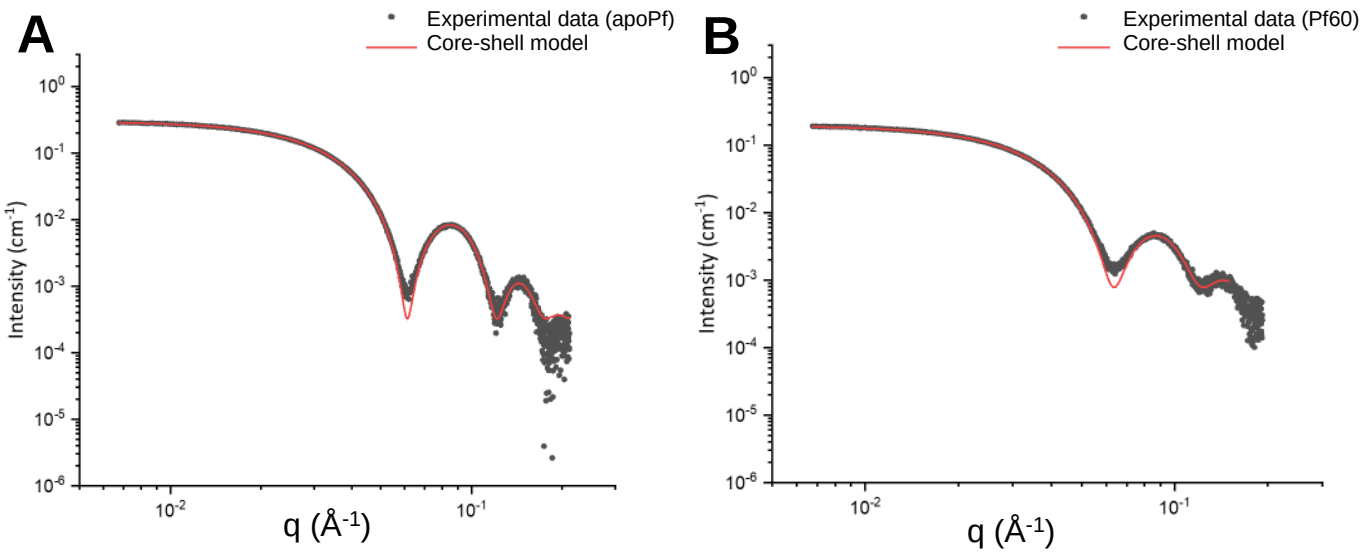

Figure 3.24 Form factor fitting for apoPf and Pf60

(A) Core-shell form factor fitting for normalised apoPf scattering intensity performed with Sasview, solvent SLD fixed from published data. Model returned a chi-squared of 2.26 and a particle radius of 64.72 Å (B) Core-shell form factor fitting for normalised Pf60 scattering curve, returning a chi-squared of 3.79 and a particle radius of 64.96 Å.

Table 3-2 Core-shell model fitting parameters for apoPf

Parameter	Core Shell Model	ApoPf fitting	Pf60 fitting
Background (cm^{-1})	3.0e-4	3.0e-4 ± 3.9 e-6	7.0e-4 ±5.59 e-6
Core radius (Å)	40	34.61 ±0.007	29.09 ±0.013
Shell thickness (Å)	20	30.11 ±0.005	35.87 ±9.8e-4
SLD core ($10^{-6}Å^{-2}$)	9.43	9.43 ±2.5e-4	9.45 ±6.0e-4
SLD thickness ($10^{-6}Å^{-2}$)	12.5	10.06 ±6.6e-5	9.95 ±9.2 e-5
SLD solvent ($10^{-6}Å^{-2}$)	9.43	9.43 ±5.3e-5	9.45 8.18 e-5
Total Radius (Å)	60	64.72	64.96
χ2		2.26	3.79

In view of the high chi-squared values, it was evident that the core-shell model used in the analysis of apoPf did not fit the experimental data (Pf120 through to Pf600). Core-shell and multi-shell form factor models were fitted to normalised Pf120 scattering data, (Figure 3.25) with the parameters detailed in Table -3-3. Firstly, the core-shell model returned a radius of 63.63 Å, however the chi-squared value was high (30.41). Secondly, a multi-shell model was fit to the scattering data for Pf120, this complex model returned a total particle radius of 68.95 Å, and a chi-squared value of 34.14. Investigation into the particle radius found the outer shell SLD and thickness to be arbitrary, as changing these parameters did not affect the chi-squared result.

To improve the chi-squared value, the Schulz PDR was implemented as a number-distribution to the scattering parameters. Considering the core shell fitting of the Pf120 scattering data, a PDR of 0.2 was applied to the core radius, this resulted in a total particle radius of 58.70 Å and a chi-squared of 3.98. Again, a Schulz PDR function was applied to the multi-shell fitting of Pf120 scattering data. With a PDR of 0.14 fitted to the core radius and 0.09 applied to the outer shell thickness, this returned a total radius of 67.25 Å, with a chi-squared value of 2.80.

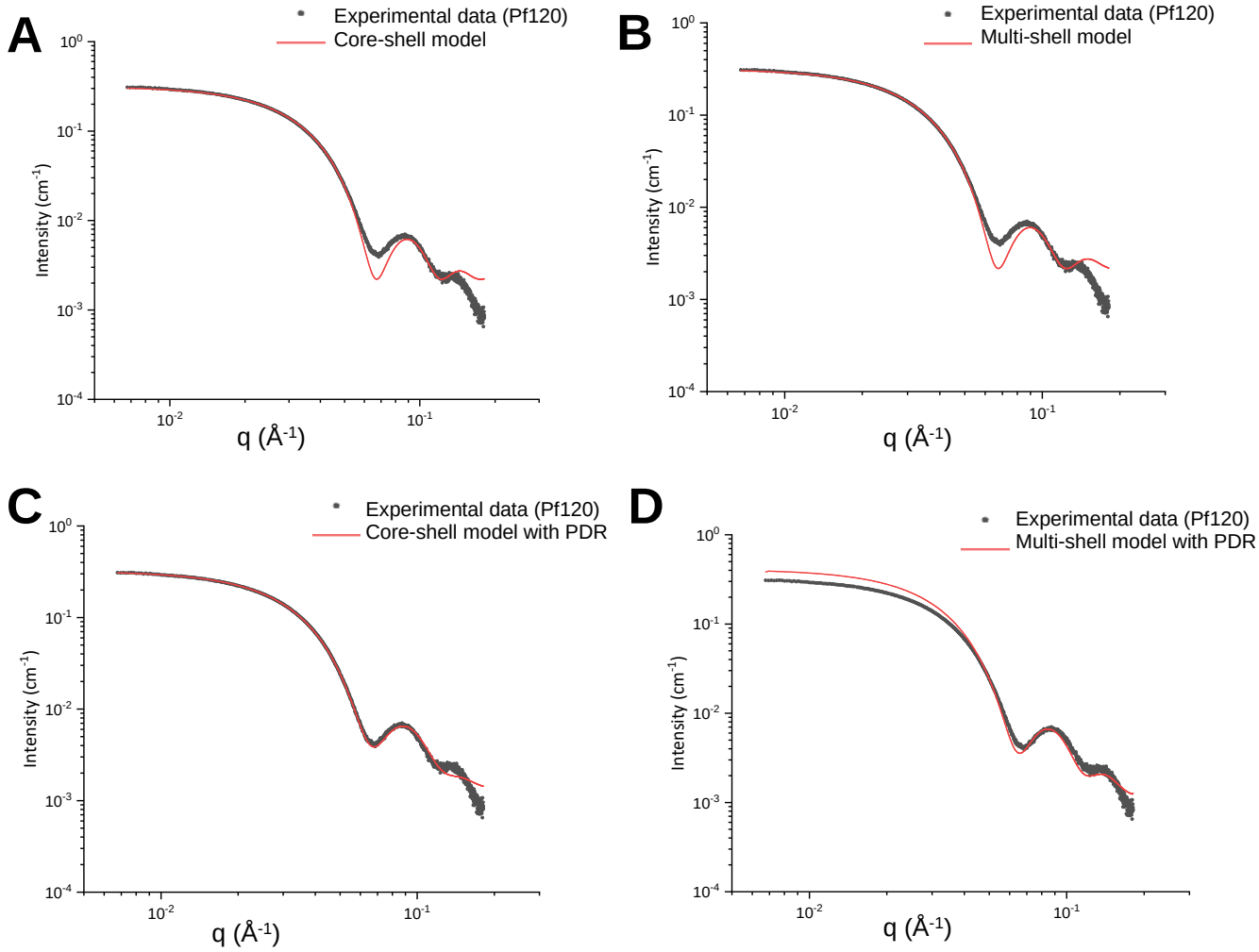

Figure 3.25 Form factor fitting for Pf120

Form factor fitting for normalised Pf120 scattering data (A) Core-shell modelling returned a chi-squared of 30.41 and a total particle radius of 63.63 Å (B) Multi-shell fitting returned a chi-squared of 34.14, with a total particle radius of 68.95 Å. (C) Core-shell form factor returned a chi-squared of 3.98 with a particle radius of 58.70 Å, with 0.20 PDR fitted to radius (D) Multi-shell form factor fitting returned a chi-squared of 2.80 with a particle radius of 67.25 Å, with 0.14 PDR fitted to radius and 0.09 PDR fitted to inner shell

Table -3-3 Form factor modelling parameters for Pf120

Parameter	Core shell	Multi shell	Core Shell w PDR	Multi shell w PDR
Background (cm^{-1})	0.002 ±5.9e-6	0.002 ±5.8e-6	0.001 ±5.7e-6	2.0e-4 ±5.6e-6
Core Rradius (Å)	33.95 ±0.008	48.90 ±0.008	31.60 ±0.011	50.80 ±0.007
Thickness 1 (Å)	29.68 ±0.007	0.39 ±0.003	27.10 ±0.012	9.25 ±0.002
Thickness 2 (Å)		19.67 ±0.006		7.20 ±0.002
SLD core ($10^{-6}Å^{-2}$)	9.95 ±4.0e-4	10.34 ±0.008	9.60 ±0.002	9.72 ±8.0e-5
SLD thickness1 ($10^{-6}Å^{-2}$)	10.2 ±1.2e-4	50.06 ±0.25	10.28 ±2.0e-4	10.61 ±2.0e-4
SLD thickness 2 ($10^{-6}Å^{-2}$)		10.06 ±0.014		9.13 ±1.0e-4
SLD solvent ($10^{-6}Å^{-2}$)	9.43 ±9.6e-5	9.42 ±1.0e-4	9.43 ±4.0e-4	9.43 ±4.3e-5
Total Radius (Å)	63.63	68.95	58.70	67.25
χ2	**30.41**	**34.14**	**3.98**	**2.80**

Normalised Pf600 scattering data (Figure 3.26) with the fitting parameters, described in Table 3-4 were fit with core-shell and multi-shell models. The core-shell fitting returned a total particle radius of 69.3 Å and a chi-squared value of 23.29. A multi shell fitting of the Pf600 scattering data reported an increased total radius of 76.70 Å and a chi-squared value of 32.06. Because of such a high chi-squared value it was suitable to investigate these fittings with a Schulz PDR on individual parameters. With the core shell fitting of Pf600 scattering data a PDR of 0.46 was applied to the core radius, this resulted in a total particle radius of 61.90 Å and a chi-squared value of 5.66. Likewise, a Schulz PDR was applied to the multi-shell fitting parameters, with a PDR of 0.2 applied to the core radius and 0.80 applied to the outer shell. This returned a chi-squared value of 4.81 with a total particle radius of 73.09 Å.

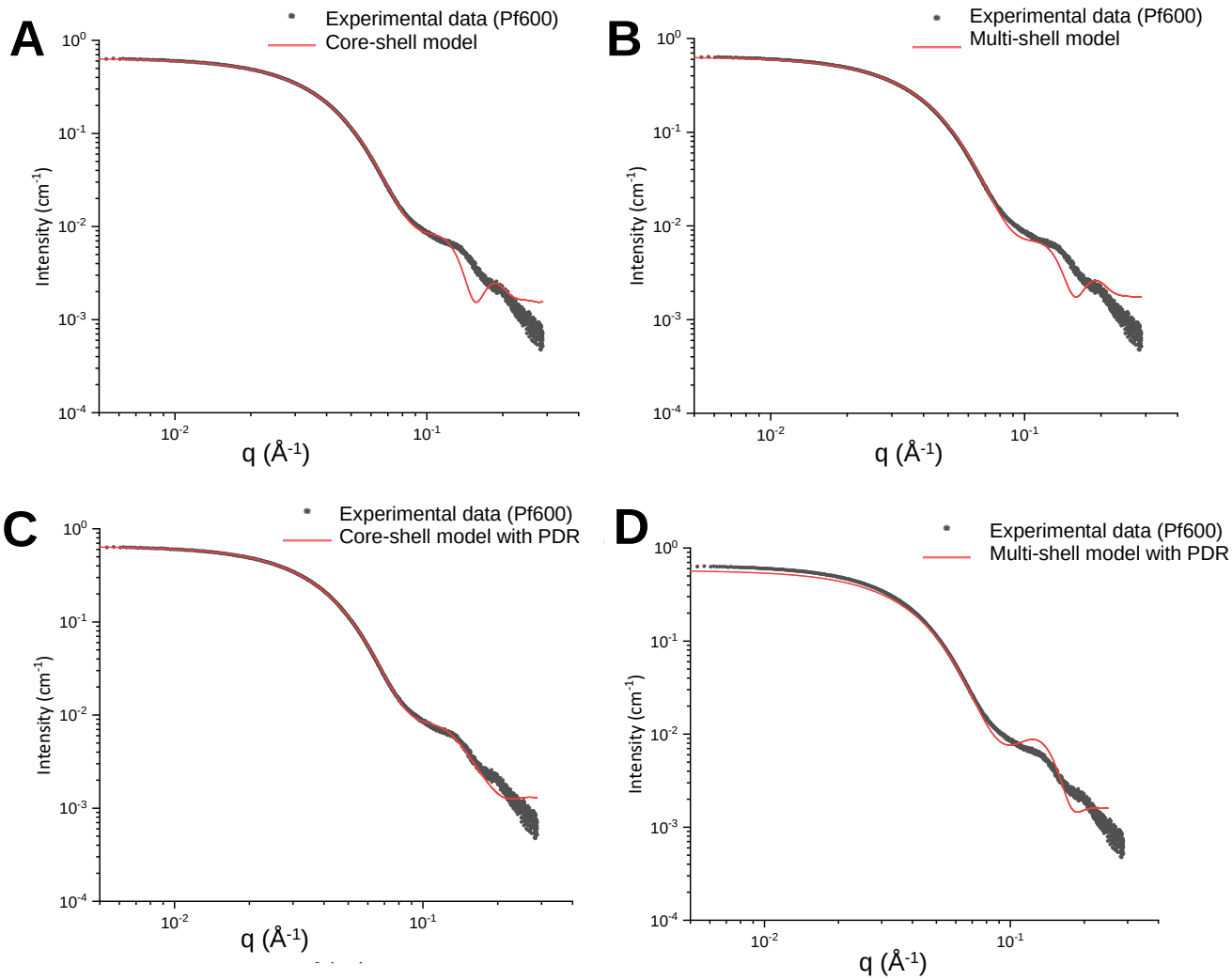

Figure 3.26 Form factor fitting for Pf600

Form factor fitting for normalised Pf600 data (A) Core-shell modelling returned a chi-squared value of 23.29 and a total particle radius of 69.30 Å (B) Multi-shell fitting returned a chi-squared of 32.06, with a total particle radius of 76.70 Å. (C) Core-shell form factor returned a chi-squared of 5.66 with a particle radius of 61.90 Å, with PDR of 0.46 fitted to core radius (D) Multi-shell form factor fitting returned a chi-squared of 4.81 with a particle radius of 73.09 Å, with PDR 0.2 fitted to radius and a PDR of 0.8 fitted to outer shell.

Table 3-4 Form factor modelling parameters for Pf600

Parameter	Core shell	Multi shell	Core shell w PDR	Multi shell w PDR
Background (cm^{-1})	0.001 ±4.7e-6	0.002 ±4.8e-6	0.001 ±6.5e-6	0.001 ±5.36e-6
Core radius (Å)	28.71 ±0.002	28.60 ±0.002	18.23 ±0.19	22.71 ±0.001
Thickness 1 (Å)	40.60 ±0.005	38.10 ±0.005	43.675 ±0.04	39.79 ±0.003
Thickness 2 (Å)		10.00 ±0.005		10.50 ±0.003
SLD core ($10^{-6}Å^{-2}$)	65.97 0.007	67.94 ±0.007	73.22 ±1.75	60.45 ±0.007
SLD thickness1 ($10^{-6}Å^{-2}$)	16.10 ±0.001	17.16 ±0.001	15.33 ±0.17	15.02 ±8.4e-4
SLD thickness 2 ($10^{-6}Å^{-2}$)		10.10 ±0.003		10.30 ±0.002
SLD solvent ($10^{-6}Å^{-2}$)	9.43 ±0.001	9.34 ±0.001	9.44 ±0.003	9.49 ±5.0
Total Radius (Å)	69.31	76.70	61.90	73.09
χ2	**23.29**	**32.06**	**5.66**	**4.81**

3.8 Anaerobically mineralised ferritin SAXS results

3.8.1 Theoretical modelling of anaerobically mineralised ferritin

Following the characterisation of aerobically mineralised ferritin by DLS SEC and TEM, SAXS was used to characterise and compare the anaerobically recombinant *Pf* ferritin and the commercially available Hsf. Recombinant apo-ferritin and the horse spleen equivalent alongside two mineralised ratios, 120 atoms and 600 atoms, were purified and identified as homogenous using SEC, DLS and TEM (Section 2.9). The selected samples were further analysed using the same SAXS protocol on the BL21 beamline at Diamond Light Source in line with the SAXS analysis workflow (Figure 3.5). The samples were purified by in-line HPLC prior to measurement, both to improve sample homogeneity and to allow for background subtraction.

There was a clear peak on the HPLC plot just after 1.5 ml, the main peak was seen at 1.57 ml for all three recombinant ferritin samples (apoPf, Pf120 and Pf600). A consistent Rg across the peak was indicative of sample quality and gave confidence in the merging of scattering data. The distinct fringes characteristic of a hollow sphere can be seen in the scattering curve for apoPf (Figure 3.28). These fringes become less distinct with an increase in iron loading ratios for Pf120 (Figure 3.30) and Pf600 (Figure 3.32). There was similarity in the scattering curves at low q for all three samples. This, coupled with the HPLC plot, is an indication of particle size homogeneity across the mineralisation ratios. However, at higher q there was much less definition for Pf120 and Pf600. Considering the P(r), apoPf displays a skewed distribution towards a higher particle Rg (85 Å) which becomes much more evenly distributed around 65 Å for Pf120 and 60 Å for Pf600, consistent with the aerobically loaded ferritin SAXS data from Section 3.7. Considering the Kratky analysis for each sample, there is a clear peak identifying the presence of globular folded particles, with multidomain peaks corresponding to the fringes seen in the scattering curve. However, with the Kratky analysis of Pf600, (Figure 3.28D) the scattering curve is much more indistinct with a lot of noise at higher q regions masking the expected fringes, this was not seen with the aerobically mineralised samples previously.

Sample	q x Rg Guinier limits		I(0) Reci (Å)	I(0) Real (Å)	Rg Reci (Å)	Rg real (Å)	*r* average (Å)	*D*max (Å)	X^2
apoPf	0.3174	1.291	2.98E-01	3.00E-01	52.22	54.9	69.6	127	0.1
Pf120	0.1854	1.2997	1.05E-01	1.09E-01	50.74	54.83	67.2	126.5	0.09
Pf600	0.1787	1.2994	2.85E-02	2.67E-02	47.96	52.89	62.6	127.5	0.5
apoHsf	0.2418	1.2987	1.47E-02	1.25E-02	43.26	44.57	56.2	120	0.09
Hsf120	0.2766	1.2966	5.94E-02	5.79E-02	40.11	40.78	52.2	120	0.09
Hsf600	0.1673	1.2891	4.25E-02	4.01E-02	39.93	40.91	51.9	120	0.05

Table 3-5 Small angle X-ray scattering size parameters for anaerobically loaded ferritin

SAXS size parameters as described by ScÅtter, Reciprocal data (Reci) calculated from the Guinier approximation compared with real space (real) calculated from P(r) distribution

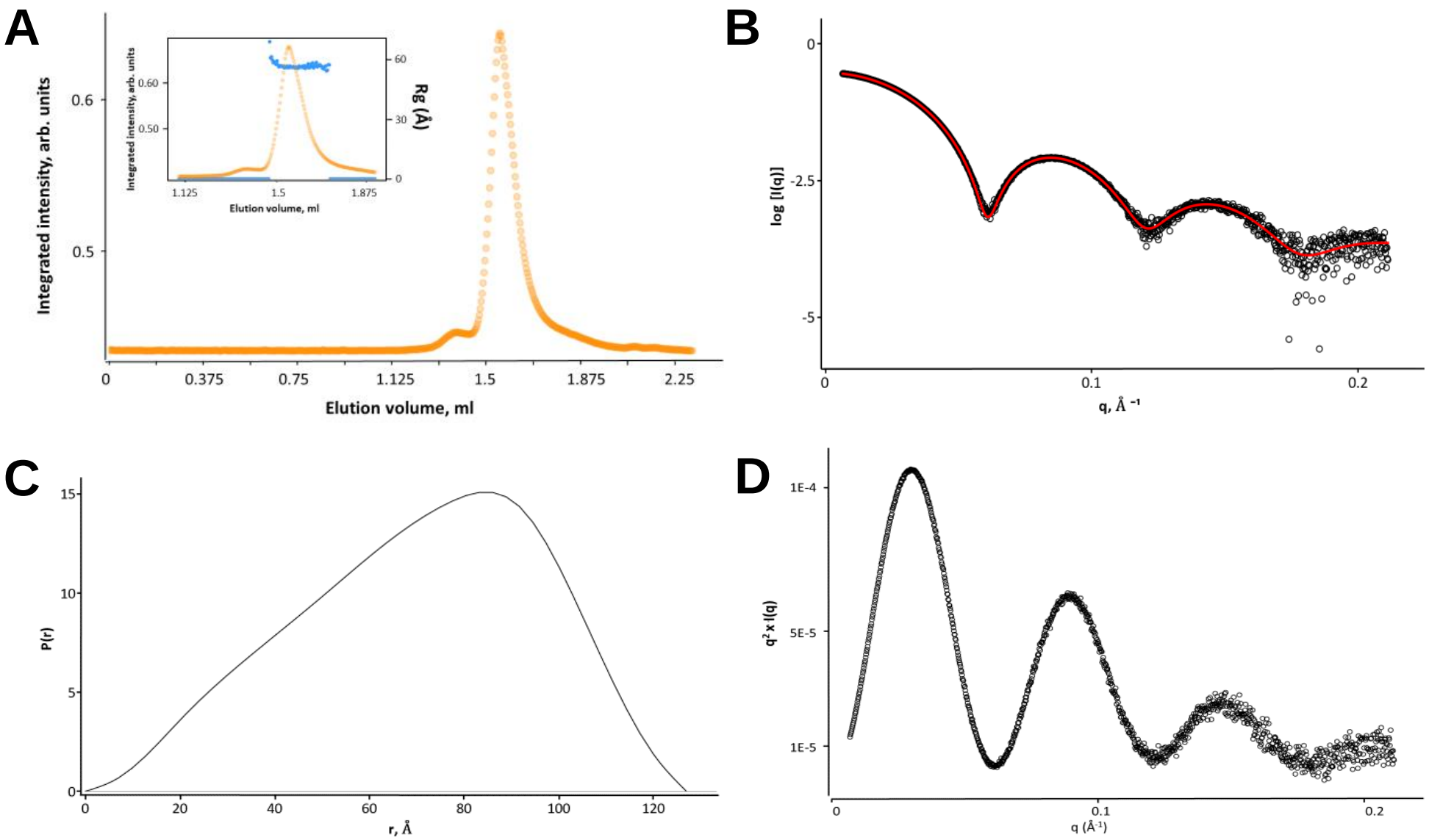

Figure 3.27 Small angle X-ray scattering analysis of recombinant apoPf

(A) HPLC plot with peak at 1.57 ml. (Inset) Rg across elution peak (B) Scatter intensity curve (black) fit to the P(r) analysis (red) (C) P(r) model histogram, showing Dmax. (D) Kratky plot

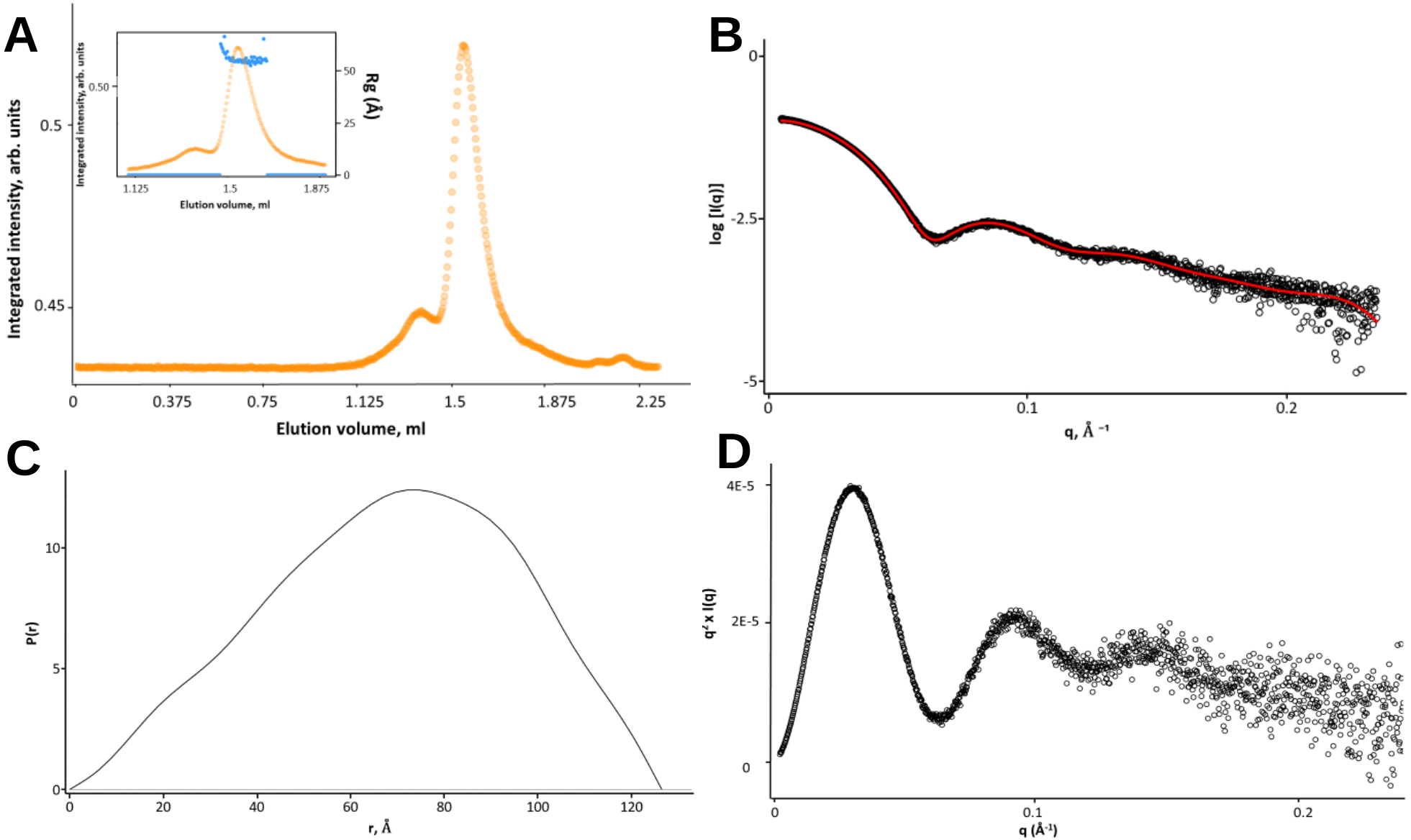

Figure 3.29 Small angle X-ray scattering analysis of recombinant Pf120

(A) HPLC plot with peak at 1.57 ml. (Inset) Rg across elution peak (B) Scatter intensity curve (black) fit to the P(r) analysis (red) (C) P(r) model histogram, showing Dmax. (D) Kratky plot

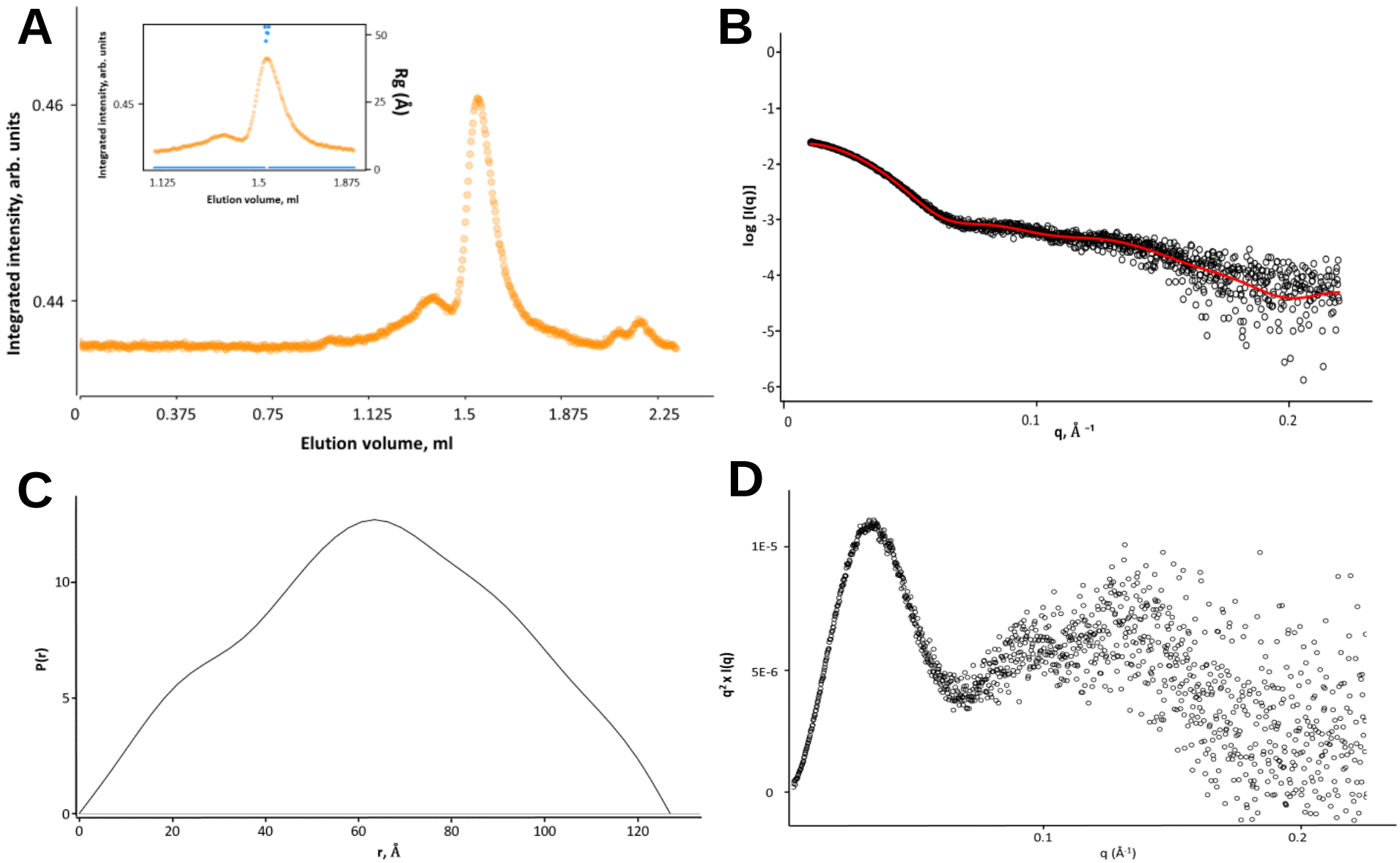

Figure 3.31 Small angle X-ray scattering analysis of recombinant Pf600

(A) HPLC plot with peak at 1.57 ml. (Inset) Rg across elution peak (B) Scatter intensity curve (black) fit to the P(r) analysis (red) (C) P(r) model histogram, showing Dmax. (D) Kratky plot

Identical analysis was performed on the commercially available horse spleen ferritin, with apoHsf receiving no mineralisation, Hsf120 was mineralised with 120 iron atoms per ferritin cage and Hsf600 mineralised with 600 iron atoms per cage. However, from the ICP-OES data in Section 2.9 there is evidence to suggest that these iron concentrations are incorrect, as the apo-Hsf already contained a significant amount of iron prior to mineralisation. However, for the sake of nomenclature they will be referred apoHsf, Hsf120 and Hsf600.

Again, the scattering data were deemed suitable for analysis, with a consistent Rg across the peaks on the HPLC signal plot. There were clear peaks at 1.57 ml for all three samples, consistent with ferritin in previous SAXS analysis.

With the apoHsf scattering curve, Figure 3.34, there is a pattern but the data lack the distinct fringes seen in previous recombinant apoPf scattering curves and described in previous work by Fischbach et al. [81]. This could be explained by the increased pre mineralisation concentration of iron identified by ICP-OES. In the characterisation by Fischbach, the native Hsf was stripped of iron using an oxygen free acetate buffer. This scattering pattern follows a similar shape at lower q regions seen for Hsf120, Figure 3.36, and for Hsf600, Figure 3.38. However, in the latter there is less distinction to the curve with noise at higher q regions. Considering the P(r), the apoHsf data begin with a slight skewing towards smaller particle Rg of 45 Å, this is maintained through the iron loading concentrations.

Furthermore, the Kratky plots for all three samples display a peak that converges towards the q axis, thus supporting evidence of globular folded proteins. With the higher iron loading Hsf600, seen with Figure 3.38D, there is noise at higher q resulting in the loss of curve quality.

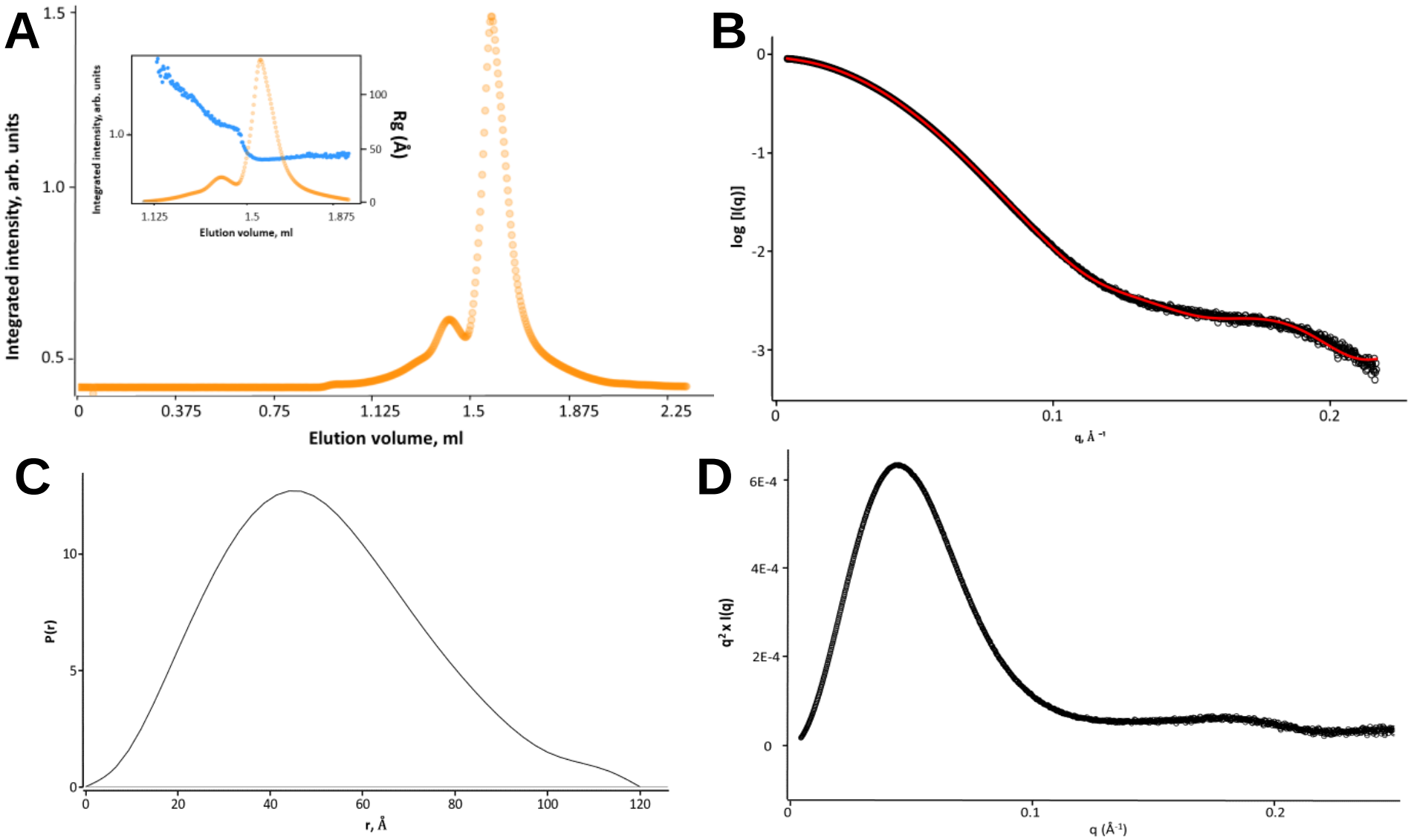

Figure 3.33 Small angle X-ray scattering analysis of apoHsf

(A) HPLC plot with peak at 1.57 ml. (Inset) Rg across elution peak (B) Scatter intensity curve (black) fit to the P(r) analysis (red) (C) P(r) model histogram, showing Dmax. (D) Kratky plot

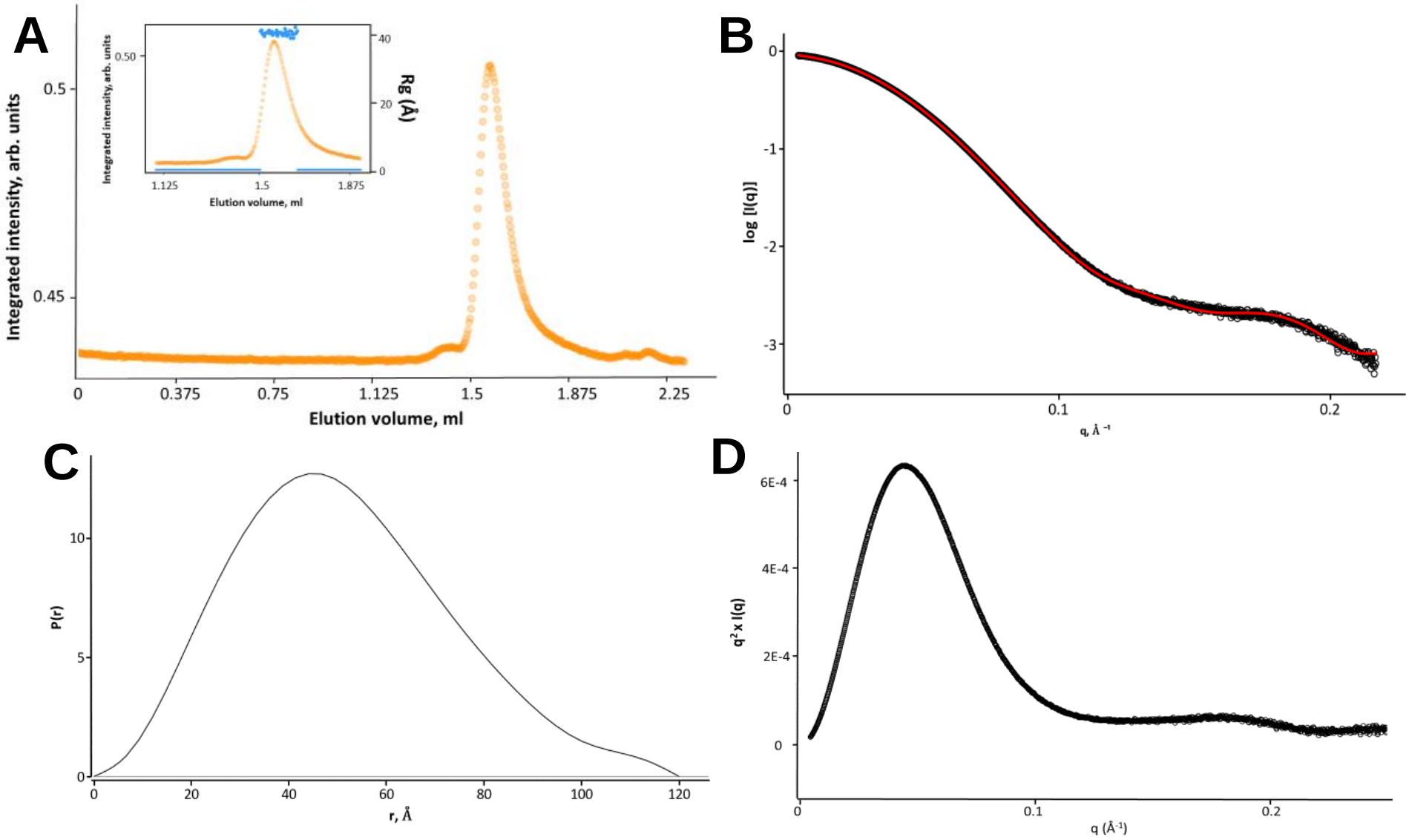

Figure 3.35 Small angle X-ray scattering analysis of Hsf120

(A) HPLC plot with peak at 1.57 ml. (Inset) Rg across elution peak (B) Scatter intensity curve (black) fit to the P(r) analysis (red) (C) P(r) model histogram, showing Dmax. (D) Kratky plot

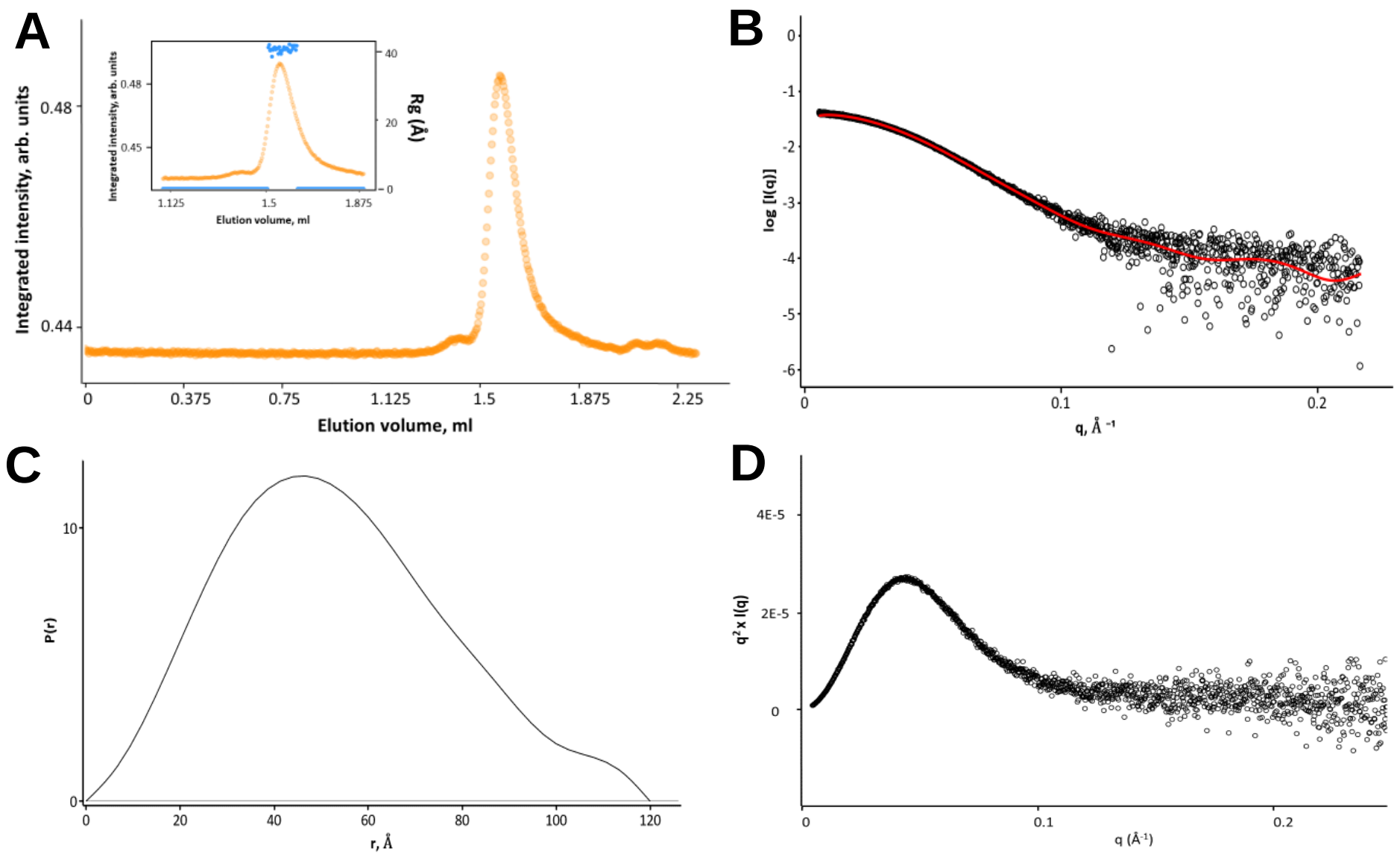

Figure 3.37 Small angle X-ray scattering analysis of Hsf600

(A) HPLC plot with peak at 1.57 ml. (Inset) Rg across elution peak (B) Scatter intensity curve (black) fit to the P(r) analysis (red) (C) P(r) model histogram, showing Dmax. (D) Kratky plot

3.8.2 Envelope modelling of anaerobically mineralised ferritin

To visually perceive how particle polydispersity and sample homogeneity are influenced by iron mineralisation, dummy atom models of the particles were constructed from the P(r). Both recombinant *Pf* ferritin and commercially available Hsf were compared to better understand the relationship between the scattering data and iron mineralisation ratio. As with the previous envelope modelling, DAMMIN/F from the ATSAS suite was used to run the dummy atom annealing resulting in an envelope dummy atom model (DAM).

As with the modelling of aerobically mineralised ferritin, there is a loss of spherical homogeneity as iron mineralisation concentration increased, Figure 3.39, with apoPf containing very low traces of iron, as indicated in the ICP-OES analysis, the model generated indicates a spherical particle. The models becomes more disorganised as iron mineralisation concentration increases, with the iron oxide contributing to the scattering pattern. The DAM generated for apoHsf is a disorganised globular particle, with the model becoming more disorganised for Hsf120, and ultimately the Hsf600 model takes a more compact and ellipsoid shape. By itself, the DAM modelling suggests that, as iron concentration increases, the ferritin particle becomes non-spherical. However, when compared with the TEM analysis, there is evidence towards the particles maintaining their shape despite increasing iron concentrations. Combined these characterisations allow for the rationale of these model being a representation of heterogenous electron dense core rather than the electron lucent protein shell.

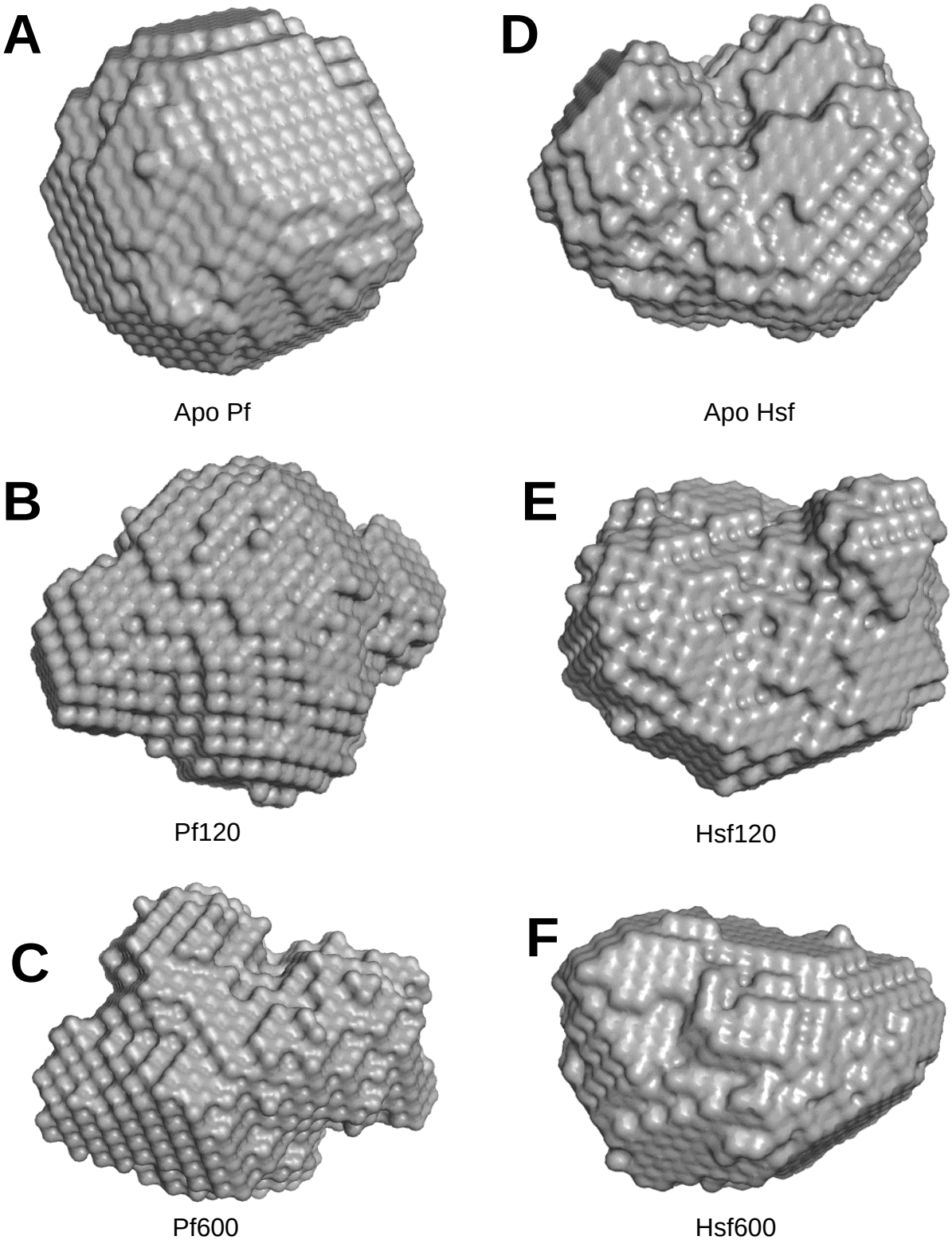

Figure 3.39 *Ab initio* dummy atom bead models of anaerobically mineralised ferritin

Ab initio bead models generated using the DAMMIN/F from the ATSAS suite, data represented in surface envelopes presented in PYMOL (A) ApoPf (B) Pf120 (C) Pf600 (D) ApoHsf (E) Hsf120 (F) Hsf600

3.8.3 Form factor modelling of anaerobic mineralised ferritin

Sasview software was utilised to fit mathematical models to the scattering data for the anaerobically mineralised ferritins to understand how the iron core reconstitutes within the particle. Size parameters were adjusted on the user interface and fitting validation plots were tested against experimental scattering data to provide a chi-squared result as an indication of fitting accuracy. After their apparent suitability in previous model fitting, core-shell models and multi-shell models were fit to the normalised scattering data in line with the analysis workflow, Figure 3.5. For improved chi-squared value, a Schulz PDR was allowed to fit the particle size parameters which are reported in Table 3-6. The normalised apoPf scattering data was fit with a core shell model to a satisfactory chi-squared value of 2.4 and a total particle radius of 65.57 Å, Figure 3.40A. A polydispersity ratio of 0.04 was applied to core radius of particle. The resulting SLD and radius parameters were similar to those seen with previous apoPf modelling, this supported a goodness of fit and demonstrated reproducibility.

Core-shell models were fit to anaerobically mineralised *Pf*120 scattering data resulting in a chi-squared value of 50.24 and total particle radius of 68.30 Å. With such an increased chi-squared value it was appropriate to fit PDRs to the model, with a Schulz PDR of 0.16 applied to the core radius. This returned an improved chi-squared of 2.77 and a total particle radius of 54.79 Å. Similarly, a multi-shell model was applied to the normalised Pf120 experiment data returning a chi-squared value of 21.70 and a total radius of 61.45. When a Schulz PDR of 0.17 was fit the core radius this returned a chi-square value of 2.45 and a particle radius of 58.03 Å.

Considering the normalised Pf600 scattering data, Figure 3.40D, a core shell fitting of the data returned a chi-squared of 7.45 and a total particle radius of 57.78 Å, when PDRs of 0.17 and 0.05 were applied to the core and outer shell respectively. Furthermore, a multi-shell model returned a chi-squared value of 2.66 and total radius of 86.41 Å, when a PDR of 0.37 was applied to the core radius and a PDR of 0.15 was applied the outer shell. Outer shell parameters were similar to solvent in this fitting, possibly misrepresenting the actual size of particle.

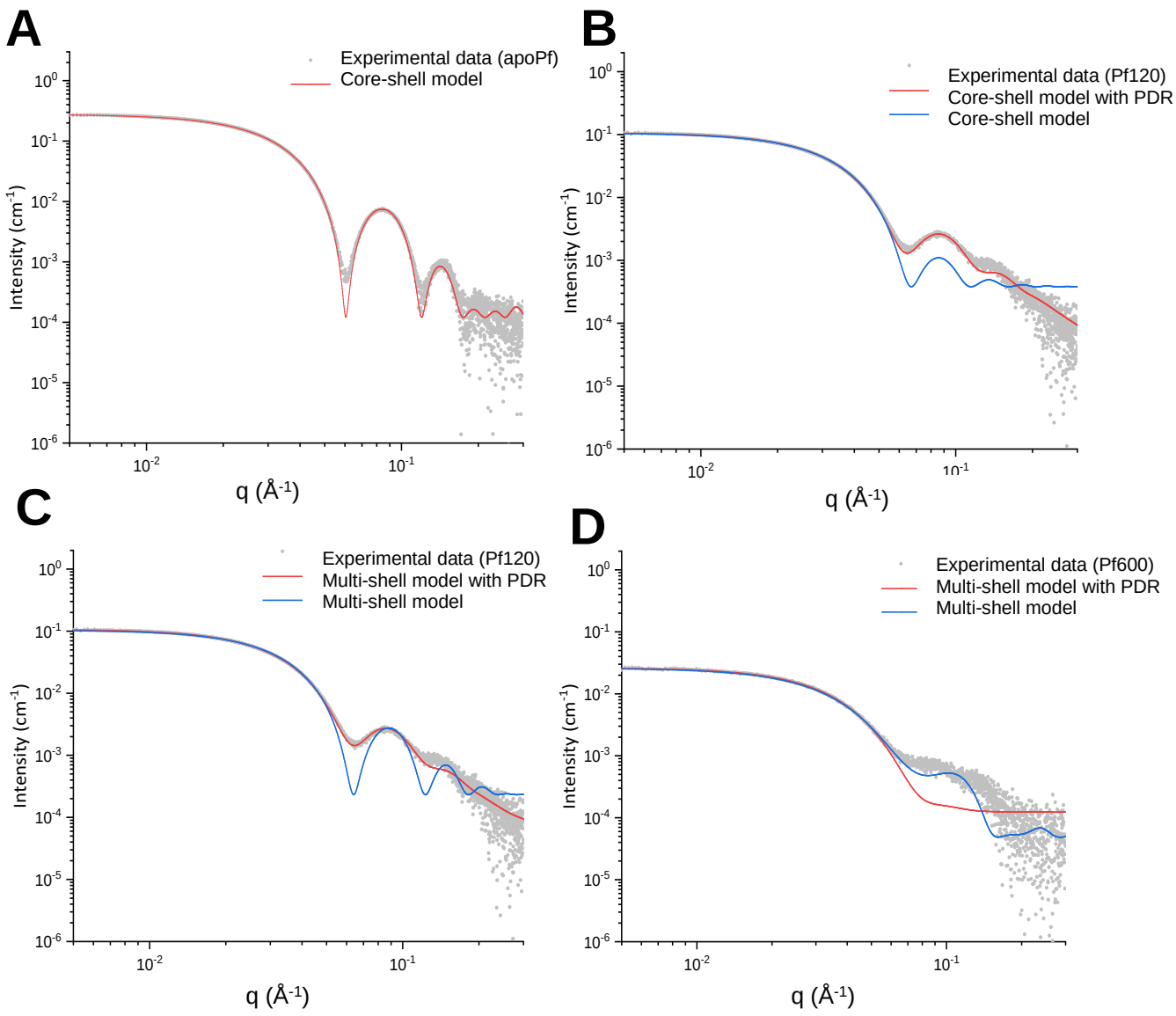

Figure 3.40 Form factor fitting for anaerobically mineralised *Pf* ferritin

Form factor fitting on normalised *Pf* ferritin scattering data (A) core-shell fitting (red) of apoPf returned a chi-squared 2.4 and total particle radius of 65.57 Å.
(B) Core-shell fitting with a PDR applied (red) returned a chi-squared of 2.77 and total radius of 54.79 Å. PD of 0.16 applied to core radius. Core-shell fitting of Pf120 with no polydispersity PD applied(blue), with a chi-squared of 50.24 and a particle radius of 68.30 Å. (C) Multi-shell fitting of 120 with PD (red) returning a chi-squared of 2.45 and total particle radius of 58.03 Å. Core radius PD of 0.04 and outer-shell PD of 0.01 applied to the fitting parameters. Core radius with no PD (blue) returned a chi-squared of 21.70 with a total radius of 61.45 Å (D) fitting of Pf600, core-shell fitting (red) returning chi-squared of 7.45 and particle radius of 57.78 Å. Multi-shell fitting (blue) returning chi-squared of 2.66 and total radius of 86.41 Å

Continuing with the particle characterisation, core-shell and multi-shell models were applied to normalised Hsf scattering data, Figure 3.41, with the fitting values described in Table 3-6. Considering the apoHsf sample, a core-shell fitting returned a total particle radius of 78.39 Å and a chi-squared value of 1.53. A multi-shell fitting of this scattering data reported a total radius of 72.01 Å and a chi-squared value of 1.21. A Schulz PDR was applied to the individual parameters, but this had a negligible effect on the chi-squared accuracy.

A core-shell model was applied to the Hsf120 normalised data resulting in a total particle radius of 73.29 Å and a chi-squared of 2.14. The multi-shell fitting returned a chi-squared value of 3.16 with a total particle radius of 77.25 Å. A core-shell model was applied to the Hsf600 normalised data resulting in a total particle radius of 67.52 Å and a chi-squared value of 1.30. The multi-shell fitting returned a chi-squared of 1.36 with a total particle radius of 76.41 Å. Polydispersity distributions were not applied to these model fittings as it did not affect the chi-squared accuracy.

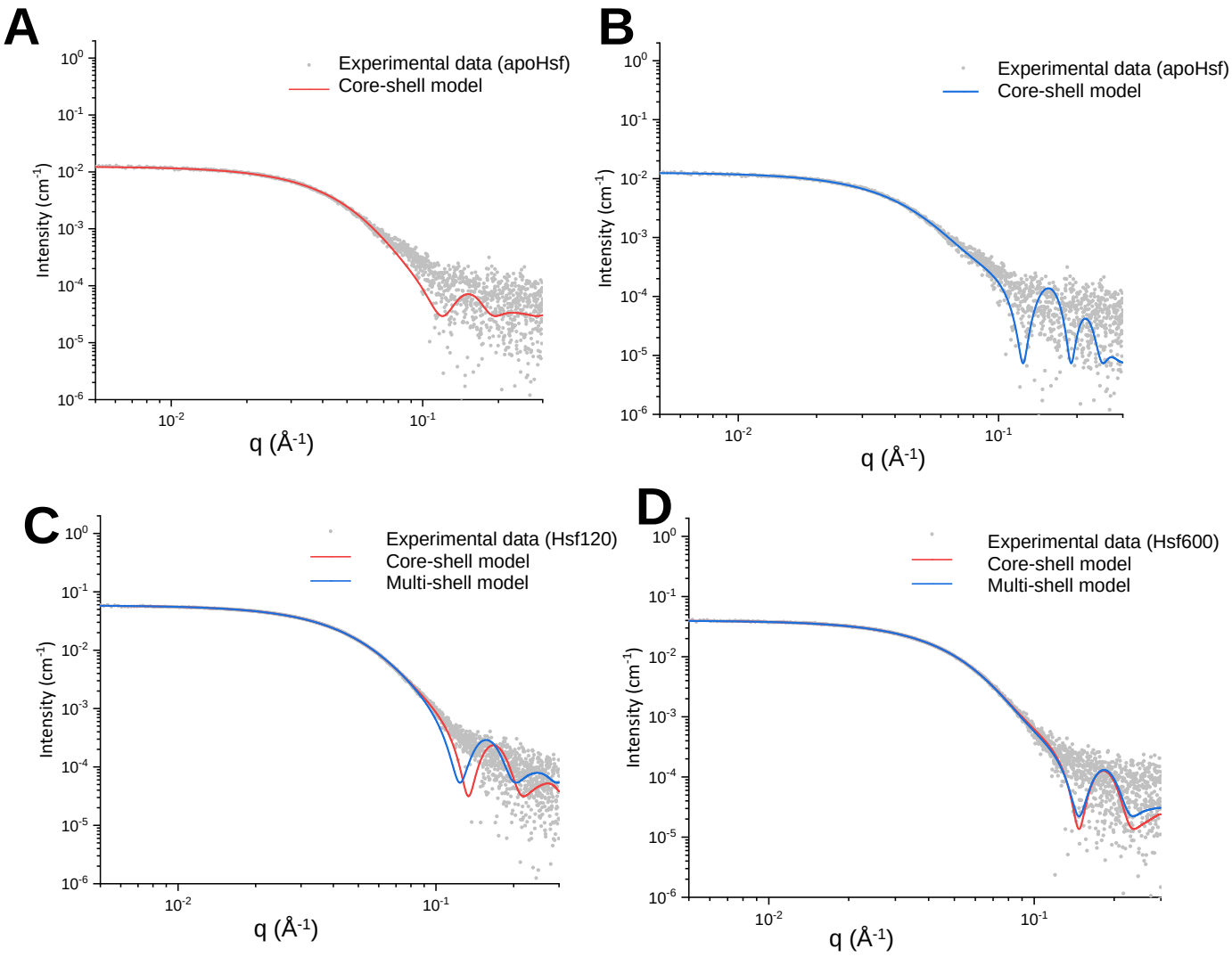

Figure 3.41 Form factor fitting for anaerobically mineralised Hsf ferritin

Form factor fitting on normalised Hsf ferritin scattering data (A) Core-shell fitting (red) of apoHsf returned a chi-squared 1.21 and total particle radius of 78.39 Å. (B) Multi-shell fitting (blue) returned a chi-squared of 1.21 with a total particle radius of 72.01 Å (C) Core-shell fitting of Hsf120 (red) returning a chi-squared of 2.14 and total particle radius of 73.29 Å. Multi-shell fitting (blue) returned a chi-squared of 3.16 with a particle radius of 77.25 Å. (D) Core-shell fitting of Hsf600 (red) returning chi-squared of 1.30 and particle radius of 67.52 Å. Multi-shell fitting of Hsf600 (blue) returning chi-squared 1.36 and total radius of 76.41 Å.

Parameter	ApoPf core	Pf120 core	Pf120 multi	P600 core	Pf600 multi	ApoHsf core	ApoHsf multi	Hsf120 core	Hsf120 multi	Hsf600 core	Hsf600 multi
Background (cm^{-1})	1.0e-4 ±1.6e-6	4.1e-5 ±1.5e-6	7.2e-5 ±1.5e-6	1.0e-4 ±1.5e-6	4.87e-5 ±1.7e-6	2.93e-5 ±1.55e-6	7.37e-6 ±1.6e-6	3.1e-4 ±1.6e-6	5.4e-5 ±1.6e-6	1.28e-5 ±1.9e-6	2.2e-5 ±1.7e-6
Core radius (Å)	35.13 ±0.005	43.08 ±0.01	39.80 ±0.01	37.91 ±0.02	26.20 ±0.03	38.89 ±0.05	39.69 ±0.06	34.65 ±0.003	37.20 ±0.01	31.66 ±0.02	31.81 ±0.001
Thickness 1 (Å)	30.44 ±0.007	11.71 ±0.23	13.60 ±0.01	19.87 ±0.03	50.12 ±0.03	39.5 ±0.05	20.00 ±0.06	38.64 ±0.01	33.38 ±0.01	35.86 ±0.07	34.59 ±0.018
Thickness 2 (Å)			4.65 ±0.03		10.09 ±0.03		12.40 ±0.05		6.67 ±0.32		10.01 ±0.01
SLD core ($10^{-6}Å^{-2}$)	9.44 ±3.6e-4	9.53 ±1.3e-4	9.54 ±0.001	20.96 ±0.008	33.10 ±0.07	17.14 ±0.02	11.31 ±0.004	16.32 ±0.001	20.25 ±0.006	21.35 ±0.01	26.50 ±0.005
SLD T1 ($10^{-6}Å^{-2}$)	10.61 ±2.0e-4	10.51 ±1.6e-4	10.92 ±0.001	14.88 ±0.004	11.46 ±0.001	10.08 ±0.001	9.24 ±0.002	9.89 ±0.003	10.02 ±8.0e-4	10.52 ±0.009	11.03 ±0.001
SLD T2 ($10^{-6}Å^{-2}$)			10.08 ±0.001		9.56 ±0.006		9.84 ±0.001		10.03 ±0.03		9.40 0.002
SLD solvent ($10^{-6}Å^{-2}$	9.43 ±8.0e-5	9.43 ±7.4e-5	9.43 ±3.0e-5	9.43 ±0.002	9.43 ±0.001	9.43 ±0.001	9.43 ±3.0e-4	9.43 2.0e-4	9.43 ±0.001	9.43 6.0e-4	9.36 ±7.5e-4
Total Radius (Å)	65.57	54.79	58.03	57.78	86.41	78.39	72.01	73.29	77.25	67.52	76.41
χ2	2.40	2.77	2.45	7.45	2.66	1.53	1.21	2.14	3.16	1.30	1.36

Table 3-6 Form factor fitting parameters for anaerobically loaded ferritins

3.9 Discussion

Particle polydispersity, size and structure characterisation was facilitated by SAXS analysis techniques. These included theoretical data analysis, *ab initio* dummy atom bead models generated from P(r), and form factor modelling, which compared the experimental data to mathematical models. The aerobically mineralised *Pf* samples were compared with anaerobically mineralised *Pf* and commercially available Hsf samples.

The scattering curve, P(r) distribution and Kratky plots were reproducible between the two mineralisation methods, with the characteristic fringes seen at lower iron concentrations being lost due to the loss of hollow sphere as increased iron concentrations populate the core. There was evidence of noise at higher q values seen in the data for the anaerobically mineralised samples, which could be attributed to particle aggregation or inaccurate background subtraction. However, Guinier and Kratky analysis provided strong evidence of low particle polydispersity and was supported by previous characterisations using TEM, SEC and DLS. Consequently, this higher noise might be attributed to the iron distribution within the particle core being non-uniform, rather than a polydisperse ferritin sample. Considering the anaerobically mineralised samples there is evidence for forcing the Dmax to 120 Å, perhaps a higher Dmax may have fit the experimental data better. However, when fitting P(r) there is a trade off between smooth distribution (no undulations in the peak) against the peak approaching P(r) = 0 at Dmax.

The change in P(r) distribution as iron loading ratio increases is most significant, as TEM and DLS analysis indicate a maintenance of particle size as iron loading ratio increases. In contrast the P(r) radius distributions skew to smaller values of r as the iron core is reconstituted. This is further supported by the P(r) of the mineralised Hsf, with increased mineralisation concentrations evident via ICP-OES. This scattering behaviour can only be attributed to the particle's electron dense core dominating the scattering of the electron lucent protein shell. Unfortunately, the SLD of the core and increase in iron concentrations were not relative. At such experimental wavelengths the total absorption cross section for iron is 94.36 cm^2 g^{-1}, compared to the value of 1.20 cm^2 g^{-1} for carbon [51], [84].

The apoPf form factor fitting was reproducible and justified the use of the core model. In contrast, the form factor fitting of Pf120 and Pf600 was more complicated, as form it assumes a homogenous distribution and low polydispersity across the samples. However, it is likely that iron oxide is arranged heterogeneously within the particle core. There is clear evidence from the loss of distinct fringes that iron is reconstituting in the core but the higher scattering length density of iron is obscuring the scattering of the protein shell. As a result, the multi-shell modelling of the outer shell, thickness and SLD was arbitrary, and had little impact on accuracy of fitting. Perhaps a different fitting model may have been appropriate to determine these parameters better.

Form factor fitting for mineralised *Pf* ferritin was reproducible when PDR were applied to the fitting retuning accurately similar SLD and radius measurements of particle core and shell thickness. The multi-shell fitting for Pf120 best describes a heterogenous distribution of iron within the outer shells, reflected by the increased t1 SLD in relation to core SLD. This could be characterised by iron building up on ferroxidase sites at iron channels along the inner surface of the protein shell, before being displaced into the core centre. Conversely, considering the Pf600 modelling, a core-shell model can be characterised by the presence of a reconstituted iron oxide core growing within the particle, with higher SLD modelled for the core compared with the outer shells.

Considering the apoHsf, the scattering clearly demonstrates the presence of iron prior to any particle mineralisation. This was reflected in the modelling, explained by a higher core SLD in relation to outer shell SLD. ICP-OES analysis of the Hsf indicates that there are up to 552 iron atoms per apoHsf particle, 830 atoms per Hsf120 particle and 1168 atoms per Hsf600 particle, with is better reflected by the core shell modelling, with iron displaced from the ferroxidase into the cavity centre.

There was clear evidence for the reconstitution of a controllable iron core inside the *Pyrococcus* ferritin core, with P(r) distributions, bead models and form factor fitting models changing incrementally as mineralisation concentrations increased. However, without the DLS and TEM data from previous characterisations providing evidence for the presence and polydispersity ferritin molecules, the polydispersity and homogeneity of the ferritin particles would be under question. The combined characterisations allow

the interpretation DAM as the electron dense core over scattering the electron lucent protein shell.

Chapter 4 Functionalisation of ferritin particle

4.1 Introduction

The previous chapters have demonstrated the synthesis and successful mineralisation of recombinant *Pf* ferritin nanoparticles. Advanced SAXS characterisation alongside SEC, TEM and DLS characterisation suggests that the particles remain homogenous and monodisperse after mineralisation which is suitable for downstream particle functionalisation. This chapter looks to explore the relationship between iron loading concentration and magnetic susceptibility, and the subsequent functionalisation of the magnetic nanoparticles with positive surface charge for non-specific electrostatic bacterial adhesion.

Through ICP-OES analysis, it is evident that the mineralisation concentration ratio (iron atoms per particle) of *Pf* ferritin can be tuneable with a controlled concentration of iron reconstituted within the particle core. However, without magnetic susceptibility testing it is unclear how this can affect the superparamagnetic properties of the particles. High powered magnetic susceptibility testing using a super conducting interference device can provide evidence towards this, relating magnetic susceptibility tuning with mineralisation concentration.

Parker et al. [42] have demonstrated the synthesis of superparamagnetic nanoparticles from recombinant *Pf* ferritin particles, although this work did not consider the functionalisation of such particles. On the other hand Carreira *et al.* [66] have shown that commercially available horse spleen ferritin particles mineralised with cobalt-doped iron oxide display superparamagnetic properties. These particles, once cationised, were able to electrostatically adhere to bacterial surfaces allowing the capture of bacteria out of solution. However, neither investigation attempted to control the iron concentration in the particle.

In the Hsf functionalisation studies, the mineralised ferritin samples were cationised in a one-pot synthesis reaction, whereby negatively charged amino acid residues on the protein surface were labelled with positively charged DMPA. This facilitated the labelling of the bacterial cells, and subsequent concentration of the bacterial cells from solution. Following this protocol, recombinant *Pf* ferritin samples were cationised and

characterised using DLS and zeta potentiometry, a procedure which has not been utilised before for recombinant ferritin.

4.2 Methods and materials

4.3 Superconducting interference magnetometry

Theory

In order to measure the magnetic parameters of the mineralised *Pf* nanoparticles, a super conducting quantum interference device (SQUID) magnetometer was utilised. SQUID refers to the superconducting interference device used to measure the DC magnetic moment, in relation to magnetic field and temperature. As shown in Figure 4.1, a sample is passed through an applied magnetic field, the pick-up coils are connected to a detector loop with parallel Josephson junctions [17]. Magnetic flux from the sample interferes with the super conducting loop and is measured as voltage. SQUID was chosen for its ability to identify small magnetic moments down to 10-11 Am^2. Furthermore, the magnetometer can drop the temperature of the sample below 10 K, at such temperatures the blocking temperature can be accurately measured [85].

Method

100 µl samples aliquots were loaded into Agar capsules (Agar Scientific Ltd, UK). The capsule was then frozen in liquid nitrogen and loaded onto a plastic straw sample holder on the end of an insertion rod. The insertion rod and sample were loaded into the SQUID magnetometer (Magnetic Property Measurement System, MPMS, Quantum Design, USA). Field sweep measurements over ±2 Tesla, at 250 K allowed for magnetic susceptibility testing. Mass magnetisation was calculated after a background subtraction.

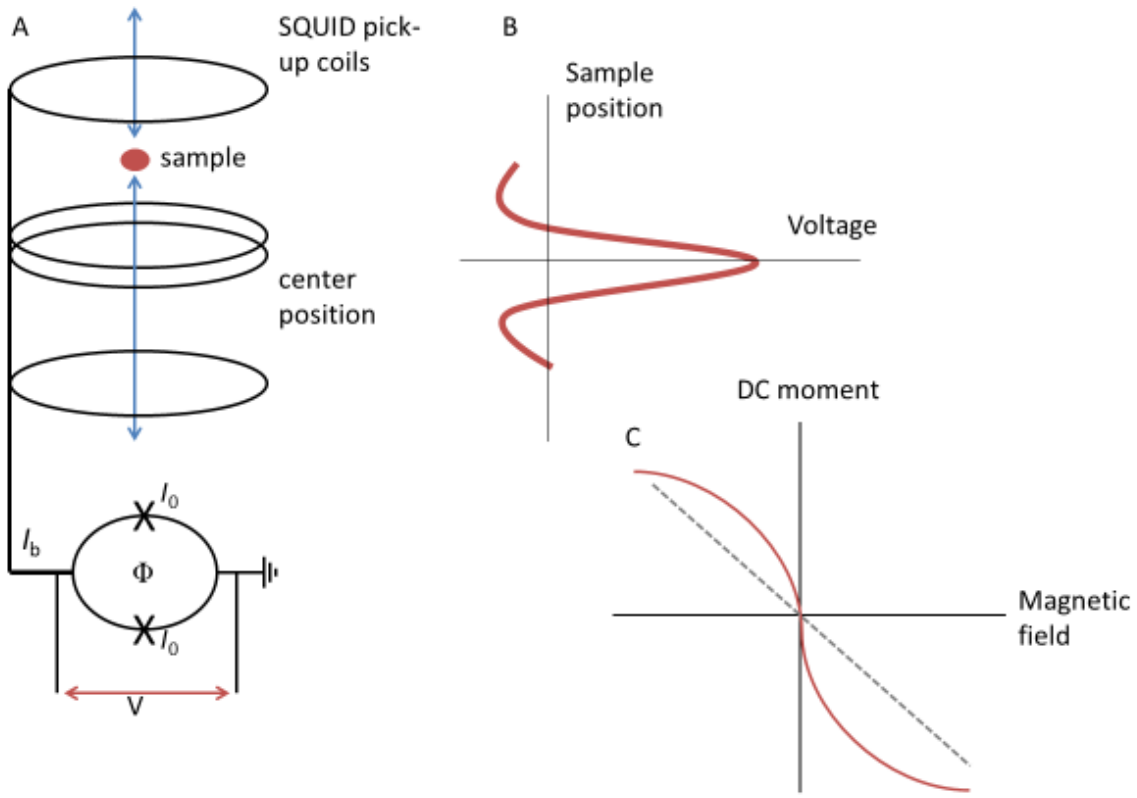

Figure 4.1 Schematic of magnetic susceptibility measurement using SQUID

(A) A sample is moved through SQUID pick up coils, the flux interference is converted into voltage, the signal of which is measured by a detector. (B) association between sample position and voltage measurement. (C) Magnetic susceptibility plotted as DC moment in relation to magnetic field, superparamagnetic (red) particles demonstrate specific hysteresis and diamagnetic buffer background (grey) shows no magnetic susceptibility, background subtracted from measurements.

4.4 Cationisation of ferritin

Theory

The presence of aspartic and glutamic residues on the ferritin outer surface provide the particle with an overall negative charge. A simple one-pot reaction first described by Danon et al. [86] chemically cationises the negative residues with the positively charged DMPA (Figure 4.2). The reaction is facilitated by the presence of N-(3-dimethylaminopropyl)-N-ethylcarbodiimide hydrochloride (EDC), which activates the carboxyl group on the negative protein residues. By forming an active O-acylisourea ester, the nucleophilic primary amine group on DMPA is then able to crosslink with the activated carboxyl with an isourea by-product being released. The second amine group of the DMPA is naturally positive allowing for the electrostatic attraction to bacterial surfaces [87].

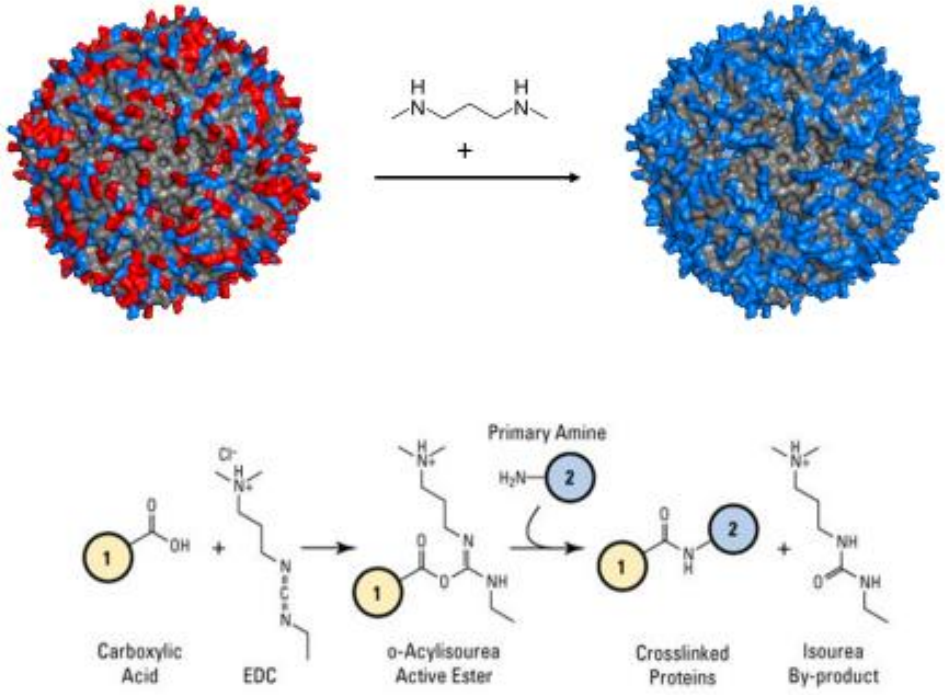

Figure 4.2 Cationisation of ferritin

(A) Schematic of conversion from overall negative charged particle to positive charged particle. *Pf* ferritin with positive charged residues in blue (Lys, His, Arg) and negatively charged particle in red (Asp, Glu). Crosslinking of DMPA results in negative residues conveying a positive charge. PBD ID 2X17.
(B) Schematic example of EDC coupling reaction, with active ester intermediate formed by addition of EDC, allowing the DMPA primary amine nucleophilic attack, with permissions 2017 Thermo Fisher Scientific Inc. All rights reserved.

Method

Solutions of DMPA were made from 374 mg powdered form dissolved in 200 mM 2-(N-morpholino) ethanesulfonic acid (MES) buffer and adjusted to pH 7 using HCl. Ferritin aliquots were added to the DMPA solution, to make a protein concentration of 2 $mg.ml^{-1}$ and solutions stirred continuously for 3 hours at 4^{o}C. After initial equilibration, the pH was adjusted to pH 5 and EDC was added (141 mg per 5 ml) to initiate the coupling reaction. The solution was left to equilibrate overnight at 4^{o}C with stirring. The solution was dialysed using Medicell dialysis tubing 12–14 kDa molecular weight cut-off against HEPES buffer (pH 8.6, 0.05 M, 0.1M NaCl).

4.4.1 Zeta potentiometry

Theory

The determination of the surface charge is an important parameter in understanding the cationisation process. The surface charge of a particle induces ions to accumulate in an electrical double layer of rigid ions interacting with the particle surface and a more diffuse layer of ions in solution. Close to the particle surface ions are either absorbed or very strongly associated and remain in situ when the particle moves in response to the Brownian motion of solution. The outer most shear or slipping plane is the point at which ions are less strongly associated and free to move in solution [88]. The potential energy difference between the outermost hydrodynamic layer and the particle surface is known as the zeta potential. This is measured by passing an electrical charge across a sample and calculating the electrophoretic mobility based on the scattering of light as the particles move within a cuvette in relation to electric field, (Figure 4.3). Particle velocity (V) is proportional to electric field (E) and electrophoretic mobility (μ) is the proportionality constant [89] (Equation 4-1).

$$v = \mu E$$

Equation 4-1

The Henry equation (Equation 4-2), is used to describe the relationship between zeta potential (z) and electrophoretic mobility (μ), where ε is dielectric constant, eta potential, h is viscosity and f(ka) is the Henry function. Positive energy differences can be attributed to positive surface charge and negative energy differences with negative surface charge thus giving an indication of particle surface charge [90].

$$\mu = \frac{2\varepsilon z\, f(ka)}{3h}$$

- For particles in polar media the maximum value of f(ka) is 1.5 (Smoluchowski approximation)
- For particles in non-polar media the minimum value of f(ka) is 1 (Hückel approximation)

Equation 4-2

Method

The sample pH was determined and 5 ml aliquots were adjusted to a concentration of 1 $mg.ml^{-1}$ suspended in HEPES buffer (pH 8.6, 0.05 M, 0.1M NaCl). The samples were then desalted using a PD10 column (GE Healthcare) and passed through a 220 nm pore to remove any high intensity scattering debris. DLS was performed on a Zetasizer Nano-ZS (Malvern Instruments, UK). With a total of 12 measurements per triplicate collected. Due to the samples being in polar solution, the Smoluchowski approximation was used by the Zetasizer, in line with Equation 4-2, to calculate the zeta potential.

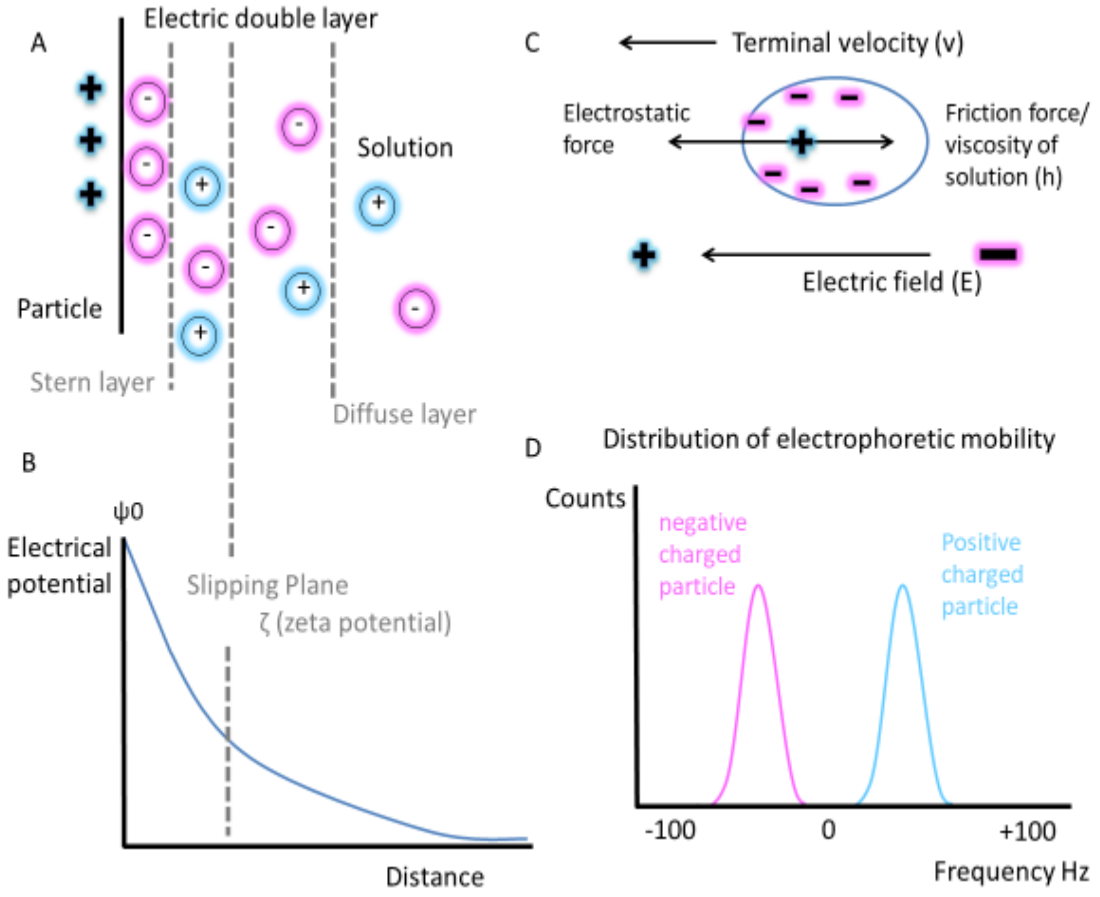

Figure 4.3 Schematic of zeta potentiometry measurement

(A) Cartoon of the electric double layer of a positive nanoparticle, strongly associated anions form the Stern layer, the slipping plane is the point at which ions become diffuse in solution, energy difference between surface and slipping plane is zeta potential (B) Electric double layer plotted as electric potential against distance (C) Electrophoresis is used to give particle electrophoretic mobility, the zeta potential is calculated using the Henry equation. (D) Electrophoretic mobility is measured in counts detected through the scattering of light, and the resulting distribution indicates the particle surface charge. Figure adapted with permissions from Kaszuba et al. Malvern Instruments ltd. Open-access article distributed under the terms of the Creative Commons Attribution License.

4.5 Results

4.6 Superconducting magnetometry analysis

To better understand how the reconstitution of a magnetic core within the nanoparticle affects magnetic susceptibility, analysis of the aerobically mineralised *Pf* ferritin was compared with the anaerobically mineralised *Pf* and Hsf. Firstly, a field sweep of ±2 Tesla was carried out on the aerobically mineralised Pf120 and Pf600 samples, Figure 4.4. After background subtraction and calculation of mass magnetisation, there is evidence to suggest that these samples were diamagnetic as their magnetic susceptibility opposed that of the magnetic field. The double line at higher magnetic field is possible evidence of background interference from the sample holder and is affecting the shape of the graph at higher magnetic field.

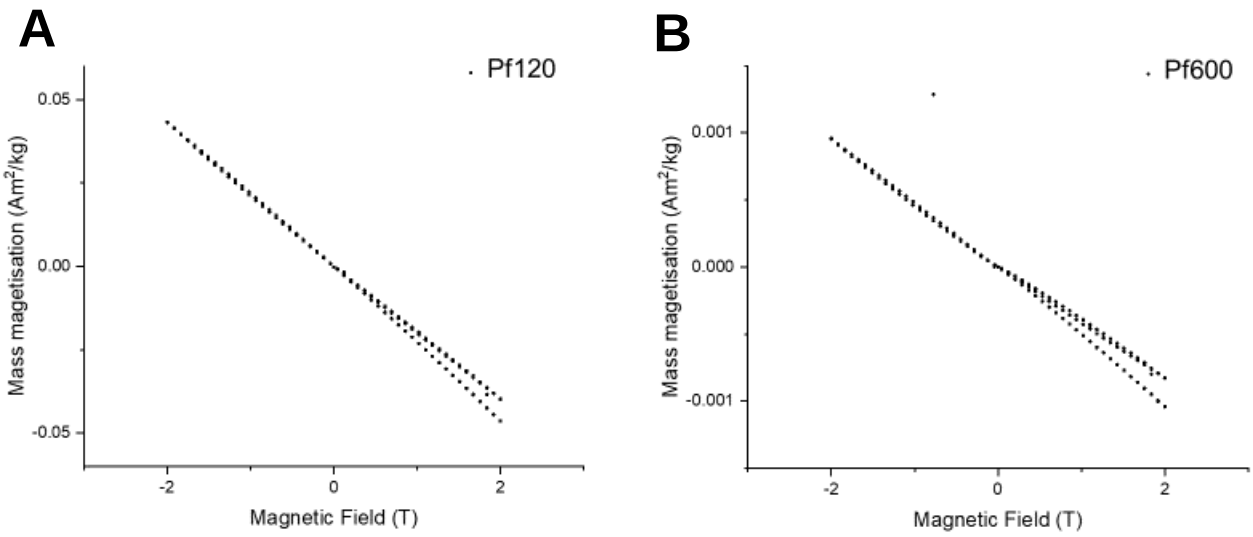

Figure 4.4 Magnetic susceptibility of aerobically loaded ferritin

Field sweep of ±2 Tesla using the MPMS3 magnetometer (A) magnetic susceptibility of aerobically loaded Pf120 and (B) aerobically loaded Pf600

Secondly, the magnetic susceptibility of the anaerobically mineralised samples was tested with a field sweep of ±0.5 Tesla. This included Pf120, Pf600, Hsf120 and Hsf600, Figure 4.5. In contrast to the aerobically mineralised samples, there is evidence to suggest that the anaerobically mineralised samples were paramagnetic as the magnetic susceptibility was weak and proportionally aligned in parallel to the direction of applied field. However, the samples did not display the characteristic hysteresis expected of a super paramagnetic particle and it is possible that a field sweep of 0.5 Tesla was of insufficient scale to detect the superparamagnetic qualities of the particles. Evidence of *Pf* ferritin anaerobically mineralised with 1000 iron atoms per particle by Parker et al.[42] showed rapid saturation at fields 2.0-4.0 T.

In Figure 4.5 there is slight curvature of the data, an indication that this sample may have superparamagnetic properties, however at such low field sweep this is inconclusive. Similar to the data obtained for the aerobic loading, there is evidence of background interference from the measurements, this could be explained by the diamagnetic sample holder skewing the data. It is possible such interference could be characterised as the sample moving in the sample holder or debris on the inside of the measurement housing.

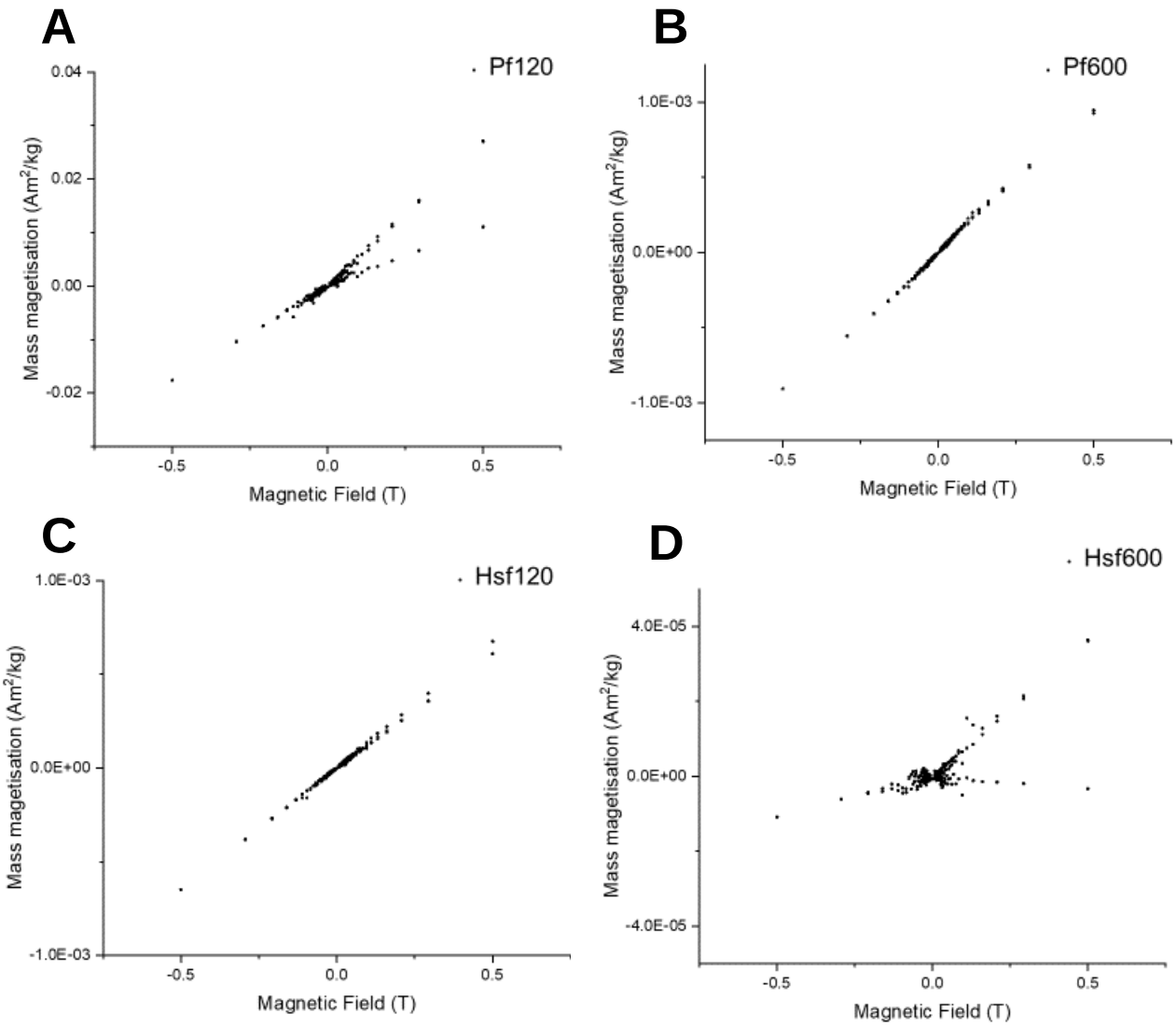

Figure 4.5 Magnetic susceptibility of anaerobically loaded ferritin

Field sweep of ±0.5 Tesla using the MPMS3 magnetometer (A) magnetic susceptibility of anaerobically loaded Pf120 (B) anaerobically loaded Pf600 (C) anaerobically loaded Hsf120 and (D) anaerobically loaded Hsf600

Due to the inadequacy of the previous ±0.5 T field sweep, a wider field sweep of ± 2.0 T was employed to better characterise the magnetic susceptibilty of the anaerobically mineralised ferritin. Figure 4.6 shows the magnetic susceptibility of the anaerobically mineralised ferritins Pf600 and Hsf600. Similar, to the data obtained in the aerobic loading, the magnetic susceptibility of these anaerobically mineralised samples opposes that of the magnetic field providing evidence of particles with diamagnetic properties. Although these are the same samples that had previously shown paramagnetism, it is possible that the time between the initial field sweep and this second field sweep may have been long enough for the iron core to reduce to Fe_2O_3 nH_2O, therefore losing magnetic susceptibility of the sample.

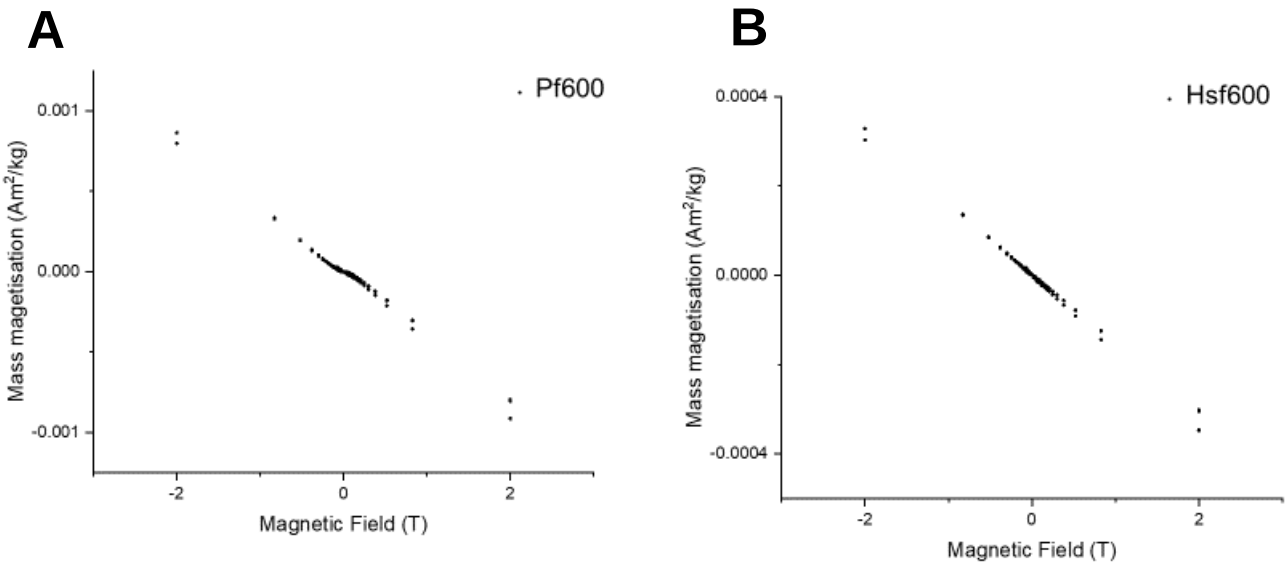

Figure 4.6 Further magnetic susceptibility testing of anaerobically loaded ferritin

Field sweep of ±0.5 Tesla using the MPMS3 magnetometer (A) magnetic susceptibility of anaerobically loaded Pf600 (B) anaerobically loaded Hsf600

4.7 Cationisation analysis

One-pot chemical cationisation of the *Pf* ferritin was employed to give the nanoparticles an overall positive charge, preparing them for downstream bacterial concentration experiments. Initially, apoPf was subject to cationisation and sample polydispersity tested using DLS. Furthermore, zeta potential analysis was used to elicit the change in particle surface change. Mineralised *Pyrococcus* ferritin and commercially available horse spleen ferritin samples were subject to cationisation to understand particle stability and cationisation efficiency across the ferritin species. The same nomenclature used throughout the thesis is used here. The apo- prefix describes ferritin as pre-mineralisation and Pf120 used to describe ferritin mineralised with 120 iron atoms per particle. The Cat- prefix refers to the ferritin samples that had been subjected to the cationisation reaction.

4.7.1 Cationisation of apo-ferritin

Initial DLS analysis of apoPf, Figure 4.7, demonstrates the polydispersity of the sample post cationisation reaction. Considering the three hydrodynamic diameter measurements for apoPf there is an even distribution for particle number, particle volume and particle intensity. Furthermore these peaks are reflected in the size parameters, with an overall mean hydrodynamic diameter of 11.66 nm, Table 4-1.

Considering the Cat-apoPf ferritin, there was an even hydrodynamic diameter distribution seen for particle number and volume. However, there was a wider size distribution for the hydrodynamic intensity, this was reflected by an increased mean hydrodynamic diameter and Z-average for the particle, 14.12 nm and 25.76 nm respectively. Polydispersity indices for the samples, Table 4-1, were below 0.34 for all samples providing confidence in sample polydispersity and homogeneity.

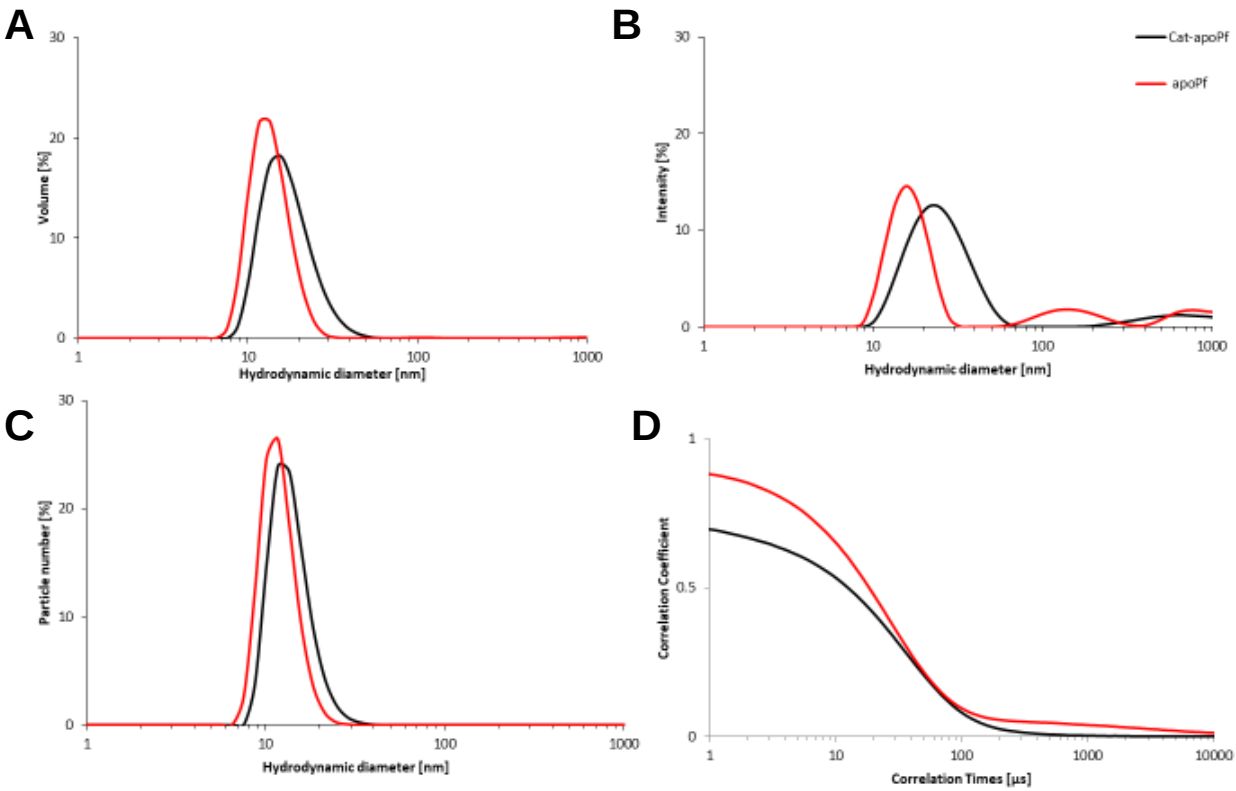

Figure 4.7 Dynamic light scattering size analysis for cationised apoPf ferritin

Hydrodynamic diameter as volume of sample (A), intensity of signal (B), and mean particle number(C) and correlation coefficient (D)

Table 4-1 Dynamic light scattering parameters

Size comparison between apo-Pf ferritin and cationised apo-Pf ferritin

				Volume Distribution			
	Number Mean d (nm)	Z-average d (nm)	PDI	Peak 1 Mean d (nm)	Peak 1 Area Percent	Peak 2 Mean d (nm)	Peak 2 Area Percent
apoPf	11.66	18.17	0.30	16.50	84.10	2697	15.90
Cat-apoPf	14.12	25.76	0.33	24.87	82.70	538.3	17.30

The zeta potential of the samples was measured to understand the particles surface charge and to compare the difference between pre- and post-cationisation reaction. In Figure 4.8 it is evident that the Cat-apoPf has an overall positive charge with a zeta potential of 25.1 mV (measurement taken at pH 7.6). The surface charge of apoPf is much less distinct, but the peak indicates an overall negative zeta potential of -21.0 mV at pH 6.5.

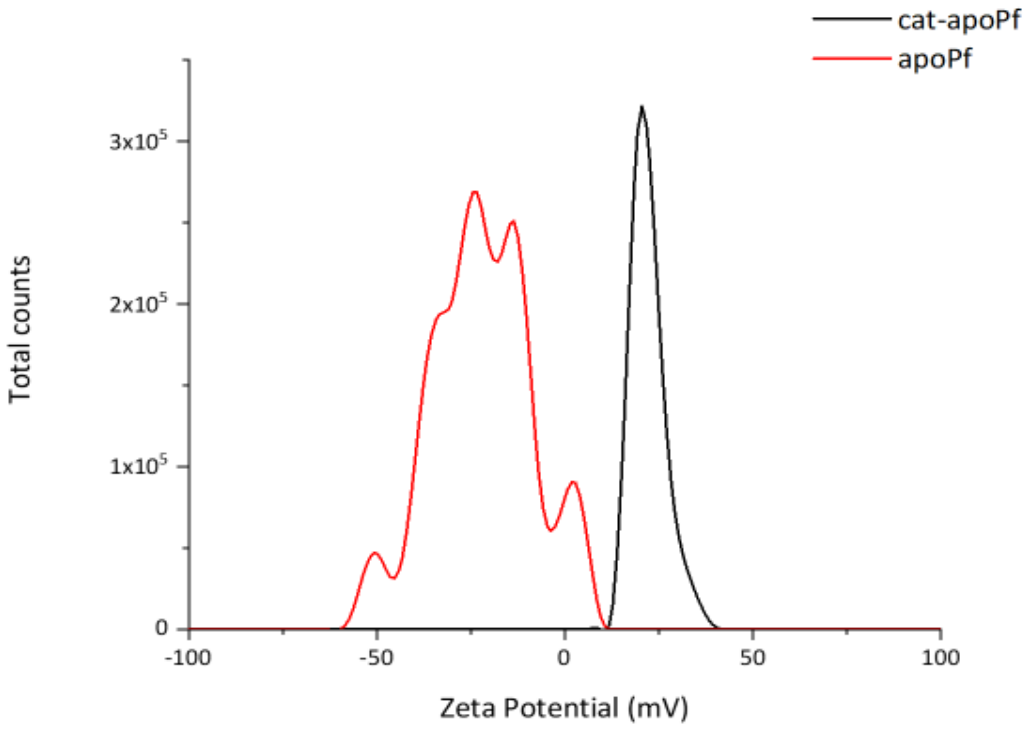

Figure 4.8 Zeta potential of cationised apoPf

Comparison between Cat-apoPf (black) with average zeta potential of 25.1 mV, and apoPf (red) with an average zeta potential of -21.00 mV.

4.7.2 Cationisation of mineralised ferritin

In this section the cationisation of apo-ferritin was compared with that of mineralised ferritin, with both *Pyrococcus* and commercially available horse spleen ferritin under scrutiny. The same cationisation protocol was used as previously described (Section 4.7.1) and the particle dispersity was measured using DLS. Considering the DLS analysis of *Pf* ferritin, Figure 4.9, there is an even distribution for the hydrodynamic volume and hydrodynamic number of both samples. However, there is a slightly increased diameter for the hydrodynamic intensity, this is accounted for with an increased Z-average and higher intensity size distribution peaks, reflected in the size parameters in Table 4-2. Considering the correlograms, the sigmoidal decay is less defined than in previous measurements, with the curves undulating on their decline.

Considering the horse spleen ferritin, Figure 4.10, there was even distribution seen for hydrodynamic volume and hydrodynamic number, as seen with the apoPf. However, the intensity was more uneven with a multimodal distribution seen for the Cat-apoHsf and a bimodal distribution seen for Cat-Hsf120. The correlograms do not take the distinct sigmoidal decay as seen with previous ferritin size measurements. The size parameters reported in Table 4-2 show an elevated Z-average and inconsistent intensity size distribution peaks despite a relatively low PDI. Due to a lack of uniformity with the increased Z-average and particle mean diameter, these samples were characterised as too polydisperse for downstream zeta potential measurements.

Table 4-2 Dynamic light scattering size parameters

Comparison of cationised ferritins before and after mineralisation with 120 iron atoms.

				Volume Distribution			
	Number Mean d (nm)	Z-average d (nm)	PDI	Peak 1 Mean d (nm)	Peak 1 Area Percent	Peak 2 Mean d (nm)	Peak 2 Area Percent
Cat-apoPf	23.38	52.15	0.23	33.78	100.00	0.00	0.00
Cat-Pf120	17.63	46.10	0.34	26.01	99.40	3068	0.60
Cat-apoHsf	13.54	139.10	0.19	15.18	97.00	159.8	3.00
Cat-Hsf120	12.30	46.95	0.54	16.12	99.40	392.40	0.60

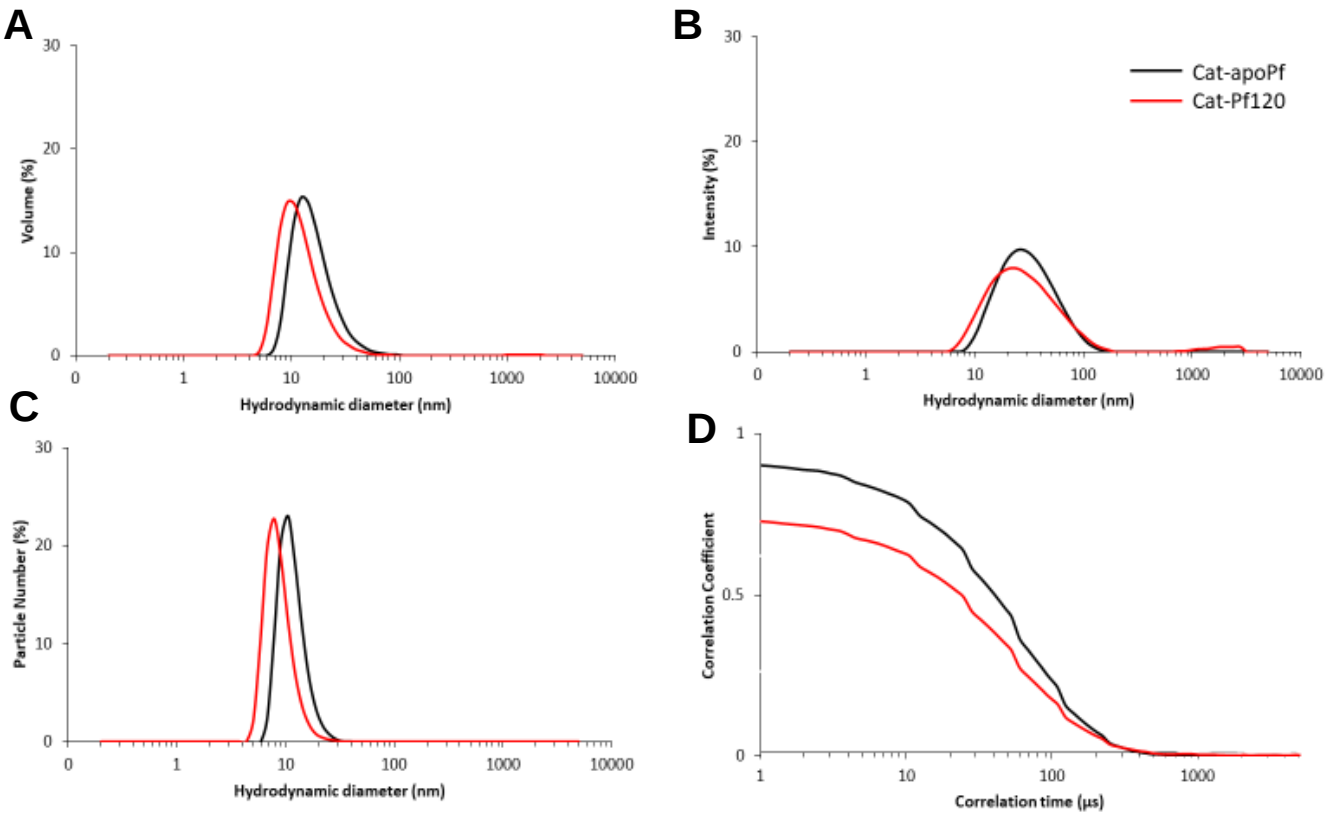

Figure 4.9 Dynamic light scattering size analysis for cationised *Pf* ferritin

Hydrodynamic diameter as volume of sample (A), intensity of signal (B), and mean particle number(C) and correlation coefficient (D)

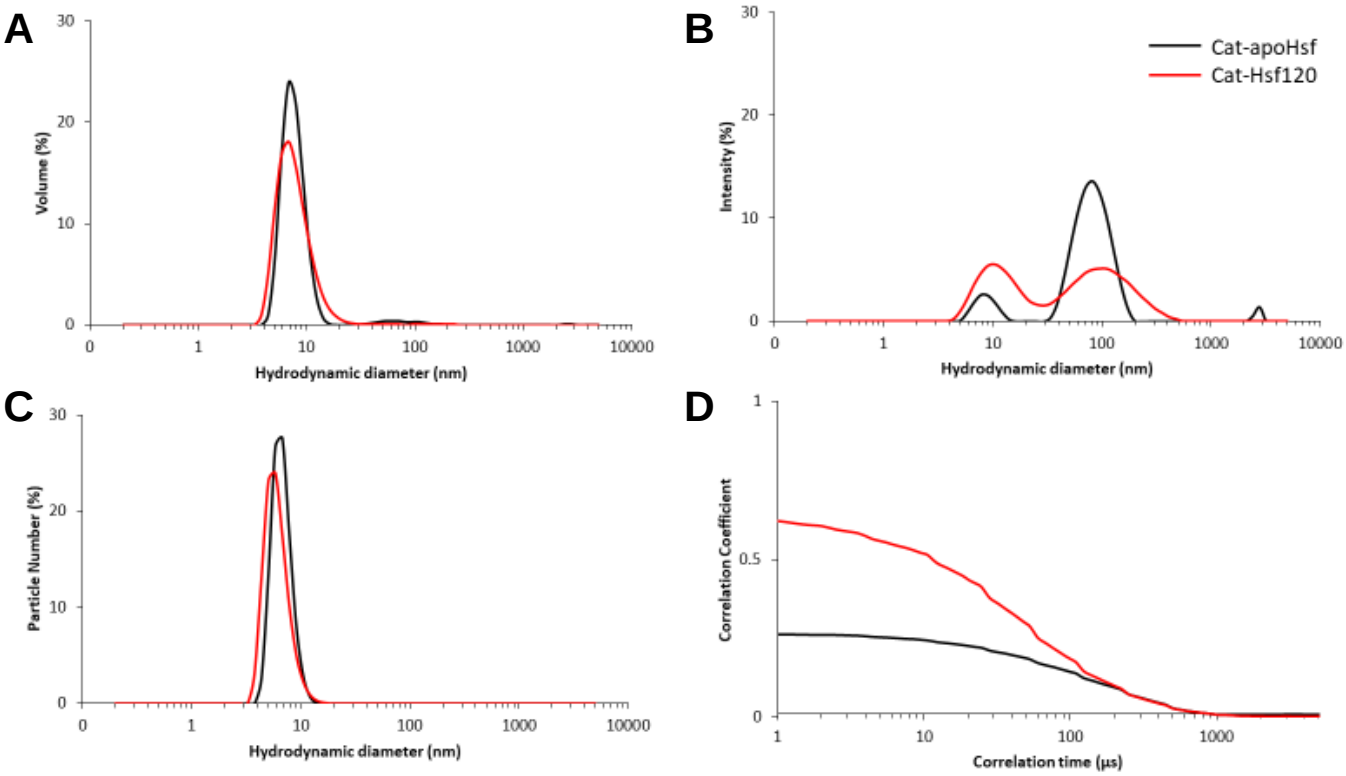

Figure 4.10 Dynamic light scattering size analysis for cationised Hsf ferritin

Hydrodynamic diameter as volume of sample (A), intensity of signal (B), and mean particle number (C) and correlation coefficient (D)

4.8 Discussion

The magnetometry experiments in this chapter failed to determine the magnetic susceptibility of the mineralised recombinant and commercially available ferritin samples. Supplementary investigation is required to elucidate the shortcomings of the protocol used. The cationisation investigation highlights a change in particle charge seen in the zeta potentiometry measurements for Cat-apoPf. Further characterisation is required to investigate the cationisation of mineralised samples, which were determined as inappropriate for downstream application in this investigation.

Although efforts were made during the revised anaerobic mineralisation to limit the amount of oxygen from entering the reaction, samples prepared using this revised protocol did not provide enough evidence for the characterisation of a super-paramagnetic nanoparticle. The magnetometry data suggest the particles convey some paramagnetism initially, which is subsequently lost as the iron oxide inside the ferritin changes oxidation states from Fe_3O_4 to $Fe_2O_3{}_nH_20$. This contrasted with the magnetic susceptibility testing of cobalt-doped Fe_3O_4 core reconstitution inside commercially available horse spleen ferritin shown by Carreira et al. [23] and further shown in the iron-oxide core reconstitution of recombinant *Pyrococcus* ferritin by Parker et al.[42]. with both these examples providing strong evidence of superparamagnetism through magnetometry field sweeps. There is also scope for further investigation into cobalt doping of the recombinant ferritin core in order to influence the magnetic susceptibility of the particles.

Further development of the protocol is required to reproduce these previous findings, with increased attention on limiting the oxygen atmosphere of the reaction. This could include the purging of all buffers and samples with nitrogen gas before introduction to the anaerobic chamber. In addition, a more appropriate SQUID field sweep would improve future analysis, with sweeps of ±2 Tesla a minimum in order to determine the paramagnetic qualities of the samples. Alternatively, investigation into the particle core using Raman spectroscopy and electron diffraction could better characterise the iron oxide constituents, specifying the iron oxidation state and therefore providing an indication of magnetic susceptibility without the need for SQUID magnetometry.

There was success with the cationisation experiments, with initial tests of Cat-apoPf ferritin demonstrating a change in particle surface charge from negative to positive zeta potential, this reflects similar findings in the cationisation of horse spleen ferritin by Carreira et al. [66]. There is no evidence in the literature of such investigation into recombinant *Pyrococcus* ferritin. Despite this, the increased particle polydispersity was of concern, and inconsistent DLS size measurements of mineralised cationised ferritins provided evidence of aggregation and sample heterogeneity which was deemed unacceptable for downstream application.

A greater extent of characterisation by TEM could be used to better visualise particle stability. Equally, further protocol development is necessary to better understand particle stability after the cationisation reaction and to optimise the particle homogeneity and monodisperse particle yield. Aggregation could be attenuated by adjusting the pH of the reaction, moving the reaction away from the isoelectric point of the *Pf* ferritin. Alternatively, increased attention to the particle purification step could increase functionalised particle stability and yield, moving away from SEC towards analytical ultra centrifugation and asymmetric flow field flow fractionation, techniques used by Le Vay [51] when separating aggregated recombinant bacterioferritin.

Chapter 5 Conclusions

This project has identified a viable thermostable recombinant protein, namely *Pyrococcus furiosus* ferritin, which could facilitate bacterial labelling and optimise bacterial concentration from water samples. By refining and combining TEM and SAXS analysis the investigation has demonstrated how iron oxide may reconstitute within the nanoparticle core and has shown the controllable loading of iron oxide core in its cavity

This work provides evidence to suggest that the experimental conditions promoted the formation of a hydrated iron (III) oxide ($Fe_2O_3 \cdot nH_2O$) rather than the desired magnetite (Fe_3O_4). Extensive particle characterisation has provided evidence to support a conclusion that there is little structural difference between mineralised Hsf and *Pf* ferritin. This is important as there are benefits from using the recombinant *Pf* ferritin over commercially available horse spleen ferritin, these include, increased magnetic susceptibility, quality control, thermostability and cost effectiveness.

TEM and DLS size analysis has identified two mineralisation techniques which have little impact upon particle polydispersity. This analysis, supported by dummy atom modelling and form factor fitting of the SAXS data, provides evidence to propose that these could form the basis of tuneable mineralisation protocols that would enable magnetic distinction between different particles. Such controllable mineralisation highlights an opportunity to use *Pf* ferritin nanoparticles mineralised with varying concentrations of magnetic iron oxide, potentially concentrating bacteria by differences in magnetic susceptibility, however this is something yet to be explored.

The cationisation of a recombinant *Pf* ferritin has provided evidence that these recombinant particles can be chemically adjusted to exhibit a positive surface charge. However, more work is needed to demonstrate the cationisation of the mineralised particles, as seen in the cationisation of mineralised Hsf [66]. Such technologies could be employed with inexpensive lab-on-a-chip microfluidic devices to provide point of care bacterial labelling diagnostics for those in resource-poor settings.

Chapter 6 References

[1] Kanitthamniyom, P. Zhang, Y., 2019. 'Magnetic digital microfluidics on a bioinspired surface for point-of-care diagnostics of infectious disease', *Electrophoresis*, vol. 40, no. 8, pp. 1178–1185.

[2] Davies, S., 2011. 'Annual Report of the Chief Medical Officer, Volume Two, Infections the rise of antimicrobial resistance', Department of Health, London, 2013.

[3] Amin, M. T., Alazba A. A., Manzoor, U., 2014. 'A Review of Removal of Pollutants from Water/Wastewater Using Different Types of Nanomaterials', *Advances in Materials Science and Engineering*, vol. 2014, pp. 1–24,

[4] Cortie, M. B., 2004. 'The weird world of nanoscale gold', *Gold Bulletin*, vol. 37, no. 1–2, pp. 12–19, doi: 10.1007/BF03215512.

[5] Mohammed, L., Gomaa, H. G., Ragab, D., Zhu, J., 2017. 'Magnetic nanoparticles for environmental and biomedical applications: A review', *Particuology*, vol. 30, pp. 1–14,

[6] Nath, D. Banerjee, P., 2013. 'Green nanotechnology – A new hope for medical biology', *Environmental Toxicology and Pharmacology*, vol. 36, no. 3, pp. 997–1014.

[7] Bobo D., Robinson, K. J., Islam, J., Thurecht, K. J., Corrie, S. R.,2016 'Nanoparticle-Based Medicines: A Review of FDA-Approved Materials and Clinical Trials to Date', *Pharm. Res.*, vol. 33, no. 10, pp. 2373–2387,

[8] Benbrook, D. M., 2015 'Biotechnology and Biopharmaceuticals: Transforming Proteins and Genes Into Drugs, 2nd Edition', *Clin Infect Dis*, vol. 60, no. 2, pp. 331–332,

[9] Pawar, H. R., Bhosale, S. S., Derle, N. D., 2012. 'Use of liposomes in cancer therapy: a review', *Int J Pharm Sci Res.*, vol. 3(10); 3585-3590.

[10] Zhang, J. Yu, S.-H., 2016. 'Carbon dots: large-scale synthesis, sensing and bioimaging', *Materials Today*, vol. 19, no. 7, pp. 382–393

[11] Hill, S. A., Benito-Alifonso, D., Morgan, D. J., Davis, S. A., Berry, M., Galan M. C., 2016. 'Three-minute synthesis of sp3 nanocrystalline carbon dots as non-toxic fluorescent platforms for intracellular delivery', *Nanoscale*, vol. 8, no. 44, pp. 18630–18634.

[12] Feridex. *Questions and Answers in MRI*. [online] Available at: http://mriquestions.com/feridex-and-iron-oxides.html (accessed Mar. 01, 2019)

[13] Singh, N., Jenkins, G. J. S., Asadi, R., Doak S. H., 2010. 'Potential toxicity of superparamagnetic iron oxide nanoparticles (SPION)', *Nano Rev*, vol. 1. doi: 10.3402/nano.v1i0.5358.

[14] Kumar, A., 2017. 'Nanotechnology for Neuroscience: Promising Approaches for Diagnostics, Therapeutics and Brain Activity Mapping', *Advanced Functional Materials*, vol. 27, no. 39, p. 1700489. doi: 10.1002/adfm.201700489.

[15] Rodzinski, A., 2016. 'Targeted and controlled anticancer drug delivery and release with magnetoelectric nanoparticles', *Scientific Reports*, vol. 6, p. 20867, doi: 10.1038/srep20867.

[16] Wanna, Y., 2016. 'Efficiency of SPIONs functionalized with polyethylene glycol bis(amine) for heavy metal removal', *Journal of Magnetism and Magnetic Materials*, vol. 414, pp. 32–37. doi: 10.1016/j.jmmm.2016.04.064.

[17] Jiles D., 1991. *Introduction to magnetism and magnetic materials*. London ; Chapman and Hall.

[18] E. D. T. de Lacheisserie, U. J. Fourier, D. Gignoux, M. Schlenker, 2005. *Magnetism*. Springer Science & Business Media.
[19] Mody, V. V., Cox, A., Shah, S., Singh A., Bevins W., Parihar H., 2014. 'Magnetic nanoparticle drug delivery systems for targeting tumor', *Applied Nanoscience*, vol. 4, no. 4, pp. 385–392. doi: 10.1007/s13204-013-0216-y.
[20] Schmool D. S. Kachkachi H., 2016. 'Chapter One - Collective Effects in Assemblies of Magnetic Nanaparticles', *Solid State Physics*, vol. 67, pp. 1–101.
[21] Beveridge T. J.. Davies J. A., 1983 'Cellular responses of Bacillus subtilis and Escherichia coli. to the Gram stain.', *J Bacteriol*, vol. 156, no. 2, pp. 846–858.
[22] Murphy K. Weaver C., 2017. *Janeway's immunobiology*, Ninth edition. New York, NY, USA: Garland Science, Taylor & Francis Group.
[23] Carreira, S. C., Spencer, J., Schwarzacher, W., Seddon, A. M., 2016 'Cationized Magnetoferritin Enables Rapid Labeling and Concentration of Gram-Positive and Gram-Negative Bacteria in Magnetic Cell Separation Columns', *Appl. Environ. Microbiol.*, vol. 82, no. 12, pp. 3599–3604. doi: 10.1128/AEM.00720-16.
[24] Gu, H., Ho, P.-L., Tsang, K. W. T., Wang, L., Xu B., 2003. 'Using Biofunctional Magnetic Nanoparticles to Capture Vancomycin-Resistant Enterococci and Other Gram-Positive Bacteria at Ultralow Concentration', *J. Am. Chem. Soc.*, vol. 125, no. 51, pp. 15702–15703. doi: 10.1021/ja0359310.
[25] Libretexts. 2018. '*Types of Intermolecular Forces: Dispersion, Dipole–Dipole, Hydrogen Bonding, and Ion-Dipole*' [online] Available at: https://chem.libretexts.org/Courses/College_of_Marin/Marin%3A_CHEM_114_-_Introductory_Chemistry_(Daubenmire)/12%3A_Liquids%2C_Solids%2C_and_Intermolecular_Forces/12.6%3A_Types_of_Intermolecular_Forces%3A_Dispersion%2C_Dipole%E2%80%93Dipole%2C_Hydrogen_Bonding%2C_and_Ion-Dipole. (accessed Jan. 21, 2019)
[26] Miltenyi, S., Müller, W., Weichel, W., Radbruch, A., 1990. 'High gradient magnetic cell separation with MACS', *Cytometry*, vol. 11, no. 2, pp. 231–238. doi: 10.1002/cyto.990110203.
[27] Mu, K. 2015. 'Monoclonal Antibody–Conjugated Superparamagnetic Iron Oxide Nanoparticles for Imaging of Epidermal Growth Factor Receptor–Targeted Cells and Gliomas', *Mol Imaging*, vol. 14, no. 5, pp. 72-90. doi: 10.2310/7290.2015.00002.
[28] Liu, J. K. H., 2014. 'The history of monoclonal antibody development – Progress, remaining challenges and future innovations', *Ann Med Surg (Lond)*, vol. 3, no. 4, pp. 113–116. doi: 10.1016/j.amsu.2014.09.001.
[29] Shaughnessy A. F., 2012. 'Monoclonal antibodies: magic bullets with a hefty price tag', *BMJ*, vol. 345. doi: 10.1136/bmj.e8346.
[30] Greenwood, N. N. Earnshaw A., 1997. *Chemistry of the elements*, 2nd ed., 1. Boston, Mass. Butterworth-Heinemann.
[31] Sánchez, M., Sabio, L., Gálvez, N., Capdevila, M., Dominguez‐Vera, J. M., 2017 'Iron chemistry at the service of life', *IUBMB Life*, vol. 69, no. 6, pp. 382–388. doi: 10.1002/iub.1602.
[32] Zhang, C., 2014. 'Essential functions of iron-requiring proteins in DNA replication, repair and cell cycle control', *Protein Cell*, vol. 5, no. 10, pp. 750–760, doi: 10.1007/s13238-014-0083-7.
[33] Theil, E. C., 2003. 'Ferritin: At the Crossroads of Iron and Oxygen Metabolism', *J Nutr*, vol. 133, no. 5, pp. 1549-1553. doi: 10.1093/jn/133.5.1549S.

[34] He, D. Marles-Wright, J., 2015. ‘Ferritin family proteins and their use in bionanotechnology’, *N Biotechnol*, vol. 32, no. 6, pp. 651–657. doi: 10.1016/j.nbt.2014.12.006.
[35] Theil, E. C.,1987. ‘Ferritin: structure, gene regulation, and cellular function in animals, plants, and microorganisms’, *Annu. Rev. Biochem.*, vol. 56, pp. 289–315. doi: 10.1146/annurev.bi.56.070187.001445.
[36] Juan, S.-H. Aust, S. D., 1998. ‘The Effect of Putative Nucleation Sites on the Loading and Stability of Iron in Ferritin’, *Archives of Biochemistry and Biophysics*, vol. 350, no. 2, pp. 259–265. doi: 10.1006/abbi.1997.0523.
[37] Kasyutich, O., Ilari, A., Fiorillo, A., Tatchev, D., Hoell, A., Ceci, P., 2010. ‘Silver Ion Incorporation and Nanoparticle Formation inside the Cavity of Pyrococcus furiosus Ferritin: Structural and Size-Distribution Analyses’, *J. Am. Chem. Soc.*, vol. 132, no. 10, pp. 3621–3627, doi: 10.1021/ja910918b.
[38] Mackle, P., Charnock, J. M., Garner, C. D., Meldrum, F. C., and Mann, S.,1993. ‘Characterization of the manganese core of reconstituted ferritin by x-ray absorption spectroscopy’, *Journal of the American Chemical Society*, vol. 115, no. 18, pp. 8471–8472. doi: 10.1021/ja00071a076.
[39] Kim, M. 2011. ‘pH-Dependent Structures of Ferritin and Apoferritin in Solution: Disassembly and Reassembly’, *Biomacromolecules*, vol. 12, no. 5, pp. 1629–1640. doi: 10.1021/bm200026v.
[40] Fiala, G. Stetter, K. O., 1986. ‘Pyrococcus furiosus sp. nov. represents a novel genus of marine heterotrophic archaebacteria growing optimally at 100°C’, *Arch. Microbiol.*, vol. 145, no. 1, pp. 56–61. doi: 10.1007/BF00413027.
[41] Tatur, J., Hagen, W. R., Matias P. M., 2007. ‘Crystal structure of the ferritin from the hyperthermophilic archaeal anaerobe Pyrococcus furiosus’, *J Biol Inorg Chem*, vol. 12, no. 5, pp. 615–630. doi: 10.1007/s00775-007-0212-3.
[42] Parker, M. J., Allen, M. A., Ramsay, B., Klem, M. T., Young, M., Douglas, T., 2008. ‘Expanding the Temperature Range of Biomimetic Synthesis Using a Ferritin from the Hyperthermophile *Pyrococcus furiosus*’, *Chemistry of Materials*, vol. 20, no. 4, pp. 1541–1547. doi: 10.1021/cm702732x.
[43] O’Neil, J., 2015 ‘Rapid diagnostics: stopping unnecessary use of antibiotics’. [Online]. Available: https://amr-review.org/.
[44] Ray, M. J., Tallman, G. B., Bearden, D. T., Elman, M. R., McGregor, J. C., 2019. ‘Antibiotic prescribing without documented indication in ambulatory care clinics: national cross sectional study’, *BMJ*, vol. 367. doi: 10.1136/bmj.l6461.
[45] Rahi, P., Prakash, O.,. Shouche, Y. S., 2016. ‘Matrix-Assisted Laser Desorption/Ionization Time-of-Flight Mass-Spectrometry (MALDI-TOF MS) Based Microbial Identifications: Challenges and Scopes for Microbial Ecologists’, *Front. Microbiol.*, vol. 7. doi: 10.3389/fmicb.2016.01359.
[46] Chang, S.-S. 2013 ‘Multiplex PCR System for Rapid Detection of Pathogens in Patients with Presumed Sepsis – A Systemic Review and Meta-Analysis’, *PLoS ONE*, vol. 8, no. 5. doi: 10.1371/journal.pone.0062323.
[47] Votintseva, A. A., 2017 ‘Same-Day Diagnostic and Surveillance Data for Tuberculosis via Whole-Genome Sequencing of Direct Respiratory Samples’, *J Clin Microbiol*, vol. 55, no. 5, pp. 1285–1298. doi: 10.1128/JCM.02483-16.
[48] Cohen, J. 2015. ‘Sepsis: a roadmap for future research’, *The Lancet Infectious Diseases*, vol. 15, no. 5, pp. 581–614. doi: 10.1016/S1473-3099(15)70112-X.
[49] Okuda, M., Eloi, J.-C., Jones, S. E. W., Sarua, A., Richardson, R. M., Schwarzacher, W., 2012 ‘Fe 3 O 4 nanoparticles: protein-mediated crystalline

magnetic superstructures', *Nanotechnology*, vol. 23, no. 41, doi: 10.1088/0957-4484/23/41/415601.
[50] Weeratunga, S. K., Gee, C. E., Lovell, S., Zeng, Y., Woodin, C. L., Rivera, M., 2009. 'Binding of Pseudomonas aeruginosa Apo-Bacterioferritin Associated Ferredoxin to Bacterioferritin B Promotes Heme Mediation of Electron Delivery and Mobilization of Core Mineral Iron', *Biochemistry*, vol. 48, no. 31, pp. 7420–7431. doi: 10.1021/bi900561a.
[51] Le Vay, K. K., 2017. 'The construction of functional bacterioferritin-nanoparticle complexes using hydrostatic pressure', University of Bristol.
[52] Pray, L., 2008. Recombinant DNA technology and transgenic animals. *Nature Education* 1(1):51
[53] Berg, J. M., Tymoczko, J. L., Gatto, G. J. Jr., Stryer, L., 2015.*Biochemistry*, Eighth edition. New York: W.H. Freeman.
[54] Simons, R. W., Houman, F., Kleckner, N.,1987 'Improved single and multicopy lac-based cloning vectors for protein and operon fusions', *Gene*, vol. 53, no. 1, pp. 85–96. doi: 10.1016/0378-1119(87)90095-3.
[55] He, F., 2011. 'Bradford Protein Assay', *BIO-PROTOCOL*, vol. 1, no. 6, doi: 10.21769/BioProtoc.45.
[56] MBL Life Sience 'The principle and method of polyacrylamide gel electrophoresis (SDS-PAGE)' [online] Available at: https://www.mblbio.com/bio/g/support/method/sds-page.html (accessed Jun. 02, 2019).
[57] Nowakowski, A. B., Wobig, W. J., Petering, D. H., 2014. 'Native SDS-PAGE: High Resolution Electrophoretic Separation of Proteins With Retention of Native Properties Including Bound Metal Ions', *Metallomics*, vol. 6, no. 5, pp. 1068–1078. doi: 10.1039/c4mt00033a.
[58] Mori, S. Barth H. G., 2013. *Size Exclusion Chromatography*. Springer Science & Business Media.
[59] Einstein, A., 'Investigations on the theory of the Brownian movement', *Ann. Phys*, p. 11, 1906.
[60] Winey, M., Meehl, J. B., O'Toole, E. T., Giddings T. H., 2014. 'Conventional transmission electron microscopy', *MBoC*, vol. 25, no. 3, pp. 319–323. doi: 10.1091/mbc.e12-12-0863.
[61] Schneider, C. A., Rasband, W. S., Eliceiri, K. W., 2012. 'NIH Image to ImageJ: 25 years of image analysis', *Nat Methods*, vol. 9, no. 7, pp. 671–675. doi: 10.1038/nmeth.2089.
[62] Sneddon, J., Vincent, M., 2008. 'ICP-OES and ICP-MS for the Determination of Metals: Application to Oysters':, *Analytical Letters*, vol. 41, pp. 1291–1393. doi: 10.1080/00032710802013991.
[63] Meldrum F., Heywood B., Mann S., 1992. 'Magnetoferritin: in vitro synthesis of a novel magnetic protein', *Science*, vol. 257, no. 5069, pp. 522–523. doi: 10.1126/science.1636086.
[64] Koppel, D. E., 1972. 'Analysis of Macromolecular Polydispersity in Intensity Correlation Spectroscopy: The Method of Cumulants', *The Journal of Chemical Physics*, vol. 57, no. 11, pp. 4814–4820. doi: 10.1063/1.1678153.
[65] Malvern Panalytical. 'Dynamic light scattering common terms defined', *Inform White Paper*. [online] available at: https://www.malvernpanalytical.com/en/learn/knowledge-center/whitepapers/WP111214DLSTermsDefined (accessed Aug. 04, 2019).

[66] Carreira, S. C., Armstrong, J. P. K., Okuda, M., Seddon, A. M., Perriman, A. W., Schwarzacher, W.,2016. 'Synthesis of Cationized Magnetoferritin for Ultra-fast Magnetization of Cells', *JoVE (Journal of Visualized Experiments)*, no. 118, p. e54785. doi: 10.3791/54785.
[67] Pauw, B., 2011. 'About SA(X)S', *Looking At Nothing*,' [online] Available at: https://lookingatnothing.com/index.php/about-saxs (accessed Apr. 16, 2020).
[68] Putnam, C. D., Hammel, M., Hura, G. L., Tainer, J. A., 2007. 'X-ray solution scattering (SAXS) combined with crystallography and computation: defining accurate macromolecular structures, conformations and assemblies in solution', *Q. Rev. Biophys.*, vol. 40, no. 3, pp. 191–285. doi: 10.1017/S0033583507004635.
[69] Stribeck, N., 2007. *X-Ray Scattering of Soft Matter*. Springer.
[70] Glatter, O., Kratky, O., 1982. *Small angle x-ray scattering*. London ; Academic Press.
[71] Kikhney, A. G., Svergun, D. I., 2015. 'A practical guide to small angle X-ray scattering (SAXS) of flexible and intrinsically disordered proteins', *FEBS Letters*, vol. 589, no. 19, pp. 2570–2577. doi: 10.1016/j.febslet.2015.08.027.
[72] Diamond Light Source 'Welcome to B21 - Small Angle Scattering -'.[online] Available at: https://www.diamond.ac.uk/Instruments/Soft-Condensed-Matter/small-angle/B21.html (accessed Feb. 03, 2020).
[73] Jacques, D. A. Trewhella, J.,2010. 'Small-angle scattering for structural biology—Expanding the frontier while avoiding the pitfalls', *Protein Sci*, vol. 19, no. 4, pp. 642–657. doi: 10.1002/pro.351.
[74] Rambo, R. P., Tainer, J. A., 2011. 'Characterizing flexible and intrinsically unstructured biological macromolecules by SAS using the Porod-Debye law', *Biopolymers*, vol. 95, no. 8, pp. 559–571. doi: 10.1002/bip.21638.
[75] Franke, D. Svergun, D. I., 2009. 'DAMMIF, a program for rapid ab-initio shape determination in small-angle scattering', *J Appl Cryst*, vol. 42, no. 2, pp. 342–346. doi: 10.1107/S0021889809000338.
[76] Sasview. 'Fitting Models with Structure Factors — SasView 5.0.1 documentation'. [online] Available at: http://www.sasview.org/docs/user/qtgui/Perspectives/Fitting/fitting_sq.html (accessed Apr. 16, 2020).
[77] Franke, D., 2017. 'ATSAS 2.8: a comprehensive data analysis suite for small-angle scattering from macromolecular solutions', *J Appl Crystallogr*, vol. 50, no. 4, pp. 1212–1225. doi: 10.1107/S1600576717007786.
[78] SasView, 'SasView'. [online] Available at: https://sasview.github.io/ (accessed Feb. 03, 2020).
[79] Kotlarchyk, M., Stephens, R. B., Huang, J. S., 1988. 'Study of Schultz distribution to model polydispersity of microemulsion droplets', *J. Phys. Chem.*, vol. 92, no. 6, pp. 1533–1538. doi: 10.1021/j100317a032.
[80] Sasview 'Polydispersity & Orientational Distributions — SasView 5.0.1 documentation'. [online] Available at: http://www.sasview.org/docs/user/qtgui/Perspectives/Fitting/pd/polydispersity.html#gaussian-distribution (accessed Apr. 16, 2020).
[81] Fischbach, F. A., Anderegg, J. W., 1965. 'An X-ray scattering study of ferritin and apoferritin', *Journal of Molecular Biology*, vol. 14, no. 2, pp. 458. doi: 10.1016/S0022-2836(65)80196-6.

[82] Kuklin, A. I., 2012. ‘Comparative study on low resolution structures of apoferritin via SANS and SAXS’, *J. Phys.: Conf. Ser.*, vol. 351. doi: 10.1088/1742-6596/351/1/012009.
[83] Melníková, L., 2014 ‘Effect of iron oxide loading on magnetoferritin structure in solution as revealed by SAXS and SANS’, *Colloids and Surfaces B: Biointerfaces*, vol. 123, pp. 82–88, doi: 10.1016/j.colsurfb.2014.08.032.
[84] McMaster, W. H., Del Grande, N. K., Mallett, J. H., Hubbell J. H., ‘Compilation of x-ray cross sections.’, California Univ., Livermore. Accessed: Apr. 20, 2020. [Online]. Available at: https://www.osti.gov/biblio/4191734-compilation-ray-cross-sections-section-iii.
[85] Adolphi, N. L., 2009. ‘Characterization of magnetite nanoparticles for SQUID-relaxometry and magnetic needle biopsy’, *J Magn Magn Mater*, vol. 321, no. 10, pp. 1459–1464. doi: 10.1016/j.jmmm.2009.02.067.
[86] Danon, D., Goldstein, L., Marikovsky, Y., Skutelsky, E., 1972 ‘Use of cationized ferritin as a label of negative charges on cell surfaces - ScienceDirect’, *Journal of Ultrastructure Research*, vol. 38, no. 5–6, pp. 500–510. doi: https://doi.org/10.1016/0022-5320(72)90087-1.
[87] Grabarek, Z. Gergely, J., 1990. ‘Zero-length crosslinking procedure with the use of active esters’, *Analytical Biochemistry*, vol. 185, no. 1, pp. 131–135. doi: 10.1016/0003-2697(90)90267-D.
[88] Jacobasch, H.-J., Bauback, G., Schurz, J., 1985. ‘Problems and results of zeta-potential measurements on fibers’, *Colloid & Polymer Sci*, vol. 263, no. 1, pp. 3–24. doi: 10.1007/BF01411243.
[89] Selvamani, V., 2019. ‘Chapter 15 - Stability Studies on Nanomaterials Used in Drugs’, in *Characterization and Biology of Nanomaterials for Drug Delivery*, Eds. Elsevier, pp. 425–444.
[90] Kaszuba, M., Corbett, J., Watson, F. M., Jones, A., 2010. ‘High-concentration zeta potential measurements using light-scattering techniques’, *Philos Trans A Math Phys Eng Sci*, vol. 368, no. 1927, pp. 4439–4451. doi: 10.1098/rsta.2010.0175.